PONTIFICIA UNIVERSIDAD CATÓLICA DEL PERÚ

FACULTAD DE CIENCIAS E INGENIERÍA

Sistemas electro-ópticos para aplicaciones clásicas y cuánticas.

Trabajo de suficiencia profesional - Informe - para obtener el título profesional de Licenciado en Física

AUTOR

Alfredo Rolando Rueda Sánchez

ASESOR

Eduardo Ruben Massoni Kamimoto

Lima, Noviembre, 2021

Resumen

Este informe recopila mi experiencia de trabajo de los últimos tres años. Mi carrera como físico experimental y teórico me llevo a trabajar como investigador en distintos lugares. Específicamente, en el tiempo que respecta a este informe, tuve la posibilidad de trabajar en University of Otago con sede en Dunedin-Nueva Zelanda y en el Institute of Science and Technology Austria con sede en Klosterneuburg-Austria. Además, de mi trabajo actual como *Senior lab Scientist* en la empresa Scantinel photonics GmbH. con sede en Ulm-Alemania, donde actualmente desarrollo sensores de LiDAR para carros autónomos.

El núcleo de mi especialización en física se cataloga como electro-óptica cuántica que investiga la interacción entre campos electromagnéticos ópticos y de radio-frecuencia al nivel fotónico. Este tipo de interacción, debido a la naturaleza de la radiación electromagnética solo se puede lograr en sistemas no lineales como cristales o en sistemas más modernos como nanoestructuras. En mi caso, he trabajado con cristales no lineales, cuya polarización dependen cuadraticamente del campo eléctrico aplicado $\tilde{\mathbf{P}} = \chi^{(\mathbf{2})}\tilde{\mathbf{E}}\tilde{\mathbf{E}}$, en el rango de microondas y óptico. El efecto Pockels, que es como se le denomina a la interacción de estos dos rangos de frecuencia, sirve como base para estudiar distintos sistemas físicos con usos muy interesantes no solo para la física cuántica, sino también para sistemas clásicos. Mi investigación en estos temas se desarrollan en las primeras secciones de este informe. En el apéndice de este trabajo he agregado las publicaciones en discusión.

Desde hace más de un año trabajo en el desarrollo de sistemas ópticos controlados por sistemas electrónicos de alta banda en el rango de los Megahercios. En este caso no investigo para demostrar cierto tipo de efecto, sino trabajo en la mejora de sistemas ya establecidos y su proceso de integrarlos en productos comercialmente atractivos.
Si bien ahora mi trabajo esta centrado en la ingeniería y el desarrollo de productos comerciales, mi entusiasmo por la física no ha cambiado. Ahora investigo y publico mis resultados de manera independiente en mi tiempo libre sin la condicional de un financiamiento o un superior.

Agradecimientos

Agradezco a mi padre, quien me motivó a redactar este informe.

Tabla de contenidos

1. Introducción

Cuando se aplica un campo eléctrico sobre un cuerpo, los electrones y las moléculas se reordenan a lo largo del campo eléctrico externo, formando regiones positivas y negativas. Este reordenamiento es conocido como polarización. En un medio linear la magnitud de la polarización $\vec{P}$ es propócional al campo eléctrico externo E^j, siguiendo la formula: $P_i = \epsilon_0 \chi_{ij}^{(1)}(\omega) E^j$, donde ϵ_0 es permitividad del vacío, $\chi_{ij}^{(1)}(\omega)$ es un tensor denominado susceptibilidad eléctrica[1], que depende de la frecuencia y la dirección del campo eléctrico aplicado. A grandes amplitudes del campo eléctrico, reacciones no lineales de la polarización se pueden comenzar a apreciar. Esto sucede porque los electrones en los latices de los cristales, debido al alto campo eléctrico externo, oscilan con amplitudes que difieren de los osciladores armónicos simples[2]. Este comportamiento de los electrones ligados es reflejado en la polarización como una respuesta no linear y es fenomenologicamente descrita como:

$$P_i = \epsilon_0 \chi_{ij}^{(1)}(\omega_i;\omega_j) E^j + \epsilon_0 \chi_{ijk}^{(2)}(\omega_i;\omega_j,\omega_k) E^j E^k + \epsilon_0 \chi_{ijkl}^{(3)}(\omega_i;\omega_j,\omega_k,\omega_l) E^j E^k E^l \cdots , \tag{1}$$

donde $\chi^{(2)}$ es un tensor de tercer rango y es denominado susceptibilidad eléctrica de segundo orden, $\chi^{(3)}$ es un tensor de cuarto orden y es denominado como susceptibilidad eléctrica de tercer orden. Teoréticamente hay infinitas ordenes de susceptibilidad pero sus valores decrecen dramáticamente con el orden. Por ejemplo, para GaAs a una longitud de onda $\lambda_0 = 1{,}06$ μm se tiene $\chi^{(1)} = 11{,}04$ [1], $\chi^{(2)} = 94$ pm/V [2], $\chi^{(3)} = 1{,}4 \cdot 10^{-18}$ m^2/V^2 [1], etc.

En el presente informe se restringe solo a la interacción de segundo orden en cristales. La cual permite dos efectos que se les denomina conversión de suma y de resta de frecuencias. En el caso de dos ondas viajeras con frecuencia ω_1 y ω_2, se puede demostrar que la polarización de segundo orden

$$P_j^{(2)} = \epsilon_0 \chi_{ijk}^{(2)}(\omega_i;\omega_1,\omega_2) E_1^j E_2^k \tag{2}$$

[1] En caso de materiales isotrópicos la polarización es siempre en sentido contrario al campo eléctrico.

[2] Muy similar a los péndulos cuando la aproximación $\sin(\theta) \approx \theta$ deja de ser adecuada.

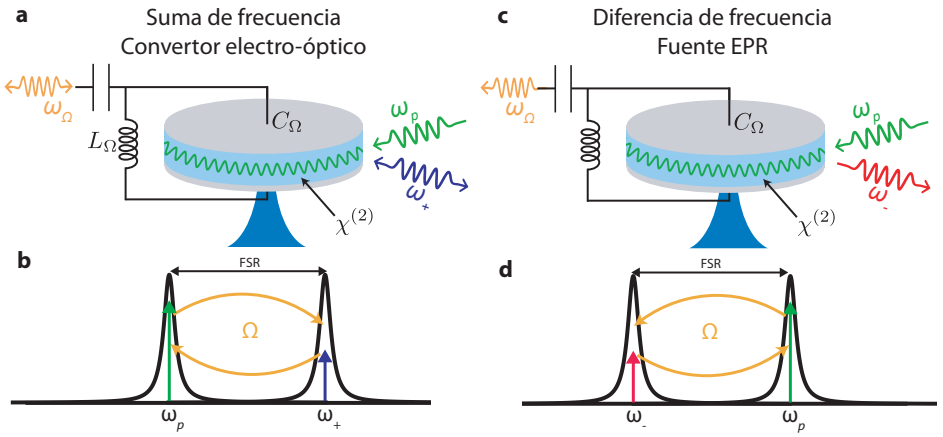

Figura 1: Un resonator óptico de medio no lineal $\chi^{(2)}$ es confinado entre dos electros formando una capacitancia C_Ω en un resonador de microondas con frecuencia de resonancia $\Omega = 1/\sqrt{L_\Omega C_\Omega}$. (a) Una señal de microondas es enviada a la cavidad, esta interacciona con la campo óptico ω_p y es convertida en una señal óptica de frecuencia ω_+, este proceso convierte también señales ópticas a microondas. (b) Espectro del resonador óptico. Los dos modos del resonador óptico corresponden al modo central y al modo adjacente con frecuencias de resonancia ω_c and ω_{as}. Interacción electro-óptica requiere que Ω coincida con el rango espectral libre (FSR) óptico. En el esquema el resonador es alimentado por una fuente coherente con la frecuencia de resonancia $\omega_p = \omega_c$ y la señal de microondas convertida sale del sistema con frecuencia $\omega_+ = \omega_{as}$. (c)Una fuente óptica incidente a una frecuencia ω_p es convertida en dos campos electro-ópticos correlacionadas Ω and ω_-. (d) Los dos modos del resonador óptico corresponden al modo central y al modo adjacente con frecuencias de resonancia ω_c and ω_s. En el esquema el resonador es alimentado por una fuente coherente con la frecuencia de resonancia $\omega_p = \omega_c$ y la salida del resonador óptico es la linea de Stokes a la frecuencia $\omega_- = \omega_s$.

oscila con la frecuencias $\omega_+ = \omega_2 + \omega_1$ y $\omega_+ = \omega_2 - \omega_1$, las cuales corresponden a la suma (SF) y a diferencia (DF) de las ondas iniciales. Además, las oscilaciones de la polarización no lineal pueden crear ondas de frecuencia $\omega_\pm$, si cumplen el requerimiento llamado coincidencia de fase: $\vec{k}_\pm = \vec{k}_2 \pm \vec{k}_1$, donde $\vec{k}$ es el número de onda. Las ondas creadas como bandas de anti-Stokes (ω_+) y Stokes (ω_-). Similarmente este estudio se puede extender al nivel cuántico donde la relación de las frecuencias se refiere a la conservación de energía y el coincidencia de fase con la conservación del momento.

En algunos sistemas se pueden aislar dos modos ópticos que pueden interactuar con un tercer modo en microondas, como será descrito en los siguientes capítulos. En la figura 1a y b se puede observar que si la onda óptica es enviada al modo óptico de menor frecuencia, se puede hacer lo que se denomina conversión de frecuencia electro-óptica. En la figura 1c y d la onda óptica inicial es envia-

da al modo óptico de mayor frecuencia, el cuál genera dos nuevas frecuencias produciendo lo que se denomina conversión parametric espontánea (Spontanous parametric down-conversion SPDC).

2. Peine de frecuencias ópticas

2.1. Descripción y contexto

El internet ha sido sin duda una de las invenciones que más influencia ha tenido en todas las sociedades alrededor del mundo. Este invento es posible debido a nuestro sistema global de telecomunicaciones, en el cual se envía información en una onda electromagnética, que se le denomina carrier. Generalmente, se varía la intensidad de la onda carrier, conocida como modulación de amplitud (AM), o se varía la fase (PM), conocida como modulación de fase. En estas variaciones arbitrarias, ya sea de amplitud o de fase, se codifica la información a transmitir y define un canal de telecomunicación. El mayor intercambio de información en esta red mundial de telecomunicaciones sucede en redes de fibras ópticas transoceánicas. El éxito de este tipo de sistemas se debe a las bajas pérdidas en la propagación de la señal a través de las fibras ópticas (0.02 dB/km) y a la capacitad para poder hacer multiplexación por división de longitud de onda (WDM), donde cientos de señales a distintas frecuencias, separadas en 40 GHz entre ellas, son combinadas y enviadas a través de una misma fibra óptica. Estas señales son generalmente producidas por varios láseres individuales cuyas frecuencias son estabilizadas entre sí.

Los peines de frecuencias ópticas son sistemas en los cuales varias líneas ópticas equidistantes espectralmente, son creadas de una sola fuente. Esta herramienta no solo sirve como una regla en el espacio espectral, sino también proporciona una fuente en la cual las líneas de emisión tienen propiedades como coherencia y estabilidad entre las intensidades y fases relativas a la fuente inicial.

En los últimos años se ha planteado la sustitución de los láseres individuales por peines de frecuencias para los sistemas WDM en las telecomunicaciones. Debido a sus beneficios como ancho de banda, coherencia, la estabilidad en las distancias espectrales, y a la reducción en los costos energéticos comparados un arreglo grande de láseres activamente estabilizados.

Un peine de frecuencias se puede generar en sistemas como moduladores de fase, donde la fuente es una señal óptica y una segunda onda moduladora, cuya frecuencia va a determinar el espacio espectral entre las líneas espectrales generadas. El

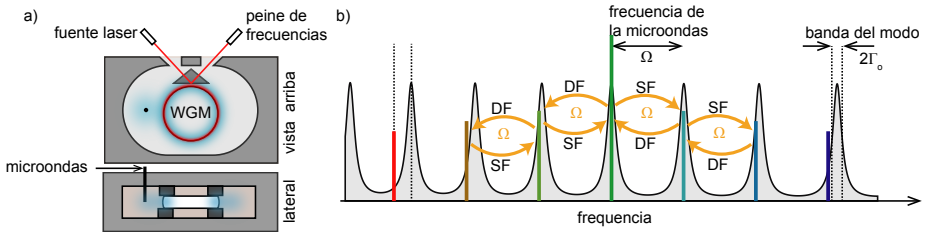

Figura 2: Principio para generar peines de frecuencia ópticas con $\chi^{(2)}$. (a) Diagrama del montaje para crear peines de frecuencia, un resonador WGM de niobato de litio con alta finesse es colocado en una cavidad conductora hecha de cobre. La luz es acoplada via la reflexión total internal en la interfase de un prisma y el resonador. La señal de microondas es enviada por medio de una antena adentro de la cavidad. El diseño de la cavidad enfoca el campo eléctrico del microondas al borde del resonador óptico, amplificando el efecto Pockels. (b) La ilustración muestra como el campo de la onda de microondas origina la creación del peine de frecuencias por el efecto Pockels. Los modos ópticos en un resonator esta separados por el rango de frecuencia libre, que coincide con la frecuencia de microondas Ω, permitiendo la creación de ondas por medio de la suma (SF) y diferencia de frecuencia (DF) indicadas con líneas verticales de colores. Dada una frecuencia de microondas las líneas generadas son equidistantes y estas llevan a un detuning con los modos ópticos (indicados por las líneas de forma Lorentzianas), que eventualmente termina limitando la creación de nuevas frecuencias.

gran problema de estos tipos de artefactos es el consumo energético enorme de la onda moduladora para la generación de las líneas. Además, debido a la misma naturaleza del efecto, las amplitudes de las líneas siguen la funciones de Bessel las cuales oscilan con la creación de más líneas, llegando a cero en algunas configuraciones. Debido a estas razones, peines de frecuencias creados por $\chi^{(2)}$ dejaron de ser de interés.

En los últimos años, la creación de peines de frecuencias ópticas se concentro entonces en el uso del efecto Kerr, el cual necesita solo una onda como fuente para crear el peine. Para aumentar la eficiencia de este efecto, el uso de microresonadores de una finesse alta es necesaria [3].

2.2. Resultados

En la publicación *Resonant electro-optic frequency comb* en 2019 en la revista *Nature* [4], reportamos un sistema multiresonante capaz de generar un peine de frecuencias que cubre la zona C-Band.

El esquema para la generación del peine de frecuencias se baso en uso de un whispering gallery mode resonador óptico (WGMR), hecho de un cristal niobato

de litio, el cual confina la luz a través de reflexion interna total. Este resonador es colocado en el centro de un cavidad de microondas resonante a la frecuencia Ω, que coincide con el espectro libre del resonador óptico (FSR). Por la geometría de los dos resonadores, los campos eléctricos de microondas y el óptico son enfocados al borde del resonador óptico, amplificando el efecto proporcionalmente a la finesse de las cavidades. Cuando se envía la onda óptica y de microondas, estas crean las líneas de Stokes y anti-Stokes, estas interaccionan con la onda moduladora produciendo líneas nuevas. Este proceso se sigue extendiendo creando el peine de frecuencias como se muestra en la Fig.2. Entre los méritos de esta publicación se encuentran:

- Se logró tener el sistema con el consumo de energía (voltage π) más bajo en sistemas electro-ópticos, estableciendo un nuevo record.

- Se estudió la creación de las líneas ópticas en estos tipos de sistemas resonantes. A diferencia de los sistemas no-resonantes, estos no son descritos por las funciones de Bessel. El logro en la parte teórica fue encontrar una solución analítica la cual describe las amplitudes y la fases relativas de las líneas ópticas basadas solo en variables adimensionales de uso experimental.

- Se demostró los límites en el ancho de banda de los peines de frecuencias como función de la intensidad de la onda moduladora y la dispersión del material.

- Se demostró experimentalmente los comportamientos del sistema descrito por la teoría.

El uso de los sistemas resonantes ayudan a poder amplificar cierto tipo de efecto por varias ordenes de magnitud. Esto ayudo a bajar el consumo energético de la onda moduladora. Además, las amplitudes de las lineas decrecen monótonamente con el orden y no oscilan. Esto ha despertado el interés en investigar peines de frecuencias basados en el efecto Pockels. Este proyecto lo realicé en su mayoría solo: experimento y teoría, bajo la supervisión de Prof. Harald Schwefel y Dr. Florian Sedlmeir.

3. Conversión electro-óptica al nivel cuántico

3.1. Descripción y contexto

En los últimos años ha habido un desarrollo exponencial en tecnologías cuánticas. Entre estas, los circuitos superconductores, emergen como los sistemas más prometedores para ser las piezas elementales en el desarrollo de las computadoras cuánticas comerciales. Debido a su facilidad en el control a través de campos magnéticos. En el 2019, Google presentó su primera computadora cuántica, probando la supremacía sobre las computadoras convencionales o clásicas, marcando un hito en el desarrollo de estas [5]. Un circuito superconductor consiste de los elementos clásicos como inductores y capacitores, y de un elemento llamado unión de Josephson, que es un elemento no lineal y no disipativo con el cual se puede construir sistemas cuánticos con niveles energéticos arbitrarios por eso también llamados átomos artificiales [6]. Mayormente, se preparan estos tipos de sistemas para que el primer nivel, generalmente llamado ground, y el segundo nivel, llamado excited, estén aislados de los otros niveles energéticos y evitar cualquier tipo de interacción con ellos. Por eso, el sistema solo puede estar en una superposición de dos estados y recibe la nominación de qubit. En el caso especifico de los qubit desarrollados por Google and IBM, la diferencia energética entre los dos primeros niveles es dada por $h\nu$, donde h es la constante de Planck y ν equivale a frecuencia en el rango de los gigahercios. Es en esta propiedad que aparece el primer problema técnico de estos sistemas, debido a esta baja frecuencia, el ruido proveniente de la radiación de cuerpo negro de los alrededores en temperatura de ambiente puede fácilmente alterar el estado cuántico del sistema. Por eso, se necesita aislar estos circuitos en criostatos que pueden llegar a una temperatura alrededor de los 20 milikelvins, manteniendo estos sistemas aislados. El siguiente paso es la computación cuántica es la interconexión. Si se desea que dos cluster de qubits estén interconnectados se puede lograr a través del intercambio de fotones que viajan por un guía de ondas que tiene que mantenerse a temperaturas criogenicas para no destruir el estado cuántico que transporta. Esto es viable para distancias de hasta algunos metros [7], pero no para largas distancias, ya que el costo de la infraestructura y mantenimiento de estos canales son inviables.

Convertores de frecuencia electro-ópticos son la clave para el progreso de la computación cuántica. La idea es que los fotones mensajeros con frecuencias de gigahercios sean convertidos a fotones ópticos, cuyas frecuencias están el los cientos de terahercios donde el ruido de fondo a temperatura de ambiente es despreciable. Así, estos fotones ópticos mensajeros pueden ser llevados por fibra óptica u otros métodos estándares a la siguiente computadora cuántica ubicada a varios kilómetros. Al arribo a la siguiente computadora cuántica, el fotón mensajero óptico es reconvertido en un fotón de microondas para su procesamiento. Idealmente, estos convertores deben tener una eficiencia de conversión unitaría en las dos direcciones, con ancho de banda (compatible con los sistemas superconductores de qubits en el orden de los MHz) [6] y adherir un ruido a la conversion muy debajo de un photon.
En años recientes ha existido un rápido crecimiento en los esfuerzos en este dirección utilizando diferentes métodos, de los cuales los sistemas electro-optomecánicos y electro-ópticos sobresalen más. Sistemas del primer tipo utilizan un sistema mecánico resonante para interconectar el campo óptico con el microondas. Sistemas electro-optomecánicos han reportado una eficiencia de conversion de 47 %, pero con un ancho de banda muy bajo BW $= 10$ kHz [8]. Además, debido a la baja frecuencia de resonancia mecánica este sistema adhiere un ruido alto de conversión N_{add} estos sistemas se mantienen en el limite clásico [8]. Sistemas del segundo tipo tienen anchos de banda arriba de los MHz y su eficiencia a subido exponencialmente yendo de 0.1 % [9] a ~ 25 % [10]. Además, por la ausencia del intermediario mecánico, el ruido adherido a la conversión puede suprimirse hasta volverse despreciable.

3.2. Resultados

En Institute of Science and Technology Austria, trabajé con un sistema similar al presentado en la sección anterior. En este caso se tuvo que aislar dos modos ópticos en el resonador para evitar efectos como la interacción con otros modos ópticos que podrían generar efectos como conversion de diferencia de frecuencias como ilustrado en la figura 3a. Este sistema se implemento en un criostato y se mantuvo a una temperatura de 10 mK. En la publicación *Bidirectional electro-*

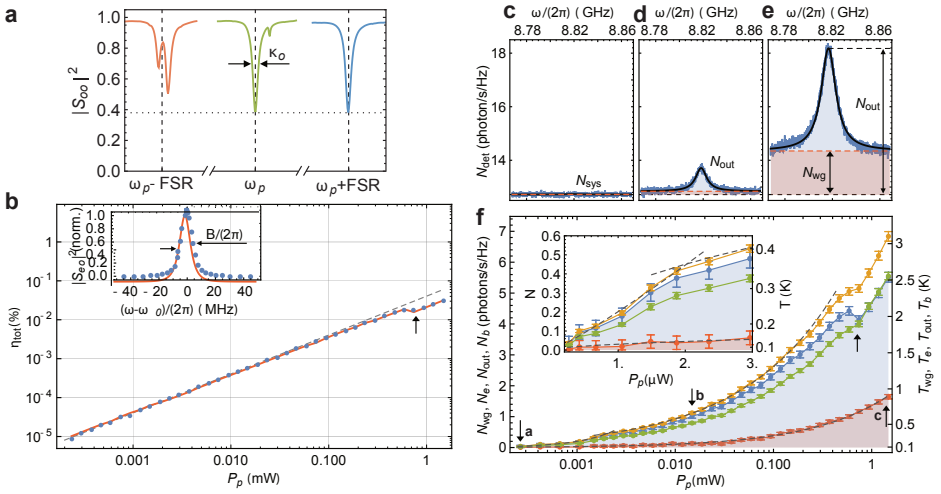

Figura 3: Conversión a temperaturas criogenicas **a** Espetro óptico del resonador. **b** Eficiencia en función del bombeo óptico. **c**, **d**, **e** Espectro del ruido térmico en el regimen de microondas (línea azul) en unidades de photones $\mathrm{s}^{-1}\,\mathrm{Hz}^{-1}$ para (c) $P_p = 0{,}23\,\mu$W, (d) $14.82\,\mu$W and (e) 1.48 mW juntos a una curva de ajuste teórica (linea negra). En los tres paneles se muestra las mediciones del ruido del sistema de medición N_{sys} y en las lineas discontinuas rojas indican el ruido térmico de banda ancha proveniente de la guía de ondas de microondas N_{wg}. (d) Población del ruido en el guía de ondas N_{wg} (rojo), ruido total la salida del sistema N_{out} (azul), ruido interno del sistema N_b (amarillo) y ocupancia del modo de microondas N_e (verde) como función de P_p. Las barras de errores de N_{wg} y N_{out} a bajos valores de P_p están dominadas por el error sistematico debido a variación lenta del ruido del sistema de medición $\pm 0{,}03$ cuantos. Los errores de barras de N_b representan el 95 % de intervalo de confidencia del la curva de ajuste teórica que también domina la incertidumbre de N_e since $N_{\mathrm{wg}} < N_{\mathrm{b}}$. Las barras de error para altos valores de P_p son dominados por la precisión de la calibración de N_{sys}.

optic wavelength conversion in the quantum ground state en 2020 publicado en el Journal PRX quantum [11] se obtuvo los siguientes logros:

- Se demostró conversión en el estado fundamental $(N_{\mathrm{add}} < 1)$ para un uso de fuente de bombeo continua [11].
- Se demostró un ancho de banda de BW $\geq$ 10 MHz.
- Se demostró bidirecionalidad en la conversión.

Estos resultados están resumidos en la figura 3b. Donde se presenta la curva de la eficiencia en función de la potencia del bombeo óptico. El efecto de la absorción óptica en la temperatura del sistema, y por ende en el ruido térmico, puede ser apreciada en la figura 3c,d ye, donde se puede identificar el ruido proveniente del

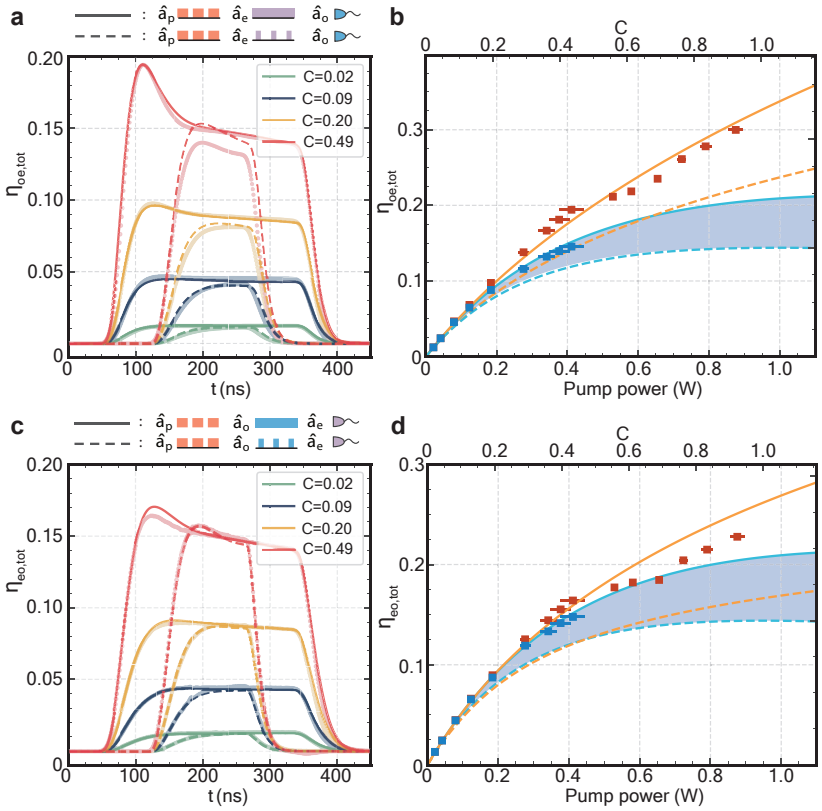

Figura 4: Conversión a cooperatividades altas. a (**c**), Señales coherentes convertidas con una bomba pulsada con duración de 300 ns y una señal de entrada constante, medidas con una repetición de 500 Hz a diferentes valores de cooperatividad. **b** (**d**), eficiencias de conversión en la semi-constante de la conversión pulsada (cuadrados azules) y eficiencia en el pico (cuadrados rojos) a distintos valores de la cooperatividad. Las barras verticales y horizontales representan la desviación estándar de los valores medidos.

sistema resonante de microondas (curva lorentziana) N_{out} y el ruido térmico del criostato N_{WG} (corresponde al offset de la curva Lorentziana). En la figura 3f se muestran los en distintas partes del sistema como en la guía de onda N_{WG}, ruido efectivo del modo N_{e}, ruido total de salida N_{out} y el ruido interno N_{b} para distintas potencias ópticas.

Debido a la capacidad y resistencia térmica del sistema, el tiempo característico de los cambios de temperatura es por los varias decenas de segundos. Dejando la posibilidad de una pulsación en un rango de tiempo relativamente corto como en los microsegundos y repeticiones debajo de los kHz. En una publicación pos-

terior se trabajó con este tipo de bombeo pulsado a amplitudes altas, llegando a cooperatividades cercanas a la unidad, sin calentar el sistema a niveles relevantes. En *Quantum-enabled interface between microwave and telecom light* [10] en 2021 se obtuvo los siguientes logros:

- Se demostró en el estado fundamental $(N_{\text{add}} < 1)$ una conversión de 25 % en un uso de fuente pulsada [10].
- Se demostró bidirecionalidad en la conversión.

En el modo de fuente pulsada se logró una conversion por encima de los 20 % por lapsos de unos 300 ns con una repetición de un 0.5 kHz como se muestra en la figura 4. La asimetría de los valores pico iniciales es debido a los distintos valores del acoplamiento de los sistemas a sus respectivas guías de onda. Estos rangos de tiempo son compatibles con la mayoría de fuentes de un fotón solo en el régimen de microondas en la parte espectral y también en la tasa de creación. La cooperatividad alta alcanzada abre el camino para nuevos experimentos en el regimen electro-óptico donde otros efectos como retroacción dinámica adibática, conversión paramétrica espontánea (SPDC), entre otros.

La publicación en la referencia [11] lo llevé acabo de manera conjunta con Dr. William Hease, con el cual comparto la primera autoría. En la publicación [10] trabajé en la parte experimental y teórica hasta que deje IST-Austria, pasando a asesorar el proyecto hasta su culminación.
El futuro de los convertores electro-ópticos tiene una perspectiva muy buena con base en el desarrollo y mejor dominio de la nanofabricación de materiales como niobato de litio y tantalio o nitrato de aluminio. Esta miniaturización permitirá una amplificación del efecto que no es posible en sistemas milimétricos. Este tipo de investigación se lleva principalmente en dos Grupos uno en Harvard con Prof. Loncar y otro en Yale con Prof. Tang.

4. Investigación teórica del enmarañamiento electro-óptico

4.1. Descripción y contexto

Uno de las efectos cuánticos más populares fuera de la comunidad física es la teletransportación. En los noventa se logró transportar los primeros estados cuánticos en los trabajos pioneros de Bouwmeester y Furusawa [12, 13]. Casi 20 años después es la teletransportación de estados un experimento bastante común en laboratorios de óptica cuántica. El efecto cuántico detrás de la teletransportación es el enmarañamiento cuántico. Este generalmente se crea cuando una partícula decae en dos, cuyas cantidades cuánticas como energía, momentum, spin, etc quedan conectadas a pesar de esta estar separadas espacialmente. Este efecto es no local porque los cambios en una partícula genera un cambio inmediato en la otra. Este efecto sumado un protocolo de mediciones de Bell y transferencia de información clásica, permiten lo que se conoce como teletransportación cuántica [13].
Para comprobar si la transportación del estado fue exitosa se compara el estado inicial con el estado final en una métrica que va desde 0 a 1 llamado fidelidad. En los últimos años la fidelidad estándar en los experimentos ha ido mejorando y valores mayores a 0.9 sobre extensión de decenas de kilómetros ya son realidad [14].
En el contexto de telecomunicaciones, para que la teletransportación sea efectiva, se necesita una fuente proveedora de fotones enmarañados. La fuente para el uso de teletransportación se les llama Einstein-Podolski-Rosen, por las correlaciones cruzadas que de los dos fotones emitidos presentan. Este tipo de fuentes se pueden caracterizar y describir a través de la matriz de covarianza de los campos de los campos emitidos. En el regimen óptico, estas fuentes han sido estudiadas y perfeccionadas en las ultimas décadas permitiendo otros protocolos de telecomunicaciones como código denso [15].
Idealmente, una fuente EPR híbrida no solo permitiría una teletransportación de estados cuánticos a una distancia arbitraria, sino también cambiaría la frecuencia del estado. De esta manera habría una conversión de frecuencia inmediata del estado, introduciendo un nuevo esquema para la telecomunicación de dos computadoras cuánticas unidad por un canal óptico.

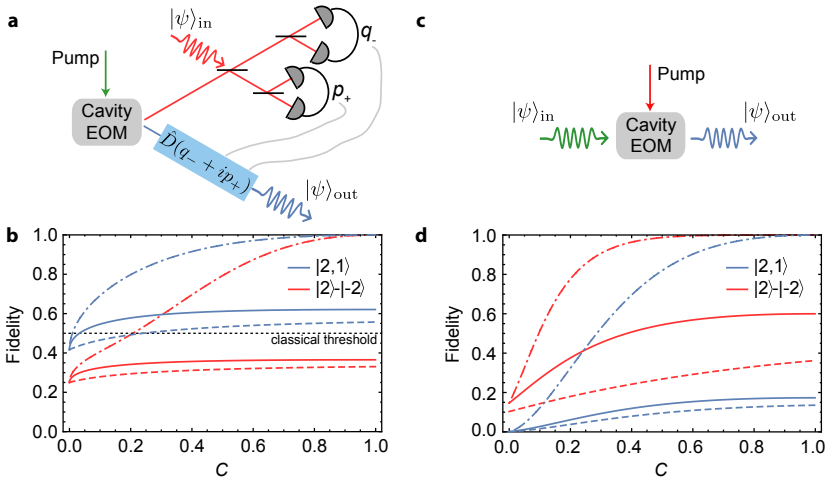

Figura 5: Transferencia de estado cuántico. (a) Esquema de teletransportación electro-óptico. El emisor mezcla un estado cuántico no conocido $|\psi\rangle_{\text{in}}$ con brazo de la fuente enmarañada usando un partidor de rayo 50:50 y hace las mediciones de Bell correspondientes de q_- y p_+. Esta información es enviada por un canal clásico al receptor en el régimen de microondas, donde este aplica el desplazamiento apropiado en el espacio de fase en el segundo brazo de la fuente de enmarañamiento, completando la transferencia del estado. (b) Cálculo de la fidelidad de la teletransportación para un estado coherente squeezed inicial $|\psi\rangle_{\text{in}} = |\alpha = 2, r = 1\rangle$ (líneas azules) y estado de gato de Schrödinger $|\psi\rangle_{\text{in}} = |2\rangle - |-2\rangle$ (líneas rojas) para los parámetros experimentales η_o =0.5 y η_Ω =0.8 (líneas solidas), a la elevada temperatura interna de $T_b = 800$ mK (líneas discontinuas) y para el caso de un sistema sin pérdidas $\eta_\Omega = \eta_o = 1$ (líneas discontinuas punteadas). (c) Esquema de conversion directa descrita en la sección anterior. (d) Cálculo de la fidelidad en usando conversión directa para una estado cuántico inicial coherente squeezed $|\psi\rangle_{\text{in}} = |\alpha = 2, r = 1\rangle$ (líneas azules) y para un estado de gato de Schrödinger $|\psi\rangle_{\text{in}} = |2\rangle - |-2\rangle$ (lineas rojas) para parámetros experimentales η_o =0.5 y η_Ω =0.8 (líneas solidas), a una temperatura interna elevada $T_b = 800$ mK (líneas discontinuas) y para el caso de un sistema sin pérdidas $\eta_\Omega = \eta_o = 1$ (líneas discontinuas punteadas).

4.2. Resultados

En la publicación *Electro-optic entanglement source for microwave to telecom quantum state transfer* de noviembre del 2019 en la revista *npj* quantum information [16], se tomó como punto de salida un sistema multiresonantes con dos modos ópticos y un modo de microondas que cumplen las condiciones de energía y coincidencia de fase como ilustrado en la figura 1b. Tomando solo en cuenta la interacción no lineal $\chi^{(2)}$, se demostró lo siguiente:

- Primer resultado analítico de la matriz de covarianza para sistemas resonantes en presencia de pérdidas y ruido térmico.

- Se calculó la calidad y cantidad de número de bits enmarañados producidos por el sistema.
- Se trató de romper el paradigma conversión directa para la inter-comunicación entre sistemas en microondas y sistemas ópticos por un esquema, donde la teletransportación reemplaza la conversión de frecuencia.
- Se presentó resultados analíticos fidelidad como función de parámetros experimentales adimensionales para cierto tipos de de estados.
- Se comparó los valores de la fidelidad de los esquemas de teletransportación y conversión directa de un sistema electro-óptico genérico, demostrando su dependencia de los estados iniciales.

Los puntos antes mencionados llamaron la atención de la comunidad logrando 19 citaciones en su primer año de publicación. Gracias a su generalidad puede ser usada para otro tipo de sistemas fuera de los electro-ópticos. En la figura 5 se puede observar que el mismo sistema operado en maneras distintas maneras puede mejorar el performance en la conversión de frecuencia de algunos estados. Para comparar se tomo el ejemplo de dos estados como los gatos de Schrödinger $|\psi\rangle_{\text{in}} = |2\rangle - |-2\rangle$ y estados coherentes squeezed. $|\psi\rangle_{\text{in}} = |\alpha = 2, r = 1\rangle$. Tomando como ejemplo el caso de un sistemas sin pérdidas $\eta_\Omega = \eta_o = 1$ se ve que los estados de coherentes squeezed son favorecidos con un protocolo de teletransportación y los estados de Schrödinger son favorecidos con la conversión directa.

El trabajo teórico de esta publicación lo realicé solo y estuve bajo la supervisión del Prof. Fink y Prof. Barzanjeh. Actualmente se esta trabajando en la primera demostración de una fuente electro-óptica de EPR, en las cuales me mantengo como miembro semi-activo, ayudando en la interpretación de datos.
Este último febrero publiqué un investigación teórica en Physical Review A, con el título *Frequency-multiplexed hybrid optical entangled source based on the Pockels effect* [17], donde estudié los efectos de multi-enmarañamiento y la creación de un peine de frecuencia óptica enmarañada. Esta publicación no forma para de este reporte debido a que no es parte de mi actividad laboral principal, sino de mi afición.

5. Desarrrollo de FMCW-LiDAR en Scantinel Photonics GmbH.

5.1. Descripción y contexto

En Scantinel Photonics GmbH, comencé el primer año como ingeniero de laboratorio y el segundo año ascendí a Senior lab scientist. En esta posición estoy encargado de todo lo que respecta al funcionamiento del hardware de los sensores de LiDAR y su funcionamiento adecuado con el software controlador. Un LiDAR funciona en la base de enviar una señal óptica en cierta dirección y detectar la señal reflejada (figura 6a). Dependiendo del esquema a usar se puede detectar la distancia del objetivo a través de la diferencia en el tiempo del envío de la señal y su detección, llamado tiempo de vuelo τ y la velocidad del objeto detectado a través del desplazamiento Doppler en la frecuencia. Nosotros desarrollamos tecnología de FMCW-LiDAR, esto significa que nuestra fuente es continua y su frecuencia oscila de manera triangular en el tiempo. A esto le denominamos Up-chirp y Down-chip (figura 6b). De la fuente una parte se separa y se mantiene como el oscilador local y la otra parte se envía en la dirección de detección requerida (figura 6a). La señal reflejada es acoplada al sistema y combinada con el oscilador local. La señal óptica resultante es convertida en una corriente electronica en el fotodetector. A esta se le aplica la tranformación de Fourier para poder hallar la frecuencia de pulsación. La frecuencia de pulsación con el upchirp f_{up} y con el downchirp f_{down} generalmente son distintas debido al efecto Doppler. El promedio de estas frecuencias $\Delta f = (f_{\text{up}} + f_{\text{down}})/2$ va a ser dos veces el tiempo de vuelo por la razón cambio de la frecuencia $\Delta f = 2\gamma\tau$ (figura 6b) y la resta entre las frecuencias de diferencia entre el up- y downchirp serán proporcionales a la velocidad relativa del objecto $v \sim f_{\text{up}} - f_{\text{down}}$.
Esta tecnología de radares ópticos ofrece una mejor resolución espacial que sus contrapartes en radiofrecuencia (RADAR) or ultrasonido (SONAR), debido a su corta longitud de onda. El objetivo de la empresa es llevar esta tecnología de una manera comercialmente atractiva a la industria automovilística y es una pieza elemental para la navegación autónoma, ya que esta necesita sensores capaces de detectar e identificar obstáculos de areas menores a un m^2 a más de 150 metros de

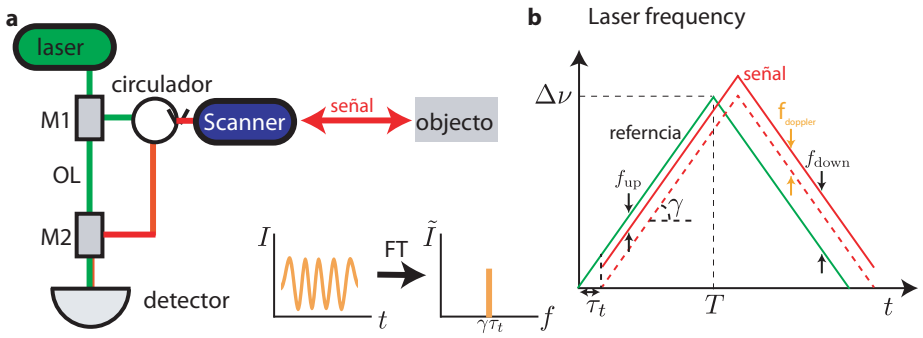

Figura 6: FMCW LiDAR. (a) la señal de un laser, cuya frecuencia varía en el tiempo, es separada en dos en el partidor M1. Una parte va como referencia (OL) y la otra es enviada a la dirección a detectar por medio de un circulador. La señal reflejada es combinada con la referencia en M2 y detectada. De la señal temporal en el fotodetector, se aplica a transformación de Fourier, de la cual las frecuencia de pulsación f_{up} o f_{down} son extraídas. (b) Función de la frecuencias de referencia y de la señal en el tiempo. Si el objeto estuviera estático la diferencia entre las frecuencia de referencia y la señal serían constantes durante el up- y downchirp.

distancia.

En Scantinel Photonics GmbH el desarrollo y mejoras de los módulos que integran los sensores de LiDAR están bajo secreto empresarial. Por ello solo enlistaré mis labores generales en la empresa.

- Desarrollo e investigación en la estabilidad de emisión y linearización del barrido de frecuencia en las fuentes del laser. La resolución de la distancia depende linearmente de la homogeneidad de barrido de la frecuencia y esta es la que limita en mayor parte la resolución radial del LiDAR.

- Soluciones al empacamiento y el manejo térmico de los productos. A causa de los muchos componentes empaquetados juntos en volúmenes pequeños, la disipación del calor se vuelve fundamental para mantener el performance de las distintas piezas. Además, el producto final debe funcionar a temperaturas entre los -20 a +80 °C.

- Elaboración de los montajes y protocolos para verificación y certificación el performance los de los distintos módulos ensamblados en los sensores. Cada componente de los LiDAR deben de verificarse que funcionan en el rango de los parámetros establecidos por diseño. Esto involucra no solo calibración de los módulos, también el arreglo de montages para la medición de estos.

6. Conclusiones

En el presente trabajo se puede observar que que he hecho un aporte en el desarrollo de sistemas electro-ópticos para aplicaciones clásicas y cuánticas. Además, ahora empleo mis conocimientos experimentales aprendidos en la optimización de sistemas electro-ópticos para la industria.

7. Referencias bibliográficas

Referencias

[1] R. Boyd, Nonlinear Optics. Elsevier Science, 2003.

[2] T. Skauli, K. L. Vodopyanov, T. J. Pinguet, A. Schober, O. Levi, L. A. Eyres, M. M. Fejer, J. S. Harris, B. Gerard, L. Becouarn, E. Lallier, and G. Arisholm, "Measurement of the nonlinear coefficient of orientation-patterned GaAs and demonstration of highly efficient second-harmonic generation," Opt. Lett., vol. 27, pp. 628–630, Apr 2002.

[3] T. J. Kippenberg, A. L. Gaeta, M. Lipson, and M. L. Gorodetsky, "Dissipative kerr solitons in optical microresonators," Science, vol. 361, no. 6402, 2018.

[4] A. Rueda, F. Sedlmeir, M. Kumari, G. Leuchs, and H. G. L. Schwefel, "Resonant electro-optic frequency comb," Nature, vol. 568, no. 7752, pp. 378–381, 2019.

[5] F. Arute, K. Arya, R. Babbush, D. Bacon, J. C. Bardin, R. Barends, R. Biswas, S. Boixo, F. G. S. L. Brandao, D. A. Buell, B. Burkett, Y. Chen, Z. Chen, B. Chiaro, R. Collins, W. Courtney, A. Dunsworth, E. Farhi, B. Foxen, A. Fowler, C. Gidney, M. Giustina, R. Graff, K. Guerin, S. Habegger, M. P. Harrigan, M. J. Hartmann, A. Ho, M. Hoffmann, T. Huang, T. S. Humble, S. V. Isakov, E. Jeffrey, Z. Jiang, D. Kafri, K. Kechedzhi, J. Kelly, P. V. Klimov, S. Knysh, A. Korotkov, F. Kostritsa, D. Landhuis, M. Lindmark, E. Lucero, D. Lyakh, S. Mandrà, J. R. McClean, M. McEwen, A. Megrant, X. Mi, K. Michielsen, M. Mohseni, J. Mutus, O. Naaman, M. Neeley, C. Neill, M. Y. Niu, E. Ostby, A. Petukhov, J. C. Platt, C. Quintana, E. G. Rieffel, P. Roushan, N. C. Rubin, D. Sank, K. J. Satzinger, V. Smelyanskiy, K. J. Sung, M. D. Trevithick, A. Vainsencher, B. Villalonga, T. White, Z. J. Yao, P. Yeh, A. Zalcman, H. Neven, and J. M. Martinis, "Quantum supremacy using a programmable superconducting processor," Nature, vol. 574, no. 7779, pp. 505–510, 2019.

[6] G. Wendin, "Quantum information processing with superconducting circuits: a review," Reports on Progress in Physics, vol. 80, p. 106001, sep 2017.

[7] P. Magnard, S. Storz, P. Kurpiers, J. Schär, F. Marxer, J. Lütolf, T. Walter, J.-C. Besse, M. Gabureac, K. Reuer, A. Akin, B. Royer, A. Blais, and A. Wallraff, "Microwave quantum link between superconducting circuits housed in spatially separated cryogenic systems," Phys. Rev. Lett., vol. 125, p. 260502, Dec 2020.

[8] A. P. Higginbotham, P. S. Burns, M. D. Urmey, R. W. Peterson, N. S. Kampel, B. M. Brubaker, G. Smith, K. W. Lehnert, and C. A. Regal, "Harnessing electro-optic correlations in an efficient mechanical converter," Nature Physics, vol. 14, no. 10, pp. 1038–1042, 2018.

[9] A. Rueda, F. Sedlmeir, M. C. Collodo, U. Vogl, B. Stiller, G. Schunk, D. V. Strekalov, C. Marquardt, J. M. Fink, O. Painter, G. Leuchs, and H. G. L. Schwefel, "Efficient microwave to optical photon conversion: an electro-optical realization," Optica, vol. 3, pp. 597–604, Jun 2016.

[10] R. Sahu, W. Hease, A. Rueda, G. Arnold, L. Qiu, and J. Fink, "Quantum-enabled interface between microwave and telecom light," 2021.

[11] W. Hease, A. Rueda, R. Sahu, M. Wulf, G. Arnold, H. G. Schwefel, and J. M. Fink, "Bidirectional electro-optic wavelength conversion in the quantum ground state," PRX Quantum, vol. 1, p. 020315, Nov 2020.

[12] D. Bouwmeester, J.-W. Pan, K. Mattle, M. Eibl, H. Weinfurter, and A. Zeilinger, "Experimental quantum teleportation," Nature, vol. 390, no. 6660, pp. 575–579, 1997.

[13] A. Furusawa, J. L. Srensen, S. L. Braunstein, C. A. Fuchs, H. J. Kimble, and E. S. Polzik, "Unconditional Quantum Teleportation," Science, vol. 282, no. 5389, pp. 706–709, 1998.

[14] R. Valivarthi, S. I. Davis, C. Peña, S. Xie, N. Lauk, L. Narváez, J. P. Allmaras, A. D. Beyer, Y. Gim, M. Hussein, G. Iskander, H. L. Kim, B. Korzh,

A. Mueller, M. Rominsky, M. Shaw, D. Tang, E. E. Wollman, C. Simon, P. Spentzouris, D. Oblak, N. Sinclair, and M. Spiropulu, "Teleportation systems toward a quantum internet," PRX Quantum, vol. 1, p. 020317, Dec 2020.

[15] K. Mattle, H. Weinfurter, P. G. Kwiat, and A. Zeilinger, "Dense coding in experimental quantum communication," Phys. Rev. Lett., vol. 76, pp. 4656–4659, Jun 1996.

[16] A. Rueda, W. Hease, S. Barzanjeh, and J. M. Fink, "Electro-optic entanglement source for microwave to telecom quantum state transfer," npj Quantum Information, vol. 5, no. 1, pp. 108–, 2019.

[17] A. Rueda, "Frequency-multiplexed hybrid optical entangled source based on the pockels effect," Phys. Rev. A, vol. 103, p. 023708, Feb 2021.

8. Apéndice

A continuación adjunto las publicaciones relevantes para este informe, que ya han sido publicadas en revistas arbitradas.

LETTER

https://doi.org/10.1038/s41586-019-1110-x

Resonant electro-optic frequency comb

Alfredo Rueda[1,2,3,4,5,6], Florian Sedlmeir[1,2], Madhuri Kumari[5,6], Gerd Leuchs[1,2,5,6,7] & Harald G. L. Schwefel[5,6]*

High-speed optical telecommunication is enabled by wavelength-division multiplexing, whereby hundreds of individually stabilized lasers encode information within a single-mode optical fibre. Higher bandwidths require higher total optical power, but the power sent into the fibre is limited by optical nonlinearities within the fibre, and energy consumption by the light sources starts to become a substantial cost factor[1]. Optical frequency combs have been suggested to remedy this problem by generating numerous discrete, equidistant laser lines within a monolithic device; however, at present their stability and coherence allow them to operate only within small parameter ranges[2–4]. Here we show that a broadband frequency comb realized through the electro-optic effect within a high-quality whispering-gallery-mode resonator can operate at low microwave and optical powers. Unlike the usual third-order Kerr nonlinear optical frequency combs, our combs rely on the second-order nonlinear effect, which is much more efficient. Our result uses a fixed microwave signal that is mixed with an optical-pump signal to generate a coherent frequency comb with a precisely determined carrier separation. The resonant enhancement enables us to work with microwave powers that are three orders of magnitude lower than those in commercially available devices. We emphasize the practical relevance of our results to high rates of data communication. To circumvent the limitations imposed by nonlinear effects in optical communication fibres, one has to solve two problems: to provide a compact and fully integrated, yet high-quality and coherent, frequency comb generator; and to calculate nonlinear signal propagation in real time[5]. We report a solution to the first problem.

The data capacity of the internet is expected to grow by a factor of two every year[6], but present optical techniques are not able to meet the rising demand on the bandwidth of the undersea fibre network[7]. Techniques such as space-division multiplexing[1], mode-division multiplexing[8] and wavelength-division multiplexing (WDM)[5] in combination with time-domain multiplexing are being investigated in order to exploit the existing network to its full capacity. Current WDM systems use an array of individually stabilized lasers, which are not phase locked to each other. For the next generation, a major shift in the paradigm—from multiple independent optical carriers to coherent optical frequency combs (OFCs)[7], combined with real-time numerical calculation of the nonlinear pulse[5]—will be necessary. The advantage of OFCs is that they can be generated from a single laser, which could reduce the overall energy consumption of the system considerably. Furthermore, depending on the method of comb generation, OFCs can feature high phase and frequency stability, and may also offer tunability of the comb's line spacing. Of particular interest for future WDM applications is the intrinsic phase lock between all comb lines, which allows the numerical counteracting of one of the main limitations—the nonlinear pulse distortion—in order to accept higher optical powers within the telecommunication fibres[5]. Commercial OFCs are at present based on femotosecond lasers[9,10]. However, over recent years, combs generated in microresonators via the third-order Kerr nonlinear four-wave mixing effect (whereby two pump photons are converted into a signal and idler photon)[2,10–12] and cascaded second-order parametric downconversion[13–15] have become more and more successful.

An alternative approach to comb generation is electro-optic modulation (EOM)[16]. This scheme exploits a second-order nonlinearity, whereby two continuous waves—for example, one in the optical range (the carrier wave) and one in the microwave range (the modulating wave)—are mixed within a nonlinear noncentrosymmetric crystal. In the past, overdriving of conventional electro-optic modulators has been explored for comb generation[17,18]. These EOM-based combs have unique advantages, such as tunable central frequency and comb-line spacing, which are crucial for applications from telecommunications to spectroscopy. However, these combs suffer from inherent phase instabilities and excess multiplication of microwave phase noise[18], which limits their usage in long-distance data transfer[5].

Here we report the experimental demonstration of efficient resonantly enhanced electro-optic comb generation. Such a fully coherent comb with intrinsic phase-noise suppression allows an increase in the information content and data rate in optical communication. The phase stability between the comb lines is inherent owing to the fixed interaction of two stable sources; high-quality optical resonators filter the fundamental electro-optic noise[18]. Our experiment draws on an in-depth theoretical description of the resonantly enhanced nonlinear interaction. We show in a first experiment the potential of this method, by describing a coherent comb with 8.9 GHz spacing and a span of almost 200 lines in the C-band (1,530–1,565 nm), using only 20 dBm of microwave modulation power. The results should spark a resurgence of interest in EOM-based comb generation, and show the potential of resonantly enhanced electro-optic modulation for the next generation of ultra-dense WDM.

The scheme we use for comb generation is based on the Pockels effect: an electric field applied to a noncentrosymmetric crystal, such as lithium niobate, results in a change in the optical refractive index of the material that is directly proportional to the applied voltage. As a consequence, light passing through the crystal encounters a varying optical path length and is thus phase modulated with the frequency of the applied voltage. This phase modulation generates sidebands that become separated from the optical carrier frequency by multiples of the modulation frequency and form a comb (Fig. 1). One can observe this behaviour in a standard EOM[19], but the magnitude of the sidebands usually decays quickly with distance from the carrier. The length of the comb is determined by the modulation index, which scales with the amplitude of the applied electric field[20]. To boost the electric field and thus the efficiency of the process and to generate a wide-spanning comb, we embed a high-quality optical whispering gallery mode (WGM) resonator into a high-quality microwave resonator.

Another equivalent way to view the process is sum- and difference-frequency generation: the energy of the microwave photons is either added to or subtracted from the carrier photon, yielding new frequencies. These sidebands themselves interact with microwave photons and give rise to new frequencies, again by the same process. For efficient comb generation, the sidebands have to match an optical resonance. As a consequence, the microwave resonator needs to be designed such that

[1]Max Planck Institute for the Science of Light, Erlangen, Germany. [2]Institute for Optics, Information and Photonics, University Erlangen-Nuernberg, Erlangen, Germany. [3]School in Advanced Optical Technologies (SAOT), Erlangen, Germany. [4]Institute of Science and Technology Austria, Klosterneuburg, Austria. [5]The Dodd-Walls Centre for Photonic and Quantum Technologies, Dunedin, New Zealand. [6]Department of Physics, University of Otago, Dunedin, New Zealand. [7]Institute of Applied Physics, Russian Academy of Sciences, Nizhny Novgorod, Russia.
*e-mail: harald.schwefel@otago.ac.nz

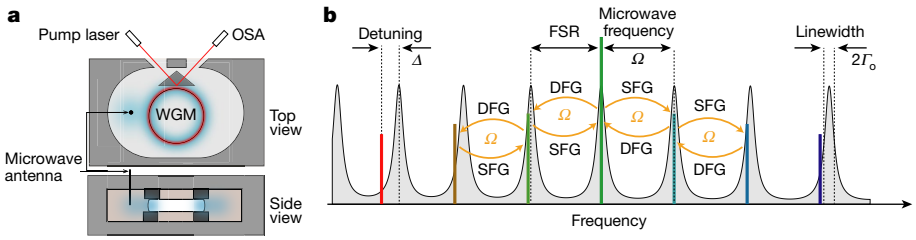

Fig. 1 | Principles of generating WGM-based $\chi^{(2)}$-frequency combs. **a**, Diagram showing the setup for the creation of electro-optic second-order ($\chi^{(2)}$)-frequency combs. A high-quality WGM optical resonator—a convex-shaped disk that guides light via total internal reflection along its inner surface, and machined from single-crystalline lithium niobate—is embedded in a microwave cavity made from copper. Light is coupled with a prism evanescently by frustrated total internal refection into the WGM. The microwave resonator is designed so that the resonantly enhanced microwave field has maximum overlap with the optical WGM. Microwave radiation is fed into the cavity through a microwave coupling pin. **b**, Illustration showing how the microwave field phase-modulates the light via the Pockels effect and a frequency comb is generated. The optical modes are separated by a nearly constant free spectral range (FSR), which approximately matches the frequency of the microwave tone, Ω, allowing for sum- and difference-frequency generation (SFG, DFG) of sidebands, indicated as the coloured vertical lines. Given the fixed microwave frequency, the comb lines are generated strictly equidistantly. This leads to a detuning of the comb lines from the optical modes (indicated by the Lorentzian-shaped black curve with grey shading), which are subject to dispersion, and eventually breaks the comb, as illustrated in Fig. 2.

its resonance frequency coincides with the free spectral range (FSR) of the optical resonator. Mathematically, the system is described by an infinite but simple set of linear equations, each representing an optical mode participating in the nonlinear process. It can be solved analytically under the condition of a constant FSR (see Supplementary Information and ref. [21]), and for the time-dependent optical field amplitudes in reflection of the resonator, we find:

$$\frac{A_{\mathrm{out}}(t)}{A_{\mathrm{in}}(t)} = \frac{(2\gamma/\Gamma) - 1 - i(\Delta + 2\sqrt{G}\cos(\Omega t))}{1 + i(\Delta + 2\sqrt{G}\cos(\Omega t))} \quad (1)$$

Here A_{in} and A_{out} stand for the input and output electric field; $\Gamma = \gamma + \gamma'$ is the half-linewidth of the optical modes, where γ and γ' are the optical coupling rate and intrinsic field loss rate, respectively; the detuning of the optical carrier frequency, $\omega_0 - \omega$, from its resonance frequency, ω_0, is normalized to half of the optical linewidth, $\Delta = (\omega_0 - \omega)/\Gamma$; Ω is the microwave frequency, which we assume to be on-resonance; t is time; and i is the imaginary number $\sqrt{-1}$. The figure of merit is $G = n_\Omega g^2/|\Gamma|^2$, where n_Ω is the number of microwave photons in the resonator and g is the single-photon coupling rate, which is a function of the electro-optic coefficient and the overlap between the optical and the microwave modes. G is often referred to as electro-optic cooperativity[22] and represents the ratio between the nonlinear photon-conversion rate and the photon-decay rate, and is hence a measure of the strength of the nonlinear interaction. It is interesting to compare the modulation of a resonant EOM with a nonresonant EOM, which is simply described by $A_{\mathrm{out}}(t) = e^{i\xi\cos(\Omega t)}A_{\mathrm{in}}(t)$, where the modulation index, ξ, is approximately $4\sqrt{G}$. The nonresonant EOM does not contain any amplitude modulation; the resonant EOM, on the other hand, does. Only when the resonant EOM is strongly overcoupled (when γ is much greater than γ') and for very small nonlinearities ($G \approx 0$) the two systems are comparable. At critical coupling ($\gamma = \gamma'$) and increasing G, the resonant EOM starts generating pulses with a repetition rate of $1/2\tau$, where τ is the roundtrip time of the optical cavity. We show in Supplementary Information that the pulse width, $\Delta\tau$, can be approximated as $\Delta\tau \approx \tau/(2\pi\sqrt{G})$.

The power of the comb lines, $P(\omega \pm k\Omega)$, can also be analytically described as:

$$\frac{P(\omega \pm k\Omega)}{P_{\mathrm{in}}} = \frac{4\gamma^2}{\Gamma^2}\left|\frac{e^{-\beta(G)}}{\sqrt{G} + \sqrt{G}\,e^{-2\beta(G)}}\right|^2 e^{-2|k|\beta(G)} \text{ for } k \neq 0 \quad (2)$$

where k represents the order of the sideband; P_{in} is the input optical power; e is Euler's number; and $2\beta(G)$ is the decay constant and can be approximated to be $\beta(G) \approx 1/\sqrt{4G}$ in the limit of strong nonlinear interaction when $4G$ is much greater than 1 (see Supplementary Information). The resonant comb scales strictly exponentially, which is another difference to the nonresonant comb, where the comb line

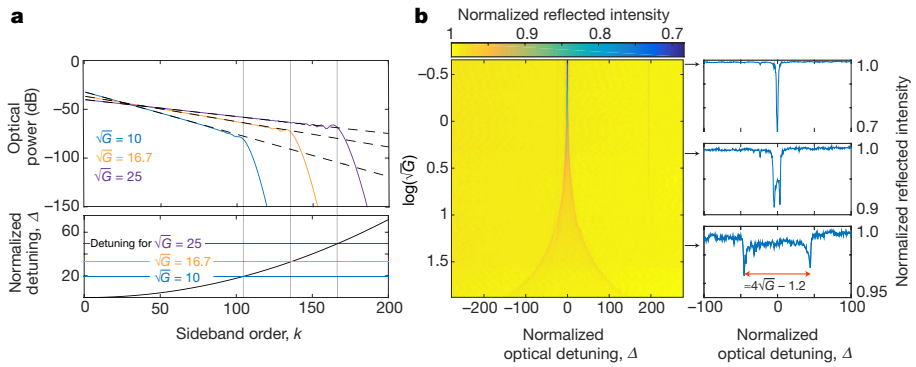

Fig. 2 | Theoretical scaling of sideband power and dispersion-induced breakdown of the comb. **a**, Top, power of the sidebands as a function of sideband order for different modulation strengths (G). The dashed lines represent the analytical solution given by equation (2), and the coloured curves are numerical solutions that include the optical dispersion of lithium niobate (see Supplementary Information). Bottom, the dispersion leads to a detuning of the equidistantly generated comb lines from the optical resonance frequencies. When a certain detuning, Δ, of the comb lines from the optical resonance frequency is reached, the comb breaks down drastically. **b**, The dependence of the breakdown on the cooperativity, G, can be understood by the nonlinear induced broadening of the modes shown here: the yellow contour plot on the left combines 101 spectra of the resonances exemplified on the right into a plot of the optical coupling depth (indicated by the colour bar) versus optical detuning, Δ, and a function of the microwave power, $\log(\sqrt{G})$. The measured mode splitting is a function of G, which is proportional to the square root of the microwave power sent to the system.

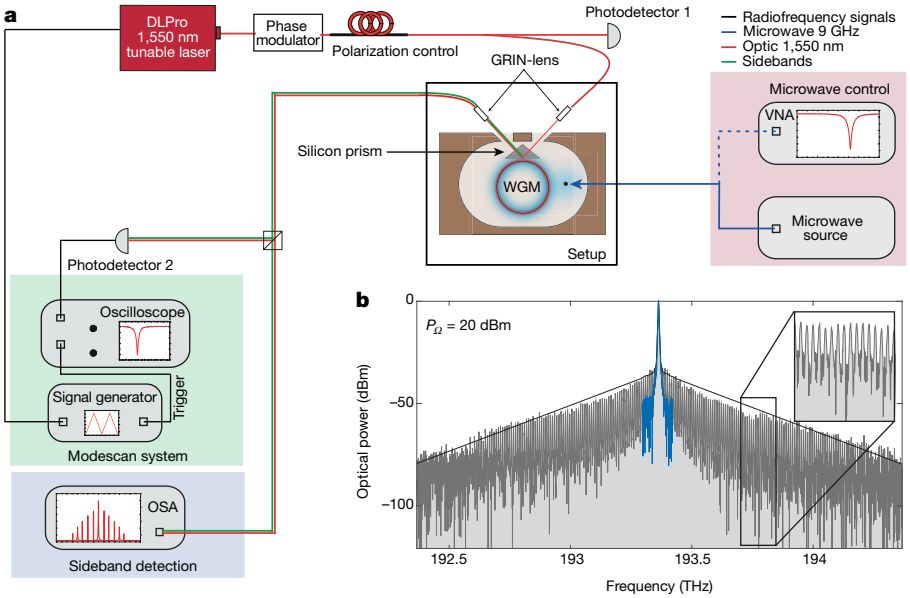

Fig. 3 | Experimental realization. a, Measurement network. From top left, a tunable monochromatic coherent laser source (from DLPro) in the C-band of the telecommunication domain ($\lambda = 1{,}549$ nm) goes through a phase modulator, used for measuring the optical FSR and the linewidth of the modes. The polarization controller sets the gradient-index (GRIN)-lens output beam to transverse electric (TE) polarization; 1% of the light is used for power calibration (photodetector 1), while 99% is directed towards the WGM resonator. The silicon prism couples 30% of the light into the WGM and the remaining 70% are directly reflected and outcoupled into photodetector 2 to characterize the optical spectrum of the resonator. The comb lines, also outcoupled through the silicon prism, are detected on an OSA. The microwave tone (right) was transmitted through a cable to the pin coupler inside the cavity. This transmission line was also used to characterize the microwave mode with a vector network analyser (VNA). See Methods for more details. **b**, Spectrum of the frequency comb generated with 20 dBm microwave power (P_Ω) at 8.9 GHz, spanning more than 180 comb lines and resulting in a width of about 1.6 THz. In blue is the spectrum of the pump laser without the added microwave tone.

power is described by Bessel functions[23]. In Fig. 2a we plot equation (2) for different modulation strengths as dashed lines on a logarithmic scale. It is apparent that the slope of the exponential decay decreases with increasing G, leading to the generation of longer combs.

To derive the previous analytical solution for the system, we neglected optical dispersion, which is intrinsic owing to geometric and material dispersion. As a consequence, the optical modes are not exactly equally spaced and the generated comb lines become increasingly detuned from the optical resonance frequencies with distance from the carrier mode (Fig. 1b). This eventually breaks the comb generation, as illustrated in Fig. 2a: the solid curves show the sideband power as function of the sideband order obtained from numerically solving the rate equations while including optical dispersion of lithium niobate (see Supplementary Information for details). Close to the pump frequency the power decreases exponentially (as expected from equation (2)) until a certain G-dependent sideband order, at which point it drops drastically. This can be intuitively understood from Fig. 2b: with increasing microwave power, the optical modes broaden and show a mode splitting of $(4\sqrt{G} - 1.2)\Gamma$. The dispersion-induced detuning of the optical eigenfrequencies from the generated sidebands does not affect the comb generation greatly at the half-width of a cold cavity mode (Γ), but rather much later, at $2\sqrt{G} - 0.6$. Figure 2b shows that this intuitive picture is accurate. As soon as the detuning (Fig. 1b) equals the nonlinear broadening, the comb starts to break down. Nevertheless, with reasonable parameters we expect a few hundred lines, as shown in Fig. 2a.

To demonstrate our highly efficient scheme experimentally, we embedded a high-quality WGM optical resonator machined from single-crystalline lithium niobate into a microwave cavity made from copper. The optical resonator is a convex-shaped disk that guides light via total internal reflection along its inner surface, interfering with itself after each roundtrip[24]. Given that lithium niobate is quite transparent, the light can do many roundtrips before being absorbed, boosting the optical intensity by orders of magnitude and facilitating efficient nonlinear interactions[25–28]. The microwave resonator is a three-dimensional copper cavity enclosing the optical resonator, designed such that the resonantly enhanced microwave field has maximum overlap with the optical WGM. The cavity contains two protruded copper rings facing each other, which clamp the optical resonator when the cavity is closed. This ensures that the microwave field is focused on the rim of the optical resonator where the optical modes are located, maximizing the overlap between the two vastly different frequencies. Two holes are used to couple optical light into and out of the cavity. Apart from that, the copper cavity is closed to prevent the microwave mode from radiating into the far field, which would decrease its quality factor, Q. Inside the cavity, we use a silicon prism placed close to the optical resonator to couple the light evanescently into the lithium niobate disk. The WGM resonator has a radius of 2.45 mm and a thickness of 0.4 mm, resulting in a free spectral range of about 8.9 GHz at the used pump frequency $\omega_0 = 2\pi \times 193.3$ THz.

On the basis of numerical simulations of the microwave mode (see Methods), we designed the copper cavity such that the microwave resonance approximately matches the optical free spectral range and added a fine-tuning mechanism to compensate for small fabrication tolerances. Our system has a single-photon coupling rate of $g = 2\pi \times 7.4$ Hz; the optical and microwave quality factors are $Q_o = 1.4 \times 10^8$ and $Q_\Omega = 241.4$, respectively. The optical resonator is critically coupled, resulting in $\gamma = \gamma' = 2\pi \times 0.35$ MHz, while the microwave resonator is undercoupled, with $\gamma_\Omega = 2\pi \times 3.6$ MHz and $\gamma_{i\Omega} = 2\pi \times 16.2$ MHz. For convenient comparison with canonical electro-optic phase modulators, one can estimate the π-voltage from these parameters to be $V_\pi = 260$ mV (see Supplementary Information). Typical nonresonant modulators have values of a few volts, showing the high efficiency of our system. This is traded, of course, by having a bandwidth of only a few megahertz, compared with the bandwidth of several gigahertz for nonresonant systems.

To observe the comb, we coupled 320 μW of optical power into a fundamental WGM and modulated it with 20 dBm of microwave power

(with a transmission loss of 9.4 dB), corresponding to $\sqrt{G} \approx 25$. The light emitted from the cavity was coupled to an optical fibre and measured with an optical spectrum analyser (OSA). Figure 3b shows that the generated comb has a span of about 11 nm, corresponding to 1.6 THz, and 90 visible comb lines in each direction. The comb is, as expected, symmetrical and decays approximately exponentially. According to our theory, we expect a dispersion-induced breakdown of the comb at a span of 320 lines, which we cannot observe owing to the noise floor of the OSA.

In summary, we have demonstrated that multiresonant electro-optic modulation can lead to the formation of a broadband frequency comb at very low electrical power consumption. We have presented a complete analytical solution for a dispersionless system that describes the comb formation thoroughly, including the phase and amplitude of the generated comb lines and their temporal behaviour at steady state. Our numerical simulations show that, even when taking into account optical dispersion, the comb can span hundreds of lines owing to nonlinear line broadening of the optical modes before breaking down. Because two stabilized sources are used to generate this electro-optic comb via a second-order nonlinear effect, the resulting comb lines have a fixed and predetermined phase relation to each other. The combination of compact, high-quality resonant enhancement with careful microwave-field engineering and a fast way to calculate nonlinear pulse propagation in real time could be key to power-efficient optical interconnects, and could extend the range of long-distance interconnects owing to the inherent phase relation of all the comb lines.

Online content

Any methods, additional references, Nature Research reporting summaries, source data, statements of data availability and associated accession codes are available at https://doi.org/10.1038/s41586-019-1110-x.

Received: 7 August 2018; Accepted: 20 February 2019;
Published online 17 April 2019.

1. Kahn, J. M. & Miller, D. A. B. Communications expands its space. *Nat. Photon.* **11**, 5–8 (2017).
2. Pfeifle, J. et al. Coherent terabit communications with microresonator Kerr frequency combs. *Nat. Photon.* **8**, 375–380 (2014).
3. Ataie, V. et al. Ultrahigh count coherent WDM channels transmission using optical parametric comb-based frequency synthesizer. *J. Lightwave Technol.* **33**, 694–699 (2015).
4. Marin-Palomo, P. et al. Microresonator-based solitons for massively parallel coherent optical communications. *Nature* **546**, 274–279 (2017).
5. Temprana, E. et al. Overcoming Kerr-induced capacity limit in optical fiber transmission. *Science* **348**, 1445–1448 (2015).
6. Mitchell, G. & Hodara, H. Review of the 2017 optical fiber communications (OFC) conference. *Fiber Integr. Opt.* **36**, 101–103 (2017).
7. Imran, M., Anandarajah, P. M., Kaszubowska-Anandarajah, A., Sambo, N. & Poti, L. A survey of optical carrier generation techniques for terabit capacity elastic optical networks. *IEEE Comm. Surv. Tutor.* **20**, 211–263 (2018).
8. Luo, L. W. et al. WDM-compatible mode-division multiplexing on a silicon chip. *Nat. Commun.* **5**, 3069 (2014).
9. Holzwarth, R. et al. Optical frequency synthesizer for precision spectroscopy. *Phys. Rev. Lett.* **85**, 2264–2267 (2000).
10. Liang, W. et al. High spectral purity Kerr frequency comb radio frequency photonic oscillator. *Nat. Commun.* **6**, 7957 (2015).
11. Suh, M.-G. & Vahala, K. Gigahertz-repetition-rate soliton microcombs. *Optica* **5**, 65–66 (2018).
12. Kippenberg, T. J., Holzwarth, R. & Diddams, S. A. Microresonator-based optical frequency combs. *Science* **332**, 555–559 (2011).
13. Herr, S. J. et al. Frequency comb up- and down-conversion in synchronously driven $\chi^{(2)}$ optical microresonators. *Opt. Lett.* **43**, 5745–5748 (2018).
14. Stefszky, M., Ulvila, V., Abdallah, Z., Silberhorn, C. & Vainio, M. Towards optical-frequency-comb generation in continuous-wave-pumped titanium-indiffused lithium-niobate waveguide resonators. *Phys. Rev. A* **98**, 053850 (2018).
15. Leo, F. et al. Frequency-comb formation in doubly resonant second-harmonic generation. *Phys. Rev. A* **93**, 043831 (2016).
16. Torres-Company, V. & Weiner, A. M. Optical frequency comb technology for ultra-broadband radio-frequency photonics. *Laser Photonics Rev.* **8**, 368–393 (2014).
17. Kovacich, R. P., Sterr, U. & Telle, H. R. Short-pulse properties of optical frequency comb generators. *Appl. Opt.* **39**, 4372–4376 (2000).
18. Beha, K. et al. Electronic synthesis of light. *Optica* **4**, 406–411 (2017).
19. Kourogi, M., Nakagawa, K. & Ohtsu, M. Wide-span optical frequency comb generator for accurate optical frequency difference measurement. *IEEE J. Quantum Electron.* **29**, 2693–2701 (1993).
20. Pozar, D. M. *Microwave Engineering* 4th edn (Wiley, Hoboken, 2011).
21. Ilchenko, V. S., Savchenkov, A. A., Matsko, A. B. & Maleki, L. Whispering-gallery-mode electro-optic modulator and photonic microwave receiver. *J. Opt. Soc. Am. B* **20**, 333–342 (2003).
22. Tsang, M. Cavity quantum electro-optics. *Phys. Rev. A* **81**, 063837 (2010).
23. Hobbs, P. *Building Electro-Optical Systems: Making It all Work* (Wiley, Hoboken, 2011).
24. Strekalov, D. V., Marquardt, C., Matsko, A. B., Schwefel, H. G. L. & Leuchs, G. Nonlinear and quantum optics with whispering gallery resonators. *J. Opt.* **18**, 123002 (2016).
25. Strekalov, D. V. et al. Microwave whispering-gallery resonator for efficient optical up-conversion. *Phys. Rev. A* **80**, 033810–033815 (2009).
26. Rueda, A. et al. Efficient microwave to optical photon conversion: an electro-optical realization. *Optica* **3**, 597–604 (2016).
27. Botello, G. S. et al. Sensitivity limits of millimeter-wave photonic radiometers based on efficient electro-optic upconverters. *Optica* **5**, 1210–1219 (2018).
28. Breunig, I. Three-wave mixing in whispering gallery resonators. *Laser Photonics Rev.* **10**, 569–587 (2016).

Acknowledgements This work was supported by the Marsden Fund Council and Julius von Haast Fellowship from government funding, managed by Royal Society Te Apārangi of New Zealand, and the Max Planck Institute for the Science of Light, Erlangen, Germany.

Reviewer information *Nature* thanks Pauline Kuo and the other anonymous reviewer(s) for their contribution to the peer review of this work.

Author contributions A.R. and F.S. performed all of the experiments and developed the theory. A.R. performed the theoretical and numerical modelling. H.G.L.S. proposed the experiment and supervised the project. A.R., F.S., M.K., G.L. and H.G.L.S. wrote the manuscript. All authors contributed to discussing and interpreting the results.

Competing interests The authors declare no competing interests.

Additional information
Extended data is available for this paper at https://doi.org/10.1038/s41586-019-1110-x.
Supplementary information is available for this paper at https://doi.org/10.1038/s41586-019-1110-x.
Reprints and permissions information is available at http://www.nature.com/reprints.
Correspondence and requests for materials should be addressed to H.G.L.S.
Publisher's note: Springer Nature remains neutral with regard to jurisdictional claims in published maps and institutional affiliations.

METHODS

Theory. Theoretically we can describe the system of a strong microwave field coupled nonlinearly to two optical fields by their total energy, its Hamiltonian. Assuming no depletion of the microwave field (owing to the presence of both sum- and difference-frequency generation), the nonlinear interaction Hamiltonian is given by (see Supplementary Information):

$$\hat{H}_{\mathrm{int}} = \hbar\ |\alpha|\ g\,(\hat{a}_1\hat{a}_2^{\dagger} + \hat{a}_1^{\dagger}\hat{a}_2)$$

This is also known as the beam-splitter Hamiltonian. Here $\hbar$ is Planck's constant; $|\alpha|^2$ is the number of microwave photons in the cavity; and $\hat{a}_1$ and $\hat{a}_2^{\dagger}$ are the standard quantum optical annihilation and creation operators of the two optical fields[29], and can represent sum- as well as difference-frequency generation. This linearization of the Hamiltonian is also known as a zero-photon process, characterized by photons scattering from one mode into another without changing the total number of photons[30]. The single-photon coupling rate, g, is defined as:

$$g = 2\varepsilon_0\chi^{(2)}\sqrt{\frac{\hbar\omega_0\omega_s\omega_\Omega}{8\varepsilon_0\varepsilon_s\varepsilon_\Omega V_0 V_s V_\Omega}}\int \mathrm{d}V\psi_\Omega\psi_s^{\dagger}\psi_0$$

where $\chi^{(2)}$ is the second-order nonlinear susceptibility; ε_0 is the vacuum permittivity; and ω_i, ε_i, V_i and ψ_i are the frequency, relative permittivity, normalization volume and the field distribution of the optical pump (0), sideband (s) and microwave tone (Ω), indicated here by the index i. The integral over the fields is only nonzero if the so called phase-matching relation between the individual fields is fulfilled, which leads to the relation $m_s = m_0 + m_\Omega$, where m is the angular momentum number for the sideband, pump and microwave field, respectively (see Supplementary Information). In a system with multiple modes ω_k, equidistantly separated from the optical pump field frequency ω_0, a strong microwave field leads to a cascade of the sum- and difference-frequency generation. Assuming the same nonlinear coupling constant, g, between the optical and microwave fields, and noting that, because of phase matching, only spectrally adjacent modes can interact, the Hamiltonian can be written as:

$$\hat{H}_{\mathrm{int}} = \hbar\ |\alpha|\ g\sum_{k=-N}^{N-1}(\hat{a}_k\hat{a}_{k+1}^{\dagger} + \hat{a}_k^{\dagger}\hat{a}_{k+1})$$

where $2N+1$ is the number of optical modes involved in the system, and $\hat{a}_k$ denotes the operator of the k participating optical modes. To describe their dynamics under the presence of a coherent microwave drive, we find the equations of motion using the Heisenberg picture to be:

$$\dot{\hat{a}}_k = \frac{i}{\hbar}[\hat{H}_{\mathrm{int}}, \hat{a}_k] = -\,in_\Omega g(\hat{a}_{k-1} + \hat{a}_{k+1})$$

where n_Ω is the number of microwave photons in the system. We introduce coupling and loss channels and solve these equations for the steady state in the rotating wave approximation and classical limit. Taking into account that we need to outcouple the fields from the resonator, we obtain equations (1), (2).

Numerical cavity design. The microwave cavity was designed with the help of numerical simulations using COMSOL Multiphysics version 5.4 (www.comsol.com). The goal was to maximize the overlap between microwave and optical fields while choosing the system geometry such that the optical FSR coincides with the $m_\Omega = 1$ microwave mode with a frequency of around 10 GHz. In compliance with these boundaries, we optimized the microwave coupling and allowed for an optical coupling port to the WGM resonator. We found a solution for efficient type-0 phase matching (TE + TE → TE) for which the electro-optic coefficient of lithium niobate is largest. We note that this hybrid system is very similar to our previous work on coherent microwave upconversion, showing the versatility of this approach[26].

Experiment. We fabricate a lithium niobate WGM resonator ($n_o = 2.21$ and $n_{eo} = 2.14$ for ordinary and extraordinary polarization[31]) with major radius $R = 2.45$ mm, minor radius $r = 1.5$ mm, and height $h = 0.4$ mm, mounted within the copper cavity shown in Extended Data Fig. 1a, b (see also Supplementary Information). As the optical pump we use a narrow-band tunable laser (Toptica DLPro; $\lambda \approx 1{,}550$ nm; linewidth 100 kHz) which goes through a polarization controller. The pump is split 99/1, with the weak port being sent to the detector to keep track of the pump power (Fig. 3). The other arm goes to the graded index lens for WGM-prism coupling to a transverse electric mode. We use a silicon prism ($n_{Si} = 3.47$) mounted within the copper cavity. Two holes in the copper cavity allow the optical pump light to enter the cavity and the reflected light and the emitted sideband from the WGM resonator to leave. The signal and reflected pump are coupled to a fibre and sent to an InGaAs photodetector (PDA10CS; Thorlabs), and its output signal to the oscilloscope. We can use a signal generator to sweep the laser frequency, to scan over the optical modes of the cavity, and to measure the optical FSR and optical loaded Q using sideband spectroscopy[32]. The microwave signal generated by a microwave source (SMR20; Rohde and Schwarz) is coupled via a coaxial pin coupler introduced close to the WGM resonator inside the cavity. The same transmission line is used for reflection measurements with a vector network analyser (ENA E5072A; Keysight) to obtain the central frequency, coupling and loss rate of the microwave mode. A metallic tuning screw is used to perturb the microwave field for fine adjustment of its resonance frequency (Fig. 2a). The whole setup is thermally stabilized at 30 °C to the millikelvin level with a proportional-integral-derivative (PID) controller (TC200; Thorlabs) in combination with a temperature sensor (AD590; Analog Devices) and a thermoelectric element attached on the outer side of the closed copper cavity. Once the laser is set to the mode, we send the microwave tone and create the sidebands (Fig. 3b). These signals are outcoupled through the prism and coupled to the fibres. The sidebands together with the reflected optical pump are measured with an OSA (AQ6370C; Yokogawa).

29. Mandel, L. & Wolf, E. *Optical Coherence and Quantum Optics* 1st edn (Cambridge Univ. Press, Cambridge, 1995).
30. Law, C. K. Effective hamiltonian for the radiation in a cavity with a moving mirror and a time-varying dielectric medium. *Phys. Rev. A* **49**, 433–437 (1994).
31. Zelmon, D. E., Small, D. L. & Jundt, D. Infrared corrected Sellmeier coefficients for congruently grown lithium niobate and 5 mol. % magnesium oxide-doped lithium niobate. *J. Opt. Soc. Am. B* **14**, 3319–3322 (1997).
32. Li, J., Lee, H., Yang, K. Y. & Vahala, K. J. Sideband spectroscopy and dispersion measurement in microcavities. *Opt. Express* **20**, 26337–26344 (2012).

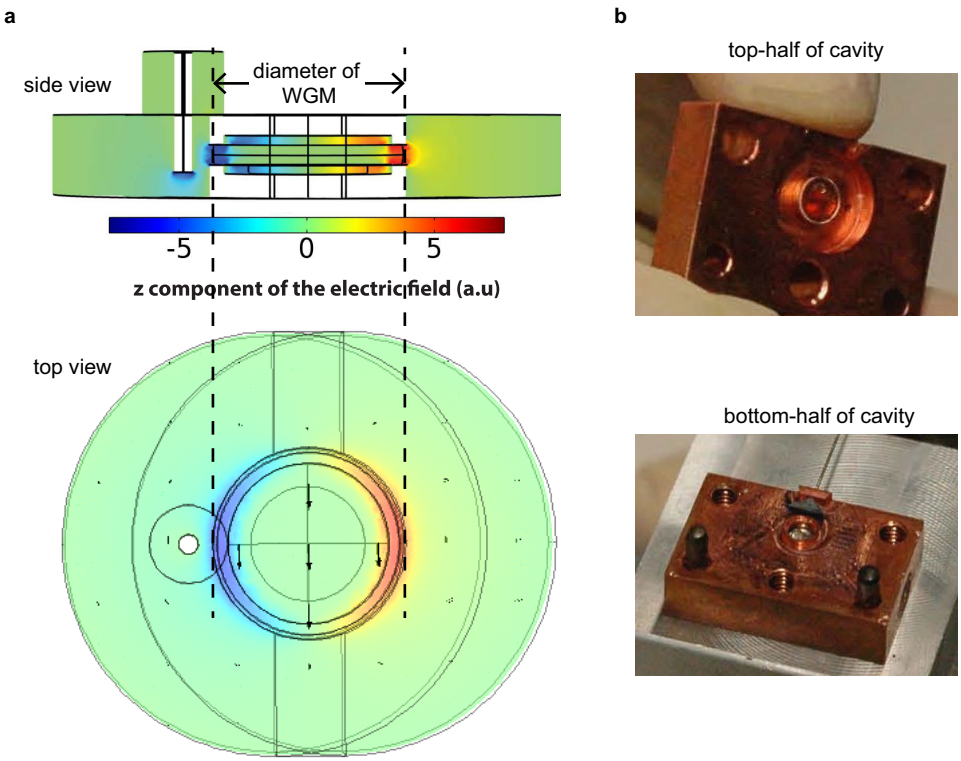

Extended Data Fig. 1 | Experimental realization. a, COMSOL simulation of the 3D copper microwave cavity. The colour bar indicates the microwave electrical field distribution inside the microcavity. In the side and top view, the localization close to the rim of the WGM is apparent. Dashed lines indicate the diameter of the WGM. The microwave field is coupled through a pin coupler to the WGM. **b**, Top and bottom halves of the copper cavity. The lithium niobate WGM resonator is mounted in the top half and the silicon prism in the bottom half.

Bidirectional Electro-Optic Wavelength Conversion in the Quantum Ground State

William Hease,[1,†] Alfredo Rueda,[1,2,†] Rishabh Sahu,[1] Matthias Wulf,[1] Georg Arnold,[1] Harald G.L. Schwefel,[2,3] and Johannes M. Fink[1,*]

[1] *Institute of Science and Technology Austria, Klosterneuburg, Austria*
[2] *Department of Physics, University of Otago, Dunedin, New Zealand*
[3] *The Dodd-Walls Centre for Photonic and Quantum Technologies, Dunedin, New Zealand*

(Received 30 June 2020; accepted 26 October 2020; published 23 November 2020)

Microwave photonics lends the advantages of fiber optics to electronic sensing and communication systems. In contrast to nonlinear optics, electro-optic devices so far require classical modulation fields whose variance is dominated by electronic or thermal noise rather than quantum fluctuations. Here we demonstrate bidirectional single-sideband conversion of X band microwave to C band telecom light with a microwave mode occupancy as low as 0.025 ± 0.005 and an added output noise of less than or equal to 0.074 photons. This is facilitated by radiative cooling and a triply resonant ultra-low-loss transducer operating at millikelvin temperatures. The high bandwidth of 10.7 MHz and total (internal) photon conversion efficiency of 0.03% (0.67%) combined with the extremely slow heating rate of 1.1 added output noise photons per second for the highest available pump power of 1.48 mW puts near-unity efficiency pulsed quantum transduction within reach. Together with the non-Gaussian resources of superconducting qubits this might provide the practical foundation to extend the range and scope of current quantum networks in analogy to electrical repeaters in classical fiber optic communication.

DOI: 10.1103/PRXQuantum.1.020315

I. INTRODUCTION

The last three decades have witnessed the emergence of a great diversity of controllable quantum systems, and superconducting Josephson circuits are one of the most promising candidates for the realization of scalable quantum processors [1]. However, quantum states encoded in microwave frequency excitations are very sensitive to thermal noise and electromagnetic interference. Short distance quantum networks could be realized with cryocooled transmission lines [2], but longer distances and high density networks require coherent up-conversion to shorter wavelength information carriers, ideally compatible with existing near infrared (1550 nm) fiber optic technology. So far, no solution exists to deterministically interconnect remote quantum microwave systems, such as superconducting qubits [3] and hybrid devices like quantum dots or spins in solids [4–6] via a room-temperature link with sufficient fidelity to build large-scale quantum networks [7,8]. Solving this challenge might not only facilitate a new generation of more power efficient classical microwave photonics [9], but eventually also enable quantum secure communication, modular quantum computing clusters, and powerful quantum sensing networks.

An ideal quantum signal converter [10] follows unitary dynamics, i.e., it is bidirectional, and exhibits a total conversion efficiency close to unity $\eta_{\mathrm{tot}} \approx 1$ for quantum level signals with a minimum amount of added noise referenced to the input port $N_{\mathrm{in}} = N_{\mathrm{out}}/\eta_{\mathrm{tot}} \ll 1$ over a large instantaneous bandwidth that allows for fast transduction compared to typical qubit coherence times.

Many different platforms are already being explored for microwave-to-optical photon conversion [11,12]. Electro-optomechanical systems have shown efficiencies up to $\eta_{\mathrm{tot}} = 47\%$ [13,14], but typically suffer from a limited bandwidth in the kilohertz range, and added noise $N_{\mathrm{in}} > 30$ due to residual thermal population in the low-frequency mechanical mediator that is efficiently coupled to the microwave mode. Electro-optic [15–19] or piezo-optomechanical [20–22] conversion can be faster, but the conversion noise properties have not been quantified. Facilitated by efficient photon counting and low duty cycle operation, unidirectional transduction of quantum level signals [23,24] has also recently been

*jfink@ist.ac.at
†These authors contributed equally to this work.

shown. Nevertheless, ground-state conversion has not been demonstrated in a bidirectional interface so far.

In this work we present such a device operating continuously with a microwave mode occupancy $N_e \leq 1$ for a pump laser power of up to $P_p = 23.5\ \mu$W. Compared to the current benchmark for a general purpose quantum interface [13], we show close to ground-state operation, resulting in extremely low conversion noise of $N_{\text{out}} \leq 0.074$ photons at the output and achieve that with a 10^2–10^3 times higher bandwidth. This is at the expense of a lower efficiency, resulting in a significantly larger equivalent input noise N_{in}. Nevertheless, the measurement of ground-state initialization is an important stepping stone in order to convert nonclassical states with high fidelity in the future.

Compared to previous transducers in this limit [23,24] we show continuous-wave bidirectional operation resulting in orders of magnitude higher integrated bandwidth (100% duty cycle). While Mirhosseini *et al.* [24] upconverted a localized phononic qubit excitation in a fully integrated on-chip platform, we demonstrate conversion of propagating classical fields entering via a fiber or coaxial port from either side. Most importantly, our modular approach [25] is expected to be fully compatible for future operation with high coherence superconducting qubits without affecting the qubit state—a crucial requirement to entangle qubits and optical photons. The presented device therefore represents a versatile microwave photonic transceiver that can transmit and receive classical and quantum information in either direction.

The physics of the presented device is based on a triply resonant electro-optic interaction as proposed in Refs. [26–30]. The specific experimental implementation relies on an ultra-high quality factor, millimeter-sized, crystalline lithium niobate whispering gallery mode resonator that is resonantly coupled to a superconducting three-dimensional (3D) microwave cavity similar to earlier bulk [15,31,32] and on-chip [16–19] electro-optic experiments without conversion noise characterization. The large size and heat capacity allows for extremely slow thermalization times, which are about 10^7 times slower compared to state-of-the-art microscopic microwave devices pulsed with about 10^3 times lower power [24]. This is expected to result in a higher duty cycle at the same temperature and efficiency, which might ultimately lead to a significantly higher channel capacity in the context of pulsed conversion of quantum states.

II. THEORY

Electro-optic converters make use of the nonlinear properties of noncentrosymmetric crystals to couple optical and microwave degrees of freedom. Our resonant transducer has two high-quality-factor optical modes whose frequency difference matches the resonance frequency of a microwave mode. The system's interaction Hamiltonian is given as [27]

$$\hat{H}_{\text{int}} = \hbar g(\hat{a}_e \hat{a}_p \hat{a}_o^\dagger + \hat{a}_e^\dagger \hat{a}_p^\dagger \hat{a}_o), \tag{1}$$

where $\hat{a}_e$, $\hat{a}_p$, and $\hat{a}_o$ denote the annihilation operators for the microwave, optical pump, and optical signal mode, respectively. This Hamiltonian describes two reciprocal three-wave mixing processes that involve creation and annihilation of photons while respecting energy conservation. The nonlinear vacuum coupling rate g for this interaction depends on the material's effective electro-optic coefficient r and the spatial overlap of the three modes [15]

$$g = r\sqrt{\frac{\varepsilon_p \varepsilon_o}{\varepsilon_e}}\sqrt{\frac{\hbar\omega_e\omega_p\omega_o}{8\varepsilon_0 V_e V_p V_o}}\int dV \psi_e \psi_p \psi_o^\star \tag{2}$$

with mode frequency ω_k, relative permittivity ε_k and permeability $\mu_k = 1$, effective mode volume V_k, and normalized spatial field distribution ψ_k defined such that the single-photon electric field for mode $k \in \{e, p, o\}$ can be written as $E_k(\vec{r}) = \sqrt{\hbar\omega_k/(2\varepsilon_0\varepsilon_k V_k)}\psi_k(\vec{r})$. All three modes are whispering gallery modes (WGMs) [33] whose spatial field distribution can be separated into cross-sectional and azimuthal parts $\psi_k(r, z, \phi) = \Psi_k(r, z)e^{-im_k\phi}$. The integral in Eq. (2) is nonzero only if the azimuthal numbers of the participating modes fulfil $m_o = m_p + m_e$, which is also known as phase matching or angular momentum conservation.

In our conversion scheme we drive the mode $\hat{a}_p$ with a bright coherent tone $\hat{a}_p \to \alpha_p$, which simplifies Eq. (1) to

$$\hat{H}_{\text{int}} = \hbar\alpha_p g(\hat{a}_e \hat{a}_o^\dagger + \hat{a}_e^\dagger \hat{a}_o). \tag{3}$$

This is known as the beam splitter Hamiltonian and it corresponds to a linear coupling between the optical mode $\hat{a}_o$ and microwave mode $\hat{a}_e$. From the enhanced coupling rate $\alpha_p g$, we define the multiphoton cooperativity as $C = 4|\alpha_p|^2 g^2/(\kappa_o\kappa_e)$, where κ_o and κ_e are the total loss rates of the optical and microwave modes, respectively. The multiphoton cooperativity is the figure of merit in most of the resonant electro-optic devices, both for frequency conversion and entanglement generation [15,16,28,34].

III. DEVICE

The electro-optic transducer consists of a z-cut lithium niobate ($LiNbO_3$) whispering gallery mode (WGM) resonator, with major radius $R = 2.5$ mm, sidewall surface radius $\rho \approx 0.7$ mm, and thickness $d = 0.15$ mm. It is fabricated using diamond polishing pastes of different grain size [35], and is coupled to a superconducting aluminum cavity as shown in Fig. 1(a). The top and bottom rings of the cavity are designed to confine the microwave mode at the rim of the WGM resonator and maximize the spatial mode

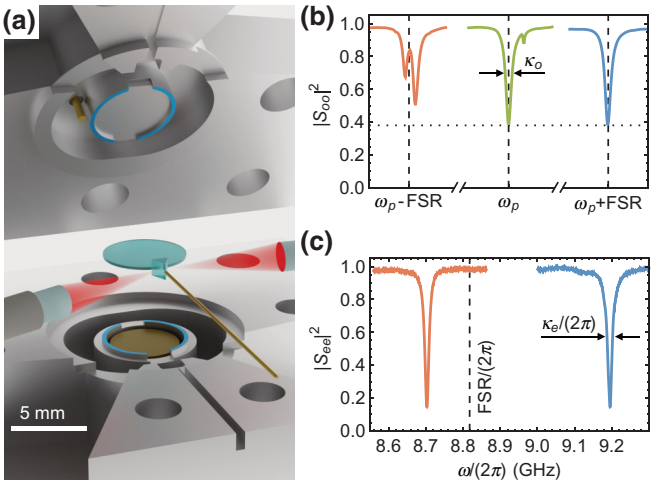

FIG. 1. (a) Exploded-view rendering of the electro-optic converter. The WGM resonator (light blue disc) is clamped between two aluminum rings (blue shaded areas) belonging to the top and bottom parts of the aluminum microwave cavity, respectively. Two gradient index (GRIN) lenses are used to focus the optical input and output beams (red) on a diamond prism surface in close proximity to the optical resonator. The microwave tone is coupled in and out of the cavity using a coaxial pin coupler at the top of the cavity (gold). The prism, both lenses, and the microwave tuning cylinder (gold shaded area inside the lower ring) positions can be adjusted with eight linear piezo positioners. (b) Optical reflection spectrum of the WGM resonator at base temperature (approximately 7 mK). The optical pump mode at $\omega_p/(2\pi) \approx 193.5$ THz (green) and the signal mode (blue) are critically coupled and separated by one free spectral range (FSR, dashed lines). On resonance 38% of the optical power is reflected without entering the WGM resonator due to imperfect optical mode overlap Λ (horizontal dotted line). The lower sideband mode (red) is chosen to couple to a mode family of different polarization, which splits it and facilitates the single-sideband selectivity of the converter. (c) Reflection spectrum of the microwave cavity at base temperature (approximately 7 mK) for the tuning cylinder in its up position (blue line) and in its down position (red line). With a tuning range of approximately 0.5 GHz we can readily match the cavity frequency with that of the optical free spectral range $\mathrm{FSR}/(2\pi) = 8.818$ GHz (dashed line).

overlap with the two optical modes. Here we use type-0 frequency conversion, where all the participating waves are polarized parallel to the material's optic and symmetry axis, addressing the highest electro-optic tensor component of $LiNbO_3$. We work with two optical modes of the WGM resonator that are spectrally separated by the resonator's optical FSR as shown in Fig. 1(b). The pump mode has an azimuthal number $m_p \approx 20 \times 10^3$ and the signal mode $m_o = m_p + 1$. The $m_p - 1$ mode's participation in the resonant interaction is suppressed due to its avoided crossing with another mode family [15], leaving only two optical modes in the process. We use an antireflection-coated diamond prism to feed the optical pump into the optical resonator via evanescent coupling. The prism is attached to a linear piezo positioning stage that allows us to accurately tune the extrinsic optical coupling rate $\kappa_{\mathrm{ex},o}$ *in situ*. The continuous-wave optical pump is an approximately 10 kHz linewidth coherent laser tone that is locked to the resonance of the optical pump WGM at $\omega_p/(2\pi) \approx 193.5$ THz for conversion measurements. The cryostat optical input line consists of a single-mode fiber with a GRIN lens at its end to focus the optical beam at the prism-WGM resonator coupling point. The reflected optical pump is collected with a second GRIN lens and coupled to the output line fiber for further measurements at room temperature.

At base temperature (approximately 7 mK) we measure an optical mode separation $\mathrm{FSR}/(2\pi) = 8.818$ GHz and an intrinsic optical loss rate $\kappa_{\mathrm{in},o} = 9.46$ MHz, which corresponds to a quality factor $Q_{\mathrm{in},o} = 2.0 \times 10^7$—a reduction by a factor 10 (5) from the measured room-temperature value outside (inside) the microwave cavity. The chosen optical pump and signal modes have a contrast of 62% at critical coupling ($Q_{\mathrm{ex},o} = Q_{\mathrm{in},o}$), as shown in Fig. 1(b), due to an imperfect spatial field mode overlap $\Lambda^2 = 0.38$ between the optical WGM and the optical input beam (see Appendix B). In this work we keep the optical system critically coupled to maximize the optical photon number for a given input power. The optical signal at $\omega_o = \omega_p + \mathrm{FSR}$ for optical to microwave conversion is created using a suppressed-carrier single-sideband modulator and sent through the same optical path as the pump tone; see Appendix A.

The chosen microwave cavity mode undergoes one oscillation around a full azimuthal roundtrip ($m_e = 1$), and its frequency is matched to the optical FSR in order to fulfil the conditions of phase matching and energy conservation. We use an aluminum cylinder centered below the WGM resonator and attached to a vertical piezo positioner that shifts the microwave resonance frequency $\omega_e/(2\pi)$ from 8.70 to 9.19 GHz at base temperature, as shown in Fig. 1(c). Microwave tones are sent to the device through a heavily attenuated transmission line and subsequently coupled to the cavity via a coaxial pin coupler mounted in the top part of the cavity, as shown in Fig. 1(a). The reflected microwave tone and the down-converted optical signal pass two circulators before amplification and measurement with a vector network analyzer (VNA) or an electronic spectrum analyzer (ESA); see Appendix A. From the VNA reflection measurements, we extract the resonance frequency ω_e, the intrinsic loss rate $\kappa_{\mathrm{in},e} = 6.7$ MHz, and the extrinsic coupling rate $\kappa_{\mathrm{ex},e} = 3.7$ MHz of the microwave resonance mode.

IV. BIDIRECTIONAL CONVERSION

In our system the microwave-to-optics and optics-to-microwave photon conversion efficiencies are equal [28]. The total input-output electro-optic photon conversion

efficiency, defined on resonance, is given as

$$\eta_{\rm tot} = \eta_e \eta_o \Lambda^2 \frac{4C}{(1+C)^2} \tag{4}$$

with coupling efficiencies $\eta_k = \kappa_{{\rm ex},k}/\kappa_k$ and $\kappa_k = \kappa_{{\rm in},k} + \kappa_{{\rm ex},k}$. We determine the bidirectional conversion efficiency of the device $\eta_{\rm tot} = \sqrt{\eta_{eo}\eta_{oe}}$, independent of the specifics of the measurement setup [36], such as the optical and microwave input attenuations β_1, β_3 and output amplifications β_2, β_4 (see Appendix D). Performing four independent measurements of the coherent scattering parameters $|S_{ij}|^2 \propto |\hat{a}_{{\rm out},i}/\hat{a}_{{\rm in},j}|^2$ with $i,j = \{e,o\}$ for every optical pump power setting

$$\eta_{\rm tot} = \sqrt{\frac{|S_{eo}(\omega_0)|^2 |S_{oe}(\omega_0)|^2}{|S_{ee}(\omega_\Delta)|^2 |S_{oo}(\omega_\Delta)|^2}} = \sqrt{\frac{\beta_1 \eta_{eo} \beta_4 \, \beta_3 \eta_{oe} \beta_2}{\beta_1 \beta_2 \, \beta_3 \beta_4}}, \tag{5}$$

we obtain the *in-situ* calibrated device efficiency $\eta_{\rm tot}$ from the optical fiber to the microwave coaxial line. Here the optics-to-microwave $|S_{eo}|^2$ and microwave-to-optics $|S_{oe}|^2$ power ratios are measured on resonance $\omega_0 = \omega_e, \omega_o$ and the reflected optical $|S_{oo}|^2$ and microwave $|S_{ee}|^2$ tones are measured at a detuning such that $|\omega_\Delta - \omega_0| \gg \kappa_e, \kappa_o$, respectively. For higher accuracy, we take into account frequency-dependent baseline variations using the full measured reflection scattering parameters.

In Fig. 2(a) we show the measured values of the total conversion efficiency $\eta_{\rm tot}$ (light blue) and the calculated internal conversion efficiency $\eta_{\rm int} = \eta_{\rm tot}/(\eta_e \eta_o \Lambda^2)$ (dark blue) together with Eq. (4) taking into account measured cavity linewidth changes (red lines) as a function of the incident optical pump P_p. As the pump power increases, the conversion efficiency departs only slightly from the expected linear behavior for the low cooperativity limit ($C \ll 1$) (dashed lines). For $P_p \approx 700$ μW (arrow), $\eta_{\rm tot}$ drops because the aluminum cavity undergoes a phase transition from the superconducting to the normal conducting state, which is accompanied by a sudden increase of $\kappa_{{\rm in},e}$; see Appendix C. The highest conversion efficiency $\eta_{\rm tot} = 3.16 \times 10^{-4}$ is reached for the maximum available pump power $P_p = 1.48$ mW that our laser can provide, where the refrigerator base plate reaches a steady-state temperature of $T_f = 320$ mK, which corresponds to a minimal microwave mode occupancy of $N_f = 0.36$ in continuous-wave mode.

From the measured values of the bidirectional conversion efficiency $\eta_{\rm tot}$ and coupling rates $\kappa_{{\rm in},e}$ at each optical pump power P_p, which is related to the drive strength and pump photon number $n_p = |\alpha|^2 = 4P_p \Lambda^2 \kappa_{{\rm ex},o}/(\hbar \omega_p \kappa_o^2)$, we extract the values of the multiphoton cooperativity in the system, ranging from $C = 3.24 \times 10^{-7}$ for the lowest to $C = 1.68 \times 10^{-3}$ for the highest P_p. From this we deduce the maximum internal photon conversion efficiency $\eta_{\rm int} = 4C/(1+C)^2$ of 0.67%. We find very good agreement between the measured conversion efficiency and Eq. (4) (solid red lines) for $g/(2\pi) = 40$ Hz, close to

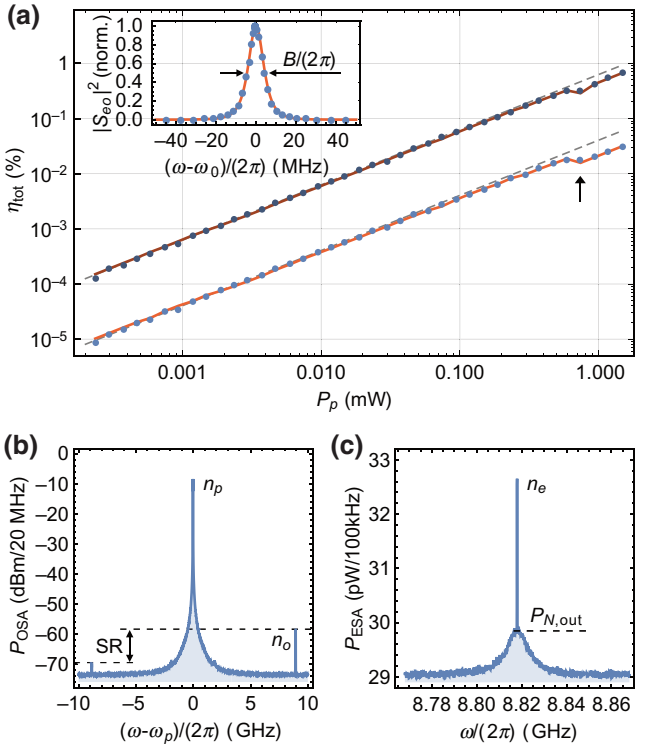

FIG. 2. Bidirectional microwave-optics conversion. (a) Measured photon conversion efficiency $\eta_{\rm tot}$ (light blue points) and inferred internal device efficiency $\eta_{\rm int} = \eta_{\rm tot}/(\eta_e \eta_o \Lambda^2)$ (dark blue points) together with theory (red lines), i.e., Eq. (4) taking into account measured cavity linewidth changes. The dashed lines are linear fits for the ten lowest power data points, respectively. The arrow marks the input power where the aluminum cavity goes from super to normal conducting. The inset shows the measured and normalized coherent optics-to-microwave conversion power ratio for $P_p = 18.7$ μW and $P_o = 267$ nW, as a function of the detuning between the optical signal frequency and ω_o (blue points) together with theory, Eq. (6) (red line), indicating the conversion bandwidth $B/(2\pi) = 9.0$ MHz. (b) Measured optical power spectrum for microwave-to-optical conversion at $P_p = 1.48$ mW. The weak coherent microwave tone $P_e = 1.0$ nW generates two optical sidebands (blue and red) with a suppression ratio of SR = 10.7 dB. The center and sideband peaks are proportional to the intracavity pump n_p and converted optical signal n_o photon numbers, respectively. The noise floor is set by the resolution bandwidth. (c) Measured power spectrum for optical-to-microwave conversion at $P_p = 2.35$ μW. The weak optical input signal $P_o = 161$ nW generates a single coherent microwave tone at $\omega_o - \omega_p$. In this particular example $n_e = 1.2$ intracavity microwave photons are generated with an incoherent noise floor $P_{N,\rm out}$ corresponding to an added output conversion noise of $N_{\rm out} = 0.4$ photons s^{-1} Hz^{-1} in the center of the microwave cavity bandwidth.

the directly measured (simulated) value of 36.1 Hz (36.2 Hz) at room temperature.

The normalized optics-to-microwave conversion as a function of the optical signal frequency is shown in the inset of Fig. 2(a). The solid red line corresponds to the theoretical expectation for the conversion spectrum [28]

$$\frac{|S_{ij}(\omega-\omega_0)|^2}{|S_{ij}(0)|^2} = \left[\left(1-\frac{4(\omega-\omega_0)^2}{\kappa_o\kappa_e}\right)^2+\frac{4(\omega-\omega_0)^2(\kappa_o+\kappa_e)^2}{\kappa_o^2\kappa_e^2}\right]^{-1}, \tag{6}$$

where κ_e and $\kappa_o/(2\pi) = 18.92$ MHz are independently extracted from direct reflection measurements. The bandwidth $B/(2\pi) = 9.0$ MHz at $P_p = 18.7$ μW with $\kappa_e/(2\pi) = 11.32$ MHz is in excellent agreement with the theoretical model for both conversion directions (see Appendix D). Here $B/(2\pi)$ increases from 8.51 MHz (calculated, $\kappa_e = 10.45$ MHz) for the lowest to 10.68 MHz (measured, $\kappa_e = 14.85$ MHz) for the highest optical pump power.

Selective up-conversion is an important feature of electro-optic transducers, because of the intrinsic noiseless nature of the up-conversion process. In Fig. 2(b) we display the measured microwave-to-optics conversion power spectrum corresponding to the highest pump power. Single sideband conversion with a suppression ratio of 10.7 dB in favor of up-conversion can be observed. This is expected from the asymmetric FSR in our WGM resonator due to the splitting of the lower sideband mode as shown in Fig. 1(b). The generated microwave output power spectrum from the optics-to-microwave conversion is shown in Fig. 2(c), where the peak at the center represents the coherently converted signal power at the microwave cavity output and the broadband incoherent baseline is due to the thermal noise added to the microwave output as a result of optical absorption.

V. ADDED NOISE

The optical pump causes dielectric heating due to absorption in the lithium niobate. In addition, stray light and evanescent fields can lead to direct breaking of Cooper pairs in the superconducting cavity. Both effects cause an increased surface resistance and in turn a larger microwave cavity linewidth $\kappa_{in,e}$ (see Appendix C). The optical heating causes an increase of the microwave cavity bath N_b and the microwave waveguide bath N_{wg}, both are related to the incoherent microwave mode occupancy

$$N_e = \eta_e N_{wg} + (1-\eta_e)N_b, \tag{7}$$

which leads to radiative cooling [37,38] for $N_{wg} < N_b$. The two bath populations are directly accessible via the detected output noise spectrum given by

$$N_{det}(\omega) = \frac{4\kappa_{in,e}\kappa_{ex,e}}{\kappa_e^2+4\omega^2}\left(N_b - N_{wg}\right) + N_{wg} + N_{sys} \tag{8}$$

in the low cooperativity limit. The conversion noise at the output port of the device $N_{out} = N_{det} - N_{sys}$ in units of photons s^{-1} Hz^{-1} is related to the measured power spectrum P_{ESA} via $N_{det}(\omega) = P_{ESA}(\omega)/(\hbar\omega_e\beta_4)$. Here $N_{sys} = 12.74 \pm 0.36$ and $\beta_4 = (67.05 \pm 0.16)$ dB are the calibrated noise photon number and gain of the measurement setup as referenced to the converter output port.

In Figs. 3(a)–3(c) we show the measured noise spectrum obtained by normalizing with a no-pump baseline reference measurement when the sample is cold $N_{det} = N_{sys}P_{ESA}/P_{ESA(P_p=0)}$ for three different pump powers with the same y-axis scale and no signal tone applied. For the lowest pump power $P_p = 0.23$ μW, only the N_{sys} offset is discernible [dashed black lines in panels (a)–(c)]. For the intermediate power $P_p = 14.82$ μW, the total output microwave noise $N_{out} = 1.01 \pm 0.07$ appears as a Lorentzian curve (blue line) with a broadband noise background $N_{wg} = 0.13 \pm 0.04$ (red dashed line). For the largest applied power $P_p = 1.48$ mW, we observe a maximum of $N_{out} = 5.51 \pm 0.20$ and $N_{wg} = 1.64 \pm 0.08$, significantly hotter than the dilution refrigerator base plate at $N_f = 0.36$. This is expected for a steady-state localized heat source, such as the optically pumped dielectric resonator, which has a finite temperature-dependent thermalization rate to equilibrate with the environment.

The added conversion noise referenced to the device output N_{out} (blue), the broadband waveguide noise N_{wg} (red), the microwave bath N_b (yellow), and mode occupancy N_e (green) for different optical pump powers P_p are shown in Fig. 3(d). Subphoton microwave output noise as low as $N_{out} = 0.03^{+0.04}_{-0.03}$ and microwave mode occupancies as low as $N_e = 0.025 \pm 0.005$ are achieved for a continuous-wave pump power of $P_p = 0.59$ μW where the total conversion efficiency is $\eta_{tot} = 2.3 \times 10^{-7}$. In the low-power limit the laser fluorescence noise is found to be a negligible contribution to the observed ground-state occupancy and the resulting very low conversion noise, as discussed in Appendix D.

As the pump power is increased, we observe a smooth growth of the waveguide noise starting from an equivalent temperature of $T_{wg} = 78^{+50}_{-17}$ mK and roughly proportional to $\sqrt{P_p}$ over 4 orders of magnitude. This is expected if the effective thermal conductivity to the cold refrigerator bath of approximately constant temperature is increasing linearly such that the heat flow q matches the dissipated part of the pump power $q \propto P_p \propto T \times \Delta T$, as predicted [39] for normal conducting metals such as the copper coaxial port attached to the superconducting cavity.

In contrast, for the microwave bath we observe three distinct regions of heating. Up to about 2 μW, the scaling is

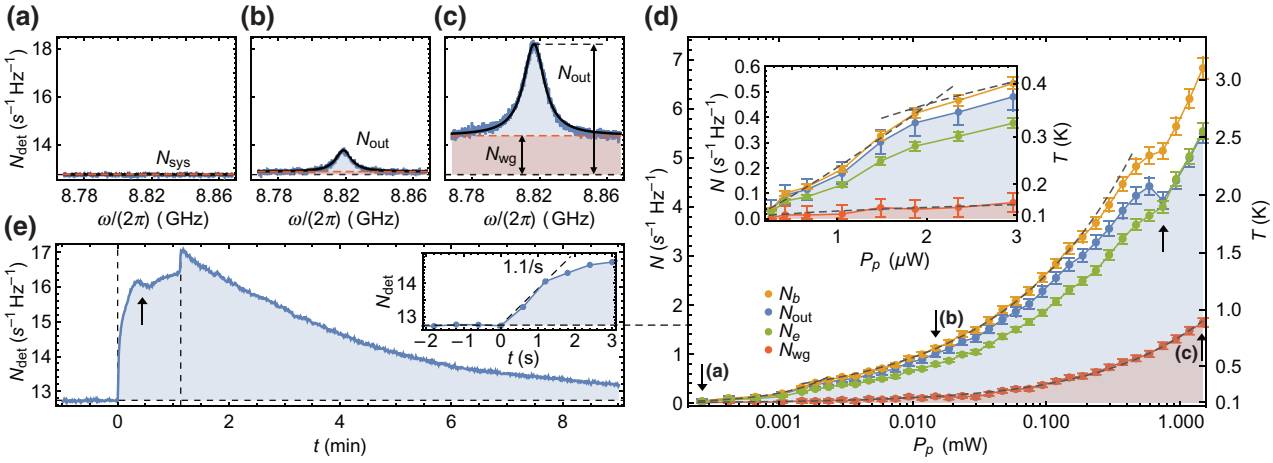

FIG. 3. Conversion noise and mode population. (a)–(c) Measured microwave output noise spectrum (blue line) in units of photons s^{-1} Hz^{-1} for (a) $P_p = 0.23$ μW, (b) 14.82 μW, and (c) 1.48 mW together with a fit to Eq. (8) (black line). In all three panels the dashed black line indicates the measurement system noise floor N_{sys} and the dashed red line indicates the broadband noise offset N_{wg}. (d) External waveguide bath population N_{wg} (red), total output noise photons N_{out} (blue), microwave mode bath N_b (yellow), and mode occupancy N_e (green) as a function of P_p. The arrows indicate values extracted from panels (a), (b) and (c), as well as where the superconducting phase transition occurs. The error bars of N_{wg} and N_{out} at low P_p are dominated by systematic errors due to slow absolute variations of the baseline of ± 0.03 quanta. The error bars of N_b represent the 95% confidence interval of the fit to Eq. (8), which also dominates the uncertainty of N_e since $N_{wg} < N_b$. The error bars at high P_p are dominated by the accuracy of the N_{sys} calibration. The shown error bars are the extrema of these absolute and relative uncertainties. The inset shows the region where the microwave bath occupancy $N_b < 1$ on a linear scale. The dashed gray lines indicate fitted power laws, specifically $N_{wg} \propto P_p^{0.55}$ over the full range of powers, $N_b \propto P_p^{1.14}$ up to $P_p \approx 2$ μW (see inset), and $N_b \propto P_p^{0.45}$ at higher powers. (e) Microwave output noise N_{out} measured on resonance over a 500 kHz resolution bandwidth in units of photons s^{-1} Hz^{-1} (blue line) on top of the measurement system noise floor N_{sys} (dashed horizontal line) as a function of time. The system is excited with a rectangular optical pulse of $P_p = 1.48$ mW and a length of 68 s (dashed vertical lines). The arrow indicates the time of approximately 30 s when superconductivity breaks, the cavity quality factor degrades, and the frequency detunes from the measurement frequency. This process is reversed at the end of the pulse when the cavity tunes back and the detected noise increases temporarily. The inset shows the fastest timescale, i.e., the initial heating rate of $dN_{out}/dt \approx 1.1$ noise photons s^{-1}.

approximately linear, which is expected for local heating with a fixed thermalization to the cold bath. The thermal conductivity of superconducting aluminum far below the critical temperature is exponentially suppressed [39], so this thermalization could be due to radiation or direct excitation of quasiparticles. In this important range of noise photon numbers, a high conductivity copper cavity might therefore show a significantly slower trend. Above 2 μW, the scaling is approximately $\sqrt{P_p}$, which indicates that part of the cavity, such as the small rings holding the disk, are normal conducting. This is confirmed by an increase in the internal losses (see Appendix C). At $P_p \approx 0.7$ mW we see a sharp drop in the output noise due to a sudden increase of $\kappa_{in,e}$ from 8.6 to 11.2 MHz. The temporarily slower increase of N_b suggests that this is also accompanied by a higher thermalization rate to the cold refrigerator bath, indicating that the entire aluminum cavity undergoes a phase transition at this input power. This interpretation of the data is backed up by stable cavity properties beyond this power (see Appendix C). The lowest measured bath occupancies are consistent with qubit measurements for a similar amount of shielding without optics [40] and could be further improved with sensitive radiometry measurements [41,42].

In Fig. 3(e) we show the time dependence of the measured output noise when the system is excited with a resonant optical square pulse with a rise time of 1 ms. Facilitated by its macroscopic device design with a large heat capacity and contact surface area to the cold refrigerator bath, we observe that the fastest heating timescale at the onset of the square pulse is as low as 1.1 photons s^{-1}. Assuming—as a worst-case scenario—a linear increase of the heating rate with the applied power, we can project $N_{out} < 10^{-4}$ for a single 100 ns long pulse of power 1 W. For this power $C > 1$ with unity internal conversion efficiency and interesting new physics to be unlocked. Examples include the strong coupling limit of electro optics with a repeated coherent energy exchange between microwave and optical photons, the emergence of parametric instabilities and self-oscillations [28], as well as efficient spontaneous parametric down-conversion for deterministic entanglement generation [34].

VI. CONCLUSION AND OUTLOOK

The presented bidirectional microwave-optical interface operates in the quantum ground state $N_e \ll 1$, as verified by measuring the minimal noise $N_{\text{out}} \ll 1$ added to a converted microwave output signal. Compared to recent probabilistic unidirectional transduction of quantum level signals, we show somewhat lower [24] and orders of magnitude higher [23] efficiency. The very high bandwidth of 10.7 MHz for continuous-wave conversion compared to typical 100 Hz repetition rates in previous experiments provides a very promising outlook to be able to also verify the quantum statistics using sensitive heterodyne [34] or photon detection measurements [43] in the near future.

Bandwidth-matched high-power pulsed operation schemes together with quality factor improvements based on new materials and lower-loss clamping geometries [34], as well as stronger coupled lower mode volume modes and improved packaging, should also enable deterministic protocols due to the observed slow heating timescales, i.e., the conversion of quantum level signals with an equivalent input noise $N_{\text{in}} = N_{\text{out}}/\eta_{\text{tot}} \ll 1$. This opens a long sought for possibility to implement fast and deterministic entanglement distribution between microwave and optical fields [34,43], for optically mediated remote entanglement of superconducting qubits [44], for extending the range of current fiber optic quantum networks [45], and for new multiplexed cryogenic circuit control and readout strategies [46–48].

The data and code used to produce the figures in the main part of this manuscript are available online [49].

ACKNOWLEDGMENTS

The authors acknowledge the support of T. Menner, A. Arslani, and T. Asenov from the Miba machine shop for machining the microwave cavity, and thank S. Barzanjeh, F. Sedlmeir, and C. Marquardt for fruitful discussions. This work is supported by IST Austria and the European Research Council under Grant No. 758053 (ERC StG QUNNECT). W.H. is the recipient of an ISTplus postdoctoral fellowship with funding from the European Union's Horizon 2020 research and innovation program under the Marie Skłodowska-Curie Grant No. 754411. G.A. is the recipient of a DOC fellowship of the Austrian Academy of Sciences at IST Austria. J.M.F. acknowledges support from the Austrian Science Fund (FWF) through BeyondC (F71) and the European Union's Horizon 2020 research and innovation program under Grant No. 899354 (FET Open SuperQuLAN). H.G.L.S. acknowledges support from the Aotearoa/New Zealand's MBIE Endeavour Smart Ideas Grant No UOOX1805.

APPENDIX A: MEASUREMENT SETUP

The measurement setup used to characterize the performance of the electro-optic converter is shown in Fig. 4.

APPENDIX B: OPTICAL RESONATOR

1. WGM resonator fabrication

The WGM resonator is manufactured from a z-cut congruent undoped lithium niobate wafer. The resonator initial dimensions are a major radius of $R = 2.5$ mm, a curvature radius of $\rho \approx 0.7$ mm, and an initial thickness $d = 0.5$ mm. The lateral surface is polished with diamond slurry from 9 μm (rms particle diameter) down to 1 μm. Subsequently, the resonator is thinned to a 0.15 mm thickness with 5 μm diamond slurry in a lapping machine [50]. Top and bottom surfaces are then finished by chemical-mechanical polishing.

2. Optical prism coupling

We couple the optical pump into the resonator via frustrated total internal reflection between the prism and the resonator surface. The optical beam coming from the cryostat input optical fiber is focused to the coupling window with an angle $\Phi_c \approx 50^\circ$ using a GRIN lens [see Fig. 1(a)]. The reflected pump and the converted optical signal are caught by a second GRIN lens and directed to the cryostat output optical fiber. The diamond prism is an isosceles triangle with basis angle 53° and height 0.8 mm. The prism's input and output sides are antireflection coated, and it is fixed from the backside to a copper wire as shown in Fig. 1(a). The copper wire goes through a small canal outside the microwave cavity and is attached to a linear piezo-positioning stage (PS). This way the distance d between the WGM resonator and the prism coupling surface can be controlled with nanometer-scale precision.

In order to reduce GRIN lens misalignments during cool down, we machine a single piece, oxygen-free copper holder that has the prism-WGM resonator coupling point at its center. Furthermore, we set up a low-temperature realignment system that consists of two ANPx101-LT and one ANPz101-LT PSs from attocube for each GRIN lens, allowing us to align them in the x-y-z direction. A feedback algorithm tracks the overall optical transmission as well as the optical mode contrast during the dilution refrigerator cooldown to 3 K where the final alignments are performed before condensation and further cool down to the cryogenic base temperature of about 7 mK.

3. Optical characterization

The optical resonator is characterized by analyzing its reflection spectrum. We sweep the frequency $\omega/(2\pi)$ of an optical tone over several gigahertz around 1550 nm and measure the intensity of the reflected signal on a photodiode (Fig. 4). In Fig. 5(a) we show the pump mode spectrum

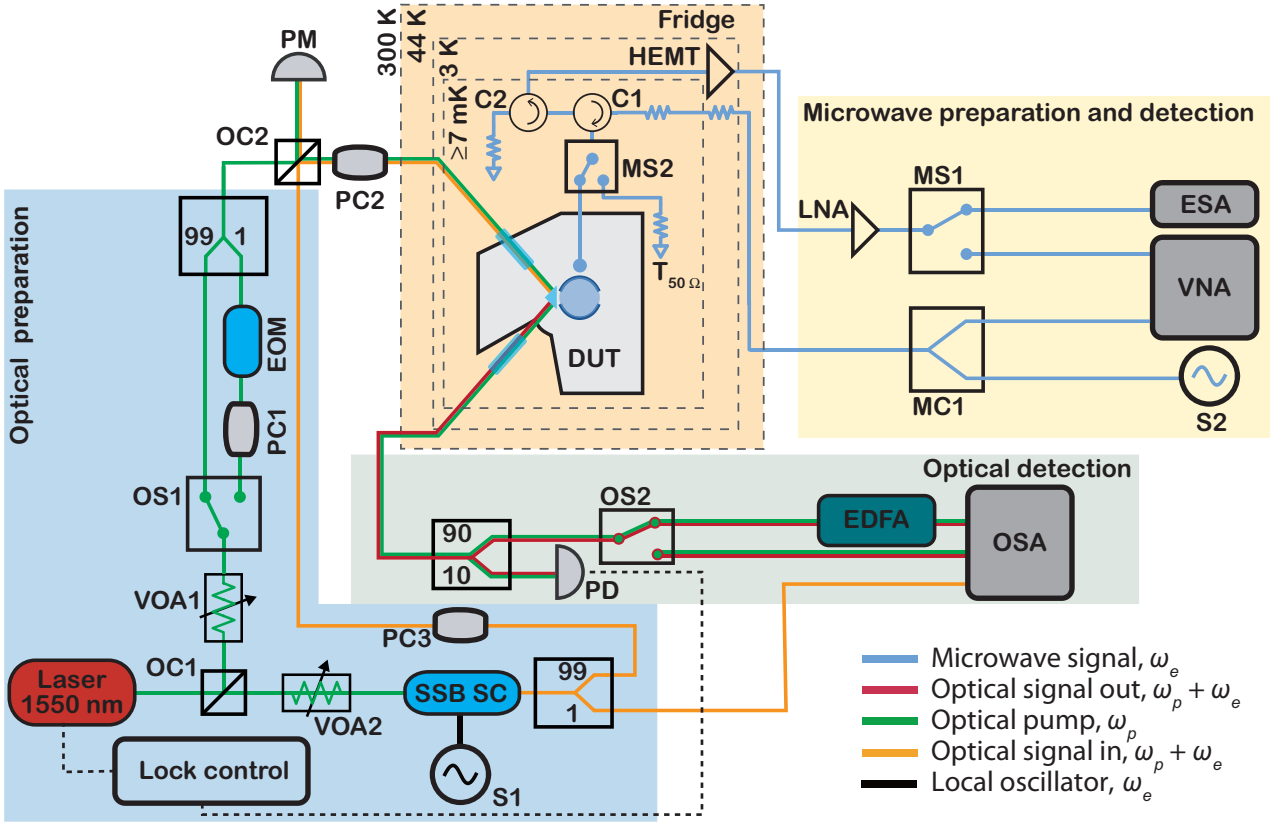

FIG. 4. Measurement setup. A tunable laser is equally split (50:50) into two paths at the optical coupler OC1. The upper path is used as the optical pump and it goes through a variable optical attenuator VOA1 that allows us to vary P_p. The optical pump can then be either sent directly to the cryostat fiber, or it can go first through an electro-optic modulator (EOM) in order to create sidebands for spectroscopy calibration. The second path (horizontal) is used to generate the optical signal. It also goes through a variable optical attenuator and is then frequency up-shifted by ω_e (approximately FSR) using a single-sideband EO modulator with suppressed carrier (SSB SC) driven by a microwave source with local oscillator frequency ω_e (S1). A small fraction (1%) of this signal is picked up and sent directly to an optical spectrum analyzer (OSA) for sideband and carrier suppression ratio monitoring. The rest (99%) is recombined with the pump at OC2, sent to the fridge input fiber, and the total power is monitored with a power meter (PM). The optical tones are focused on the prism with a GRIN lens that then feeds the WGM resonator via evanescent coupling. Polarization controllers PC2 and PC3 are set to achieve maximum coupling to a TE polarized cavity mode. The reflected (or created) optical sideband signal and the reflected pump are collected with the second GRIN lens and coupled to the cryostat output fiber. The optical signal is then split: 90% of the power goes to the OSA and 10% is sent to a photodiode (PD), which is used for mode spectroscopy and to lock on the optical mode resonance during the conversion measurement. The 90% arm is either sent directly to the OSA, or goes through an erbium doped fiber amplifier (EDFA) for amplification, depending on the microwave-to-optics converted signal power. On the microwave side, the signal is sent from the microwave source S2 (or from the VNA for microwave mode spectroscopy) to the fridge input line via the microwave combiner (MC1). The input line is attenuated with attenuators distributed between 3 K and 10 mK with a total of 60 dB in order to suppress room-temperature microwave noise. Circulator C1 redirects the reflected tone from the cavity to the amplified output line, while C2 redirects noise coming in from the output line to a matched 50 Ω termination. The output line is amplified at 3 K by a HEMT amplifier and then at room temperature again with a low noise amplifier (LNA). The output line is connected to switch MS1, to select between an ESA or a VNA measurement. Lastly, microwave switch MS2 allows us to swap the device under test (DUT) for a temperature $T_{50\,\Omega}$ controllable load, which serves as a broadband noise source in order to calibrate the output line's total gain and added noise (see Appendix D 2).

for a TE polarized tone, whose polarization is parallel to the WGM resonator's symmetry and optical axis. The optical FSR for this mode is measured by superimposing it with EOM-generated sidebands from modes one FSR away [15] (see Fig. 4 for the EOM). The measured optical FSR changed from 8.79 GHz at room temperature to 8.82 GHz at base temperature.

To characterize the coupling to the optical system, we measure the optical mode spectrum for different positions of the prism, thus changing $\kappa_{\mathrm{ex},o}$. The normalized spectrum of the chosen mode follows the analytical model [51]

$$\frac{|S_{oo}(\omega-\omega_o)|^2}{|S_{oo}(\Delta\omega)|^2}=1-\frac{4\kappa_{\mathrm{ex},o}\Lambda^2(\kappa_o-\Lambda^2\kappa_{\mathrm{ex},o})}{\kappa_o^2+4(\omega-\omega_o)^2}, \quad \text{(B1)}$$

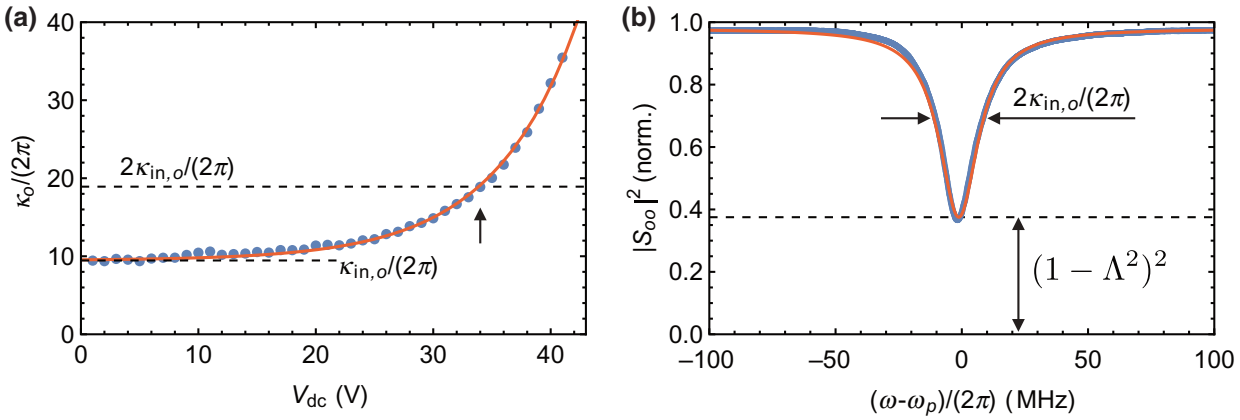

FIG. 5. Optical coupling. (a) Measured $\kappa_o/(2\pi)$ as a function of piezo voltage V_{dc} (blue points) and exponential fit (red line). For large distances $d \propto -V_{\mathrm{dc}}$, we find that $\kappa_o/(2\pi) = \kappa_{\mathrm{in},o}/(2\pi) = 9.46$ MHz. The lower dashed line indicates the lower limit $\kappa_o = \kappa_{\mathrm{in},o}$. The upper dashed line shows the critical coupling condition where $\kappa_{\mathrm{in},o} = \kappa_{\mathrm{ex},o}$ and $\kappa_o = 2\kappa_{\mathrm{in},o}$ with the corresponding V_{dc} (vertical arrow). (b) Measured optical reflection spectrum around 1550 nm at base temperature for critical coupling [arrow in panel (a)]. Because of imperfect optical mode matching quantified by $\Lambda^2 = 0.38$, an amount proportional to $(1-\Lambda^2)^2$ of the input power is reflected at critical coupling (dashed line).

where the factor Λ describes the electric field overlap between the evanescent tail of the beam reflecting on the prism and the resonator mode and $\Delta\omega \gg \kappa_o$. The external coupling rate $\kappa_{\mathrm{ex},o}$ strongly depends on the distance d between the prism and the resonator

$$\kappa_{\mathrm{ex},o}(d) = \kappa_{\mathrm{ex},o}^{\mathrm{max}} \exp(-k_0 d), \tag{B2}$$

where $\kappa_{\mathrm{ex},o}^{\mathrm{max}} = \kappa_{\mathrm{ex},o}(d=0)$ and $k_0 = \omega_o\sqrt{n_{\mathrm{LN}}^2 - 1}/c$ [51], n_{LN} is the refractive index of lithium niobate, and c is the speed of light in vacuum. We control the distance by applying a dc voltage to the piezo stage $d \propto -V_{\mathrm{dc}}$ and measure the transmission spectrum. The fitted total optical linewidth $\kappa_o = \kappa_{\mathrm{ex},o} + \kappa_{\mathrm{in},o}$ as a function of V_{dc} is shown in Fig. 5(a). From an exponential fit of the measured κ_o (red line), we extract the offset corresponding to $\kappa_{\mathrm{in},o}/(2\pi) = 9.46$ MHz. Furthermore, at critical coupling ($\kappa_{\mathrm{ex},o} = \kappa_{\mathrm{in},o}$), we extract $\Lambda^2 = 0.38$ from a fit to Eq. (B1) as shown in Fig. 5(b). The intracavity photon number for the optical pump is given by

$$n_p(\omega) = \frac{P_p \Lambda^2}{\hbar\omega_p} \frac{4\kappa_{\mathrm{ex},o}}{\kappa_o^2 + 4(\omega-\omega_p)^2}, \tag{B3}$$

where P_p stands for the optical pump power sent to the resonator-prism interface. The WGM resonators's FSR and linewidth do not change over the full optical pump power range.

APPENDIX C: MICROWAVE CAVITY

1. Design

The conversion efficiency between the optical and microwave modes depends strongly on the microwave electric field confinement at the rim of the WGM resonator. Our hybrid system, based on a 3D microwave cavity and a WGM resonator, offers a high degree of freedom to control the microwave spatial distribution $\psi_e(\vec{r})$, microwave resonance frequency ω_e, and external coupling rate $\kappa_{\mathrm{ex},e}$. We used finite element method (FEM) simulations in order to find suitable design parameters for the microwave cavity.

A schematic drawing of the microwave cavity with its important dimensions is shown in Fig. 6(a). The $LiNbO_3$ WGM resonator is clamped between two aluminum rings (highlighted in blue). In this way we maximize the microwave electric field overlap with the optical mode, the latter being confined close to the rim of the WGM resonator [see Fig. 6(b)]. The microwave spatial electric field distribution shows one full oscillation along the circumference of the WGM resonator [see Figs. 6(c) and 6(d)] to fulfil the phase matching condition. The aluminum rings have a cut in the middle in order to maximize the field participation factor and minimize potential magnetic losses in the dielectric. The cavity's cylindrical inner volume can be tailored to achieve the desired microwave resonance frequency, which can then be tuned by approximately 500 MHz *in situ*, by moving an aluminum cylinder placed inside the lower ring. This allows us to compensate the thermal contraction induced frequency shift that occurs during cool down of the device. The top right part of the shown top half of the cavity is cut out in order to facilitate the assembly of the device.

2. FEM simulation of electro-optic coupling

From FEM simulations we obtain the single-photon spatial electric field distribution given as $E_{e,z}(r,z,\phi) = E_{e,z}^{\mathrm{max}}\Psi_e(r,z)[1+f(\phi)]\cos(\phi)$, where $\Psi_e(r,z)$ is normalized

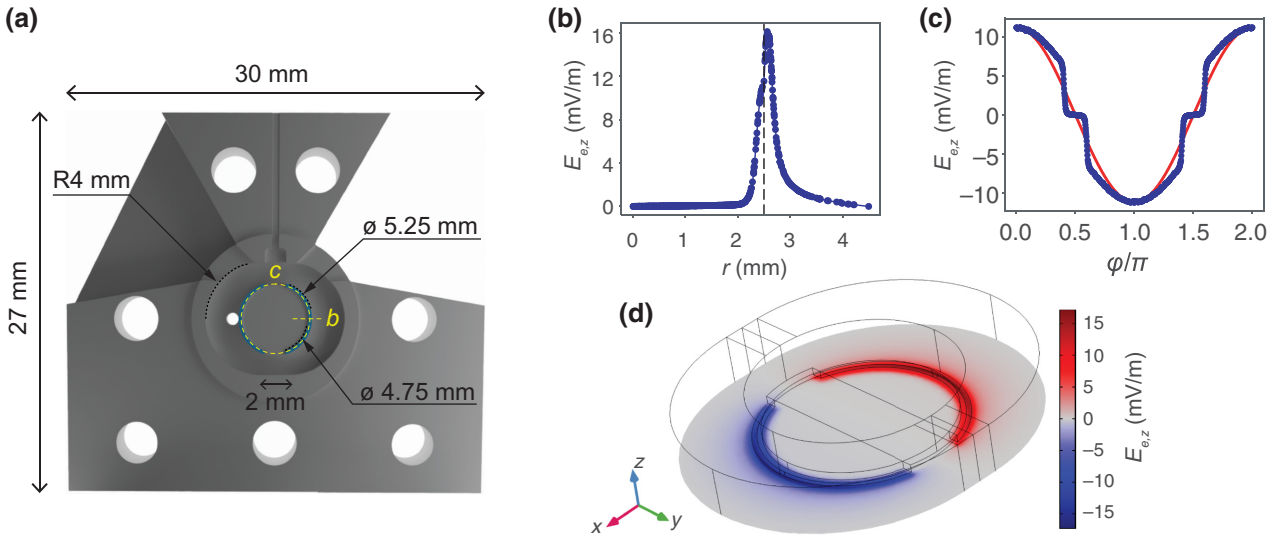

FIG. 6. Microwave cavity design. (a) Computer-aided design drawing of the top part of the aluminum microwave cavity. (b) FEM simulation of the single-photon electric field distribution of the $m = 1$ mode of the microwave cavity. Shown is the z component of the field along the radial axis at $z = 0$ (in the center of the WGM) and $\phi = 0$ [yellow dashed line in panel (a)]. The vertical dashed line marks the position of the edge of the WGM resonator. (c) FEM simulation of the z component of the single-photon electric field taken at the position of the optical mode maximum and plotted as a function of the azimuthal angle ϕ [yellow dashed circle in panel (a)]. The red line is a sinusoidal function as a guide to the eye. (d) FEM simulation of the z component of the single-photon electric field in the $z = 0$ plane for the $m = 1$ microwave resonance.

to 1, $r = \sqrt{x^2 + y^2}$ and $\phi = \arctan(y/x)$; see also Fig 6(d). For this simulation, we used the reported [52] dielectric permittivity of lithium niobate at 9 GHz, i.e., $\varepsilon_e = (42.5, 42.5, 26)$. The function $f(\phi)$ is symmetric and describes the deviation of the azimuthal field distribution from a pure sinusoidal shape, as shown in Fig. 6(c). The optical mode is distributed along the ring $\{r = r_o, z = 0, \phi \in [0\ 2\pi]\}$ and the maximum value of the microwave electric field on this ring is $E_{eo} = E_{e,z}(r_o, 0, \phi_{\max}) = E_{e,z}^{\max}\Psi_e(r_o, 0) = 11.1$ mV/m. The optical mode being a clockwise (C) traveling wave, we must decompose the stationary microwave field into a clockwise and a counterclockwise (CC) traveling wave in order to calculate the coupling

$$\begin{aligned} E_{e,z}(r_o, 0, \phi, t) &= E_{eo}[1 + f(\phi)]\cos(\phi)\cos(\omega_e t) \\ &= \frac{E_{eo}}{4}[1 + f(\phi)](e^{-i(\phi-\omega_e t)} + e^{i(\phi-\omega_e t)} \\ &\quad + e^{-i(\phi+\omega_e t)} + e^{i(\phi+\omega_e t)}) \\ &= E_C^+ + E_C^- + E_{CC}^+ + E_{CC}^-. \end{aligned} \tag{C1}$$

By introducing $E_{e,z}(r_o, 0, \phi, t)$ into Eq. (2), we get (E_{CC}^+ and E_{CC}^- do not participate in the interaction)

$$g = n^2 r\sqrt{\frac{\omega_p \omega_o}{4V_o V_p}}\frac{E_{eo}}{4}\int dV[\psi_o^* \psi_p e^{-i\phi} + \psi_o^* \psi_p e^{-i\phi} f(\phi)], \tag{C2}$$

where n is the refractive index of the pump ω_p and the sideband ω_o. The effective mode volumes V_k are given by the integral $\int dV \psi_k \psi_k^*$ over the respective optical field spatial distributions $\psi_p = \Psi_p(r, \theta)e^{-im}$ and $\psi_o = \Psi_o(r, \theta)e^{-i(m+1)}$. The second term in the integral in Eq. (C2) is zero due to the symmetry of $f(\phi)$, reducing Eq. (C2) to

$$g = \tfrac{1}{8} n^2 \omega_o r_{33} E_{eo}, \tag{C3}$$

where $n = 2.13$ ($\varepsilon_o \approx \varepsilon_p = 4.54$) is the extraordinary refractive index (dielectric permittivity) of the lithium niobate at $\omega_o \approx \omega_p = (2\pi) \times 193.5$ THz and $r_{33} = 31$ pm/V is the electro-optic coefficient. For these values, we estimate $g_{\text{sim}}/(2\pi) = 38$ Hz at room temperature.

3. Room temperature measurement of g

The system is assembled at room temperature and a microwave tone is fed into the cavity with a coaxial probe coupler of length 1.2 mm. By displacing the tuning cylinder, the cavity frequency $\omega_e/(2\pi)$ could be shifted from 8.40 to 9.22 GHz, slightly shifted up compared to numerical simulations. We attribute this to small air gaps between the WGM resonator and the aluminum disk, which decrease the effective dielectric constant between the electrodes. To match the measured frequency range exactly, we introduce an air gap of only about 1 μm in the simulations, bringing down the estimated coupling to $g_{\text{sim}}/(2\pi) = 36.2$ Hz.

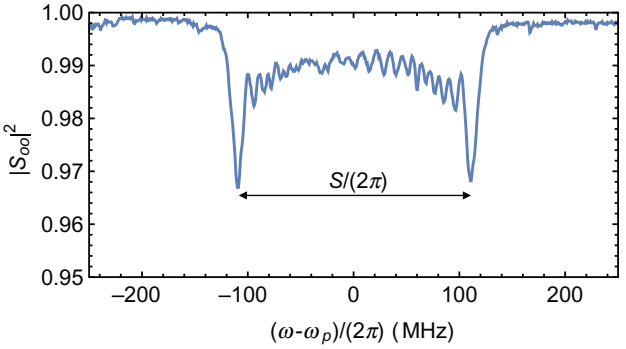

FIG. 7. Direct measurement of g. Measured optical mode splitting of $S/(2\pi) = 220$ MHz at room temperature, obtained with an input power of 9.3 dBm applied to the microwave cavity at ω_e. Here $S \approx 4\sqrt{n_e}g_{\mathrm{rt}}$ is related to the measured single-photon coupling strength $g_{\mathrm{rt}}/(2\pi) = 36.1$ Hz via the calculated intracavity photon number $n_e = 2.3 \times 10^{12}$ [46].

At $\omega_e = \mathrm{FSR}$, the microwave mode has the parameters $\kappa_{\mathrm{ex},e}/(2\pi) = 2.48$ MHz and $\kappa_{\mathrm{in},e}/(2\pi) = 29$ MHz. We infer the nonlinear coupling constant of the system by applying a strong microwave drive tone to the cavity and measuring the resulting optical mode splitting $S \approx 4\sqrt{n_e}g_{\mathrm{rt}}$, as described in Ref. [46]. In Fig. 7 we show a measured splitting of $S/(2\pi) = 220$ MHz for a 9.3 dBm microwave pump power applied on resonance. This corresponds to $g_{\mathrm{rt}}/(2\pi) = 36.1$ Hz, a fivefold improvement compared to earlier results [15], and in excellent agreement with the simulations.

4. Microwave cavity fabrication

The microwave cavity is milled out of a block of pure aluminum (5N). It is divided into a lower and upper part that are closed after placing the WGM resonator and the prism using brass screws. The internal geometry can be seen in Fig. 6(a). When closing the cavity, the pure aluminum rings get in contact with the optical resonator. The rings deform slightly, which minimizes the formation of air gaps that would otherwise reduce g.

5. Microwave characterization

The microwave resonance tuning range is measured with a VNA connected to the cryostat transmission line, as shown in Fig. 4. The resonance frequency can be tuned from 8.70 to 9.19 GHz, as shown in the main text. This range is at a slightly higher frequency compared to the

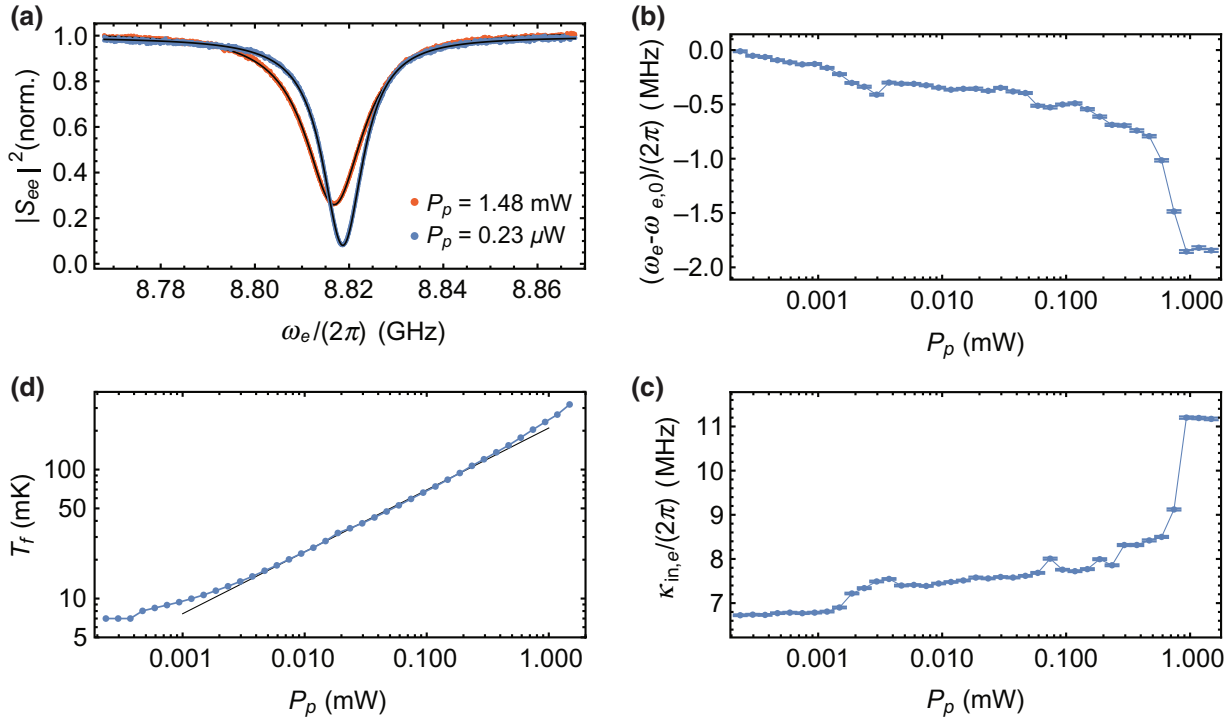

FIG. 8. Microwave cavity properties. (a) Measured reflection spectra of the microwave resonance for the minimum (blue) and maximum (red) applied optical pump powers P_p together with Lorentzian fits (black lines). (b) Fitted microwave resonance frequency $\omega_e - \omega_{e,0}$ as a function of P_p with the error bars indicating the 95% confidence interval of the fit. Here $\omega_{e,0}$ is the fitted resonance frequency obtained for the minimum optical pump power of $P_p = 0.23$ μW. (c) Fitted microwave intrinsic loss rate $\kappa_{\mathrm{in},e}$ as a function of P_p with the error bars indicating the 95% confidence interval of the fit. (d) The mixing chamber temperature sensor reading T_f of the dilution refrigerator as a function of the optical pump power P_p (blue points) and a power-law fit $T_f \propto P_p^{0.48}$ to the intermediate power range (black line).

room-temperature range. We attribute this to thermal contraction that leads to small air gaps. The decay rates of the microwave mode at the cryogenic base temperature and the lowest optical input power are $\kappa_{\mathrm{ex},e}/(2\pi) = 3.7$ MHz and $\kappa_{\mathrm{in},e}/(2\pi) = 6.7$ MHz.

Unlike the optical system, the microwave cavity's parameters undergo changes as a function of the optical pump power P_p applied to the WGM resonator. In Fig. 8(a) we show the normalized spectra of the microwave resonance at the smallest (blue) and largest (red) optical pump powers together with a Lorentzian fit. From these measurements we extract the microwave resonance frequency ω_e [shown in panel (b)] and the internal loss rates $\kappa_{\mathrm{in},e}$ [shown in panel (c)] as a function of P_p. The extrinsic coupling rate $\kappa_{\mathrm{ex},e}$ depends only on the fixed geometry and is approximately constant. In contrast, $\kappa_{\mathrm{in},e}$ increases and ω_e decreases with increasing P_p until the microwave cavity undergoes the superconducting phase transition. Once the normal conducting state is reached, a further increase of P_p does not lead to any perceptible change, as can be seen in Figs. 8(b) and (c). The microwave resonance red shift [see Fig. 8(c)] and the $\kappa_{\mathrm{in},e}$ increase are expected due to optically induced creation of quasiparticles in the aluminum cavity, as discussed for example in Ref. [17]. While the local heating is significant, the temperature of the mixing chamber plate of the dilution refrigerator follows a slow ($P_p^{0.48}$ at intermediate powers) rise from $T_f = 7$ mK up to $T_f = 320$ mK, as shown in Fig. 8(d).

APPENDIX D: FREQUENCY CONVERSION

1. Theoretical model

We model the input-output response of the electro-optic system by taking into account external coupling rates $\kappa_{\mathrm{ex},i}$ and internal loss rates $\kappa_{\mathrm{in},i}$ to the external and internal thermal baths, as shown in Fig. 9(a). First, we define the coherent conversion matrix as the ratio between the output and the input photon numbers in the absence of noise

$$\eta_{ij} = n_{\mathrm{out},i}/n_{\mathrm{in},j} \tag{D1}$$

for $i,j \in \{o,e\}$. The matrix η_{ij} is derived in Refs. [28,51] and its explicit form is given as

$$\begin{bmatrix} n_{\mathrm{out},o}(\omega) \\ n_{\mathrm{out},e}(\omega) \end{bmatrix} = M(\omega) \begin{bmatrix} |(i\omega + \Lambda^2\kappa_{\mathrm{ex},o} - \kappa_o/2)(\kappa_e/2 - i\omega) + |G|^2|^2 & \Lambda^2\kappa_{\mathrm{ex},e}\kappa_{\mathrm{ex},o}|G|^2 \\ \Lambda^2\kappa_{\mathrm{ex},e}\kappa_{\mathrm{ex},o}|G|^2 & |(i\omega + \kappa_{\mathrm{ex},e} - \kappa_e/2)(\kappa_o/2 - i\omega) + |G|^2|^2 \end{bmatrix} \times \begin{bmatrix} n_{\mathrm{in},o}(\omega) \\ n_{\mathrm{in},e}(\omega) \end{bmatrix}, \tag{D2}$$

where $M^{-1}(\omega) = |(-i\omega + \kappa_o/2)(-i\omega + \kappa_e/2) + |G|^2|^2$ and $G = \sqrt{n_p}g$, with n_p given by Eq. (B3).

The noise performance is one of the most important characteristics of a quantum converter. In our system, we consider two noise sources that affect the microwave mode. The first one is the noise in the waveguide N_{wg}, which can be seen as the external bath of the 50 Ω semirigid copper coaxial port. The second noise source is given by the internal bath of the system N_b as shown in Fig. 9(a). The optical laser noise N_{ln} in the fiber and the internal optical bath noise $N_{b,o}$ are neglected, because the former can be filtered and $\hbar\omega_o \gg k_B T$; see also Appendix D 5. In the low cooperativity limit we also neglect the thermal occupancy of the optical mode N_o, which would contribute to the optical output noise $N_{\mathrm{out},o}$.

We define the noise conversion matrix σ_{ij} as the ratio between the output noises and the relevant microwave input noise to the system in the absence of any coherent signal as [28,51]

$$\begin{bmatrix} N_{\mathrm{out},o}(\omega) \\ N_{\mathrm{out}}(\omega) \end{bmatrix} = M(\omega) \begin{bmatrix} \Lambda^2\kappa_{\mathrm{ex},e}\kappa_{\mathrm{ex},o}|G|^2 & \Lambda^2\kappa_{\mathrm{in},e}\kappa_{\mathrm{ex},o}|G|^2 \\ |(i\omega + \kappa_{\mathrm{ex},e} - \kappa_e/2)(-i\omega + \kappa_o/2) + |G|^2|^2 & \kappa_{\mathrm{in},e}\kappa_{\mathrm{ex},e}|(-i\omega + \kappa_o/2)|^2 \end{bmatrix} \begin{bmatrix} N_{\mathrm{wg}}(\omega) \\ N_b(\omega) \end{bmatrix}, \tag{D3}$$

where $N_{\mathrm{wg}}(\omega) = [\exp(\hbar\omega/k_B T_{\mathrm{wg}}) - 1]^{-1}$ and $N_b(\omega) = [\exp(\hbar\omega/k_B T_{\mathrm{b}}) - 1]^{-1}$ are wideband distributions compared to $\kappa_{\mathrm{ex},e}$, such that they can be approximated as constant.

The full input-output model including vacuum noise is given as

$$\mathbf{n}_{\mathrm{out}}(\omega) + \mathbf{N}_{\mathrm{out}}(\omega) = \eta_{ij}(\omega) \cdot \mathbf{n}_{\mathrm{in}}(\omega) + \sigma_{ij}(\omega) \cdot \mathbf{N}_{\mathrm{wg},b}(\omega) + \mathbf{N}_{\mathrm{vac}} \tag{D4}$$

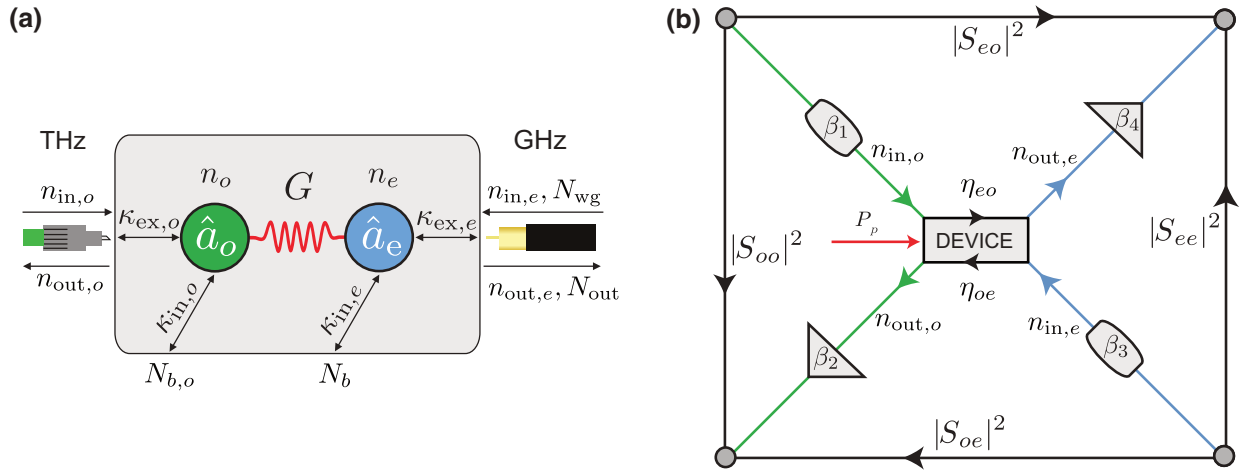

FIG. 9. Electro-optic photon conversion. (a) Schematic representation of the microwave ($\hat{a}_e$) and optical ($\hat{a}_o$) modes with coherent populations n_e and n_o and incoherent occupancies N_e and N_o (not shown). The electro-optic coupling strength $G = \sqrt{n_p}g$ originates from the Pockels effect in the lithium niobate WGM resonator. Both modes are coupled to an internal thermal bath N_b and $N_{b,o}$ with the rates $\kappa_{\mathrm{in},i}$. They are also coupled to the respective coaxial and fiber waveguides with the rates $\kappa_{\mathrm{ex},i}$. At finite temperature the microwave waveguide has a thermal bath occupancy N_{wg} and also hosts the total output noise N_{out} measured in the experiment. (b) The S_{ij} coefficients are defined between the microwave and optical input and output ports outside the cryostat (gray circles). Attenuation for the optical input and output paths are $\beta_1 = -4.81$ dB and $\beta_2 = -5.5$ dB (without EFDA), or the gain $\beta_2 = +30.8$ dB (with EFDA). An observed gain saturation at high pump powers is measured and corrected. Attenuation and gain of the microwave input and output paths are $\beta_3 = -74.92$ dB and $\beta_4 = +67.05$ dB, respectively. From two conversion measurements on resonance (S_{ij}) and two reflection measurements out of resonance (S_{ii}) where $\eta_{ii} = 1$, we infer the bidirectional photon conversion efficiency of the device according to Eq. (5) and referenced to the input and output photon numbers $n_{\mathrm{in},i}$ and $n_{\mathrm{out},i}$.

with $\mathbf{N}_{\mathrm{vac}} = \left[\begin{smallmatrix}0.5\\0.5\end{smallmatrix}\right]$.

The device is fixed to the mixing chamber of a dilution refrigerator with a base temperature of approximately 7 mK, preventing direct access to the device's input and output ports; see Fig. 4. In Fig. 9(b) we present a simplified schematic of the measurement setup, with attenuation and gain β_1, β_2 for the optical path and β_3, β_4 for the microwave path. We define the measured scattering matrix including the transmission lines on resonance as

$$|S_{ij}(\omega_0)|^2 = \frac{1}{(1+C)^2}\begin{bmatrix}\beta_2(2\Lambda^2\eta_o - 1 + C)^2\beta_1 & \Lambda^2\beta_2 4\eta_o\eta_e C\beta_3\\ \beta_4 4\eta_o\eta_e C\beta_1\Lambda^2 & \beta_4(2\eta_e - 1 + C)^2\beta_3\end{bmatrix}, \tag{D5}$$

where $\eta_i = \kappa_{\mathrm{ex},i}/\kappa_i$ and $C = 4n_p g^2/(\kappa_o\kappa_e)$ stands for the multiphoton electro-optic cooperativity. For large signal detuning $\omega_\Delta = \omega - \omega_0 \gg \kappa_e, \kappa_o$ with $\omega_0 = \omega_e, \omega_o$ the scattering matrix simplifies to

$$|S_{ij}(\omega_\Delta)|^2 = \begin{bmatrix}\beta_2\beta_1 & 0\\ 0 & \beta_4\beta_3\end{bmatrix}. \tag{D6}$$

We infer the bidirectional conversion efficiency at each optical pump power by measuring the microwave-to-optics and optics-to-microwave transmissions on resonance and the microwave-to-microwave and optics-to-optics reflections off resonance. The total device efficiency can then be defined as

$$\eta_{\mathrm{tot}} = \sqrt{\frac{|S_{eo}(\omega_0)|^2|S_{oe}(\omega_0)|^2}{|S_{ee}(\omega_\Delta)|^2|S_{oo}(\omega_\Delta)|^2}} = \eta_o\eta_e\Lambda^2\frac{4C}{(1+C)^2}. \tag{D7}$$

In the limits for $C \ll 1$ this can be approximated as

$$\eta_{\mathrm{ext}} \approx 4\eta_o\eta_e\Lambda^2 C = \frac{64\eta_o^2\eta_e\Lambda^4 g^2 P_p}{\hbar\omega_p\kappa_o^2\kappa_e}. \tag{D8}$$

This equation is used to calculate the nonlinear coupling constant in the main text. It can also be shown that in the limit of $C \ll 1$, $\Lambda < 1$ and $\eta_e \neq 0.5$, the bidirectional efficiency can be estimated using only resonant

measurements

$$\eta_{\rm tot} = (2\Lambda^2\eta_o - 1)(2\eta_e - 1)\sqrt{\frac{|S_{eo}(\omega_0)|^2|S_{oe}(\omega_0)|^2}{|S_{ee}(\omega_0)|^2|S_{oo}(\omega_0)|^2}} = \eta_o\eta_e\Lambda^2\frac{4C}{(1+C)^2}, \quad \text{(D9)}$$

where Λ and η_i are measured accurately from microwave and optical spectroscopy.

The system noise originates from the microwave resonator and waveguide baths N_b and $N_{\rm wg}$, respectively. By applying the matrix to the noise vector in Eq. (D3) we can solve for the output noise $N_{\rm out}$, which simplifies in the low cooperativity limit ($G^2 \ll \kappa_o\kappa_e$) to

$$N_{\rm out}(\omega) = \frac{4\kappa_{{\rm in},e}\kappa_{{\rm ex},e}}{\kappa_e^2 + 4\omega^2}\left(N_b - N_{\rm wg}\right) + N_{\rm wg} + 0.5. \quad \text{(D10)}$$

In our system the resonator bath N_b is always hotter than the waveguide bath $N_{\rm wg}$, because the dominant part of the dielectric absorption takes place inside the resonator. Therefore, the output noise spectrum $N_{\rm out}(\omega)$ always consists of a Lorentzian function with amplitude $N_b - N_{\rm wg}$ on top of the broadband noise level $N_{\rm wg}$, as shown in Fig. 3. Finally, following the same formalism, the integrated (dimensionless) internal microwave mode occupancy is given as

$$N_e = \frac{\kappa_{{\rm ex},e}N_{\rm wg} + \kappa_{{\rm in},e}N_b}{\kappa_e} = \eta_e N_{\rm wg} + (1-\eta_e)N_b. \quad \text{(D11)}$$

2. Microwave calibration

The microwave transmission line is characterized by the input attenuation β_3, the output gain β_4, and the total added noise of the output line $N_{\rm sys}$. The output line is first calibrated by using a 50 Ω load, a resistive heater, and a thermometer that are thermally connected. Weak thermal contact to the mixing chamber of the dilution refrigerator allows us to change the temperature $T_{50\,\Omega}$ of the 50 Ω load without heating up the mixing chamber. We vary $T_{50\,\Omega}$ from 21.5 mK to 1.8 K and measure the amplified thermal noise on a spectrum analyzer. The measured power spectral density $P_{\rm ESA}(\omega)$ is approximately constant around the microwave resonance frequency ω_e and its temperature dependence follows

$$P_{\rm ESA} = \hbar\omega_e\beta_4{\rm BW}\left[\frac{1}{2}\coth\left(\frac{\hbar\omega_e}{2k_BT_{50\Omega}}\right) + N_{\rm add}\right], \quad \text{(D12)}$$

where BW stands for the chosen resolution bandwidth, k_B is Boltzmann's constant, and $N_{\rm add}$ is the effective noise added to the signal at the output port of the device due to amplifiers and losses. At $T_{50\Omega} = 0$ K this reduces to $P_{\rm ESA} = \hbar\omega_e\beta_4{\rm BW}N_{\rm sys}$ with $N_{\rm sys} = N_{\rm add} + 0.5$.

In Fig. 10 we show the detected noise $N_{\rm det} - N_{\rm add} = P_{\rm ESA}/(\hbar\omega_e\beta_4{\rm BW}) - N_{\rm add}$ as a function of the load temperature $T_{50\,\Omega}$. The values for gain and added noise obtained from a fit to Eq. (D12) are 67.65 ± 0.05 dB and 10.66 ± 0.15, as shown in Fig. 10. The emitted black body radiation undergoes the same losses and gains, as shown in Fig. 4, except for an independently calibrated cable length difference immediately at the sample output, resulting in an additional loss of 0.6 ± 0.09 dB. Taking into account this additional loss we arrive at the corrected gain and system noise $\beta_4 = 67.05 \pm 0.16$ dB and $N_{\rm sys} = 12.74 \pm 0.36$. For the stated uncertainties, we take into account the 95% confidence interval of the fit, an estimated temperature sensor accuracy of ±2.5% over the relevant range, as well as the estimated inaccuracy in the cable attenuation difference. The input attenuation is then easily deduced from a VNA reflection measurement $|S_{ee}|^2$ that yields $\beta_3 = -74.92 \pm 0.16$ dB.

3. Optical calibration

The optical transmission lines consist mainly of two optical single-mode fibers. The input optical line starts from OC2 (see Fig. 4) and terminates at the WGM resonator-prism interface. The output optical line is defined from the WGM resonator-prism interface to the OSA (see Fig. 4). From the measured external conversion efficiencies $\eta_{\rm tot}$ and the microwave line calibration, we can determine the losses of the input and output transmission lines using

$$\frac{P_{{\rm out},o}}{\omega_o} = \beta_2\eta_{\rm tot}\beta_3\frac{P_{{\rm in},e}}{\omega_e}, \qquad \frac{P_{{\rm out},e}}{\omega_e} = \beta_4\eta_{\rm tot}\beta_1\frac{P_{{\rm in},o}}{\omega_o}, \quad \text{(D13)}$$

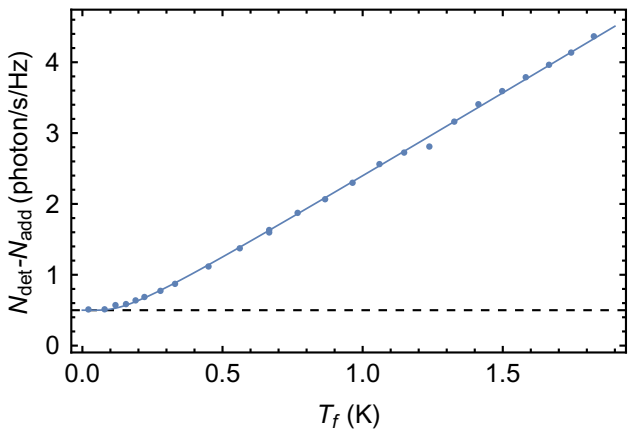

FIG. 10. System noise calibration. Measured noise (circles) together with a fit to Eq. (D12) (line) shown in units of photons using $N_{\rm det} - N_{\rm add} = P_{\rm ESA}/(\hbar\omega_e\beta_4{\rm BW}) - N_{\rm add}$. The dashed line indicates the vacuum noise.

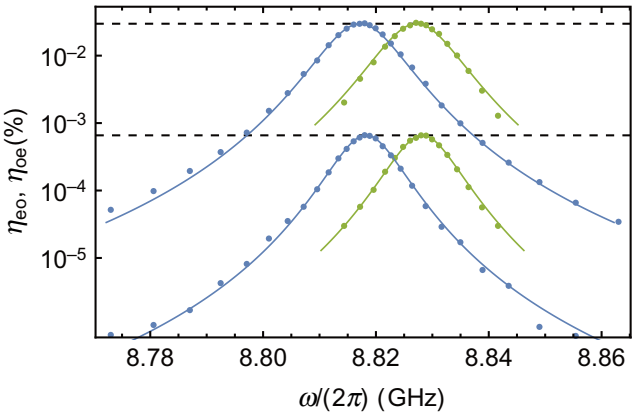

FIG. 11. Conversion bandwidth and bidirectionality. Measured total conversion efficiency η_{eo} (blue circles) and η_{oe} (green circles) as a function of output signal frequency ω (optics to microwave, blue) or $\omega = \omega_o - \omega_p$ (microwave to optics, green) for $P_p = 18.7$ μW and P_p=1.48 mW. Microwave-to-optics conversion (green) is displaced by 10 MHz for better visibility. Dashed lines indicate the maxima of the theory curves in agreement with the results reported in the main text.

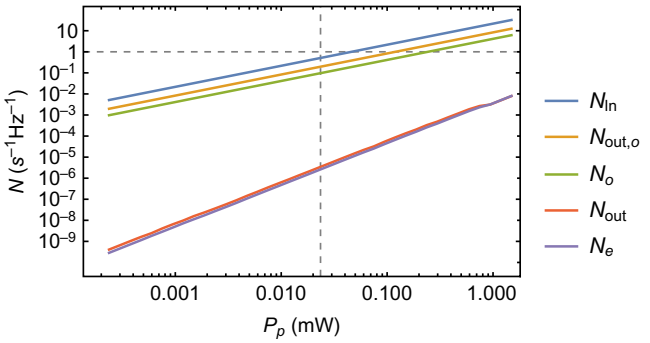

FIG. 12. Calculated noise photon numbers only due to measured laser fluorescence noise at $\omega_p + \mathrm{FSR}$. Shown are the broadband laser noise N_{ln}, the resulting optical mode occupancy N_o, optical output noise $N_{\mathrm{out},o}$ on resonance, microwave mode occupancy N_e, and the resulting output noise contribution on resonance N_{out} as a function of optical pump power P_p. The horizontal dashed line indicates a population of 1 and the vertical dashed line the pump power $P_p = 23.5$ μW where we measure $N_e = 1$ due to optical absorption heating.

where $P_{\mathrm{in},i}$ are the input powers of our transmission lines coming out from OC2 and S2 and $P_{\mathrm{out},i}$ are the measured powers at the end of the transmission lines measured with the OSA and ESA. The procedure yields the input attenuation $\beta_1 = -4.81$ dB and the output gain (via EDFA) $\beta_2 = +30.8$ dB. For measurements above $P_p = 0.1$ mW, we bypass the EDFA by switching OS2, resulting in an output attenuation of $\beta_2 = -5.5$ dB.

4. Bidirectionality

In Fig. 11 we show the measured total conversion efficiency as a function of signal frequency (dots) using Eq. (D13) together with theory (lines) using Eq. (6) in both conversion directions for two different pump powers. Because the optical calibration Eq. (D13) assumes symmetric bidirectionality we also find that the measurement results are perfectly symmetric. Nevertheless, direct measurements of β_1 taken at room temperature of -2.6 dB are in good agreement with the optical calibration. We attribute the additional loss of up to 2.2 dB to changes in the optical alignment during the cool down, e.g., in the cold angled physical contact fiber connector, as well as reflection loss at the first prism surface that is not included in the room temperature calibration.

5. Laser noise

The external cavity diode laser used in this work exhibits source spontaneous emission (SSE), which is accountable for the finite width of the main carrier peak in Fig. 2(b). A high resolution OSA measurement of the SSE power density yields $P_{\mathrm{ln}} = -65.6$ dBc/100 MHz (relative to the carrier power) centered at the upper sideband frequency $\omega_p + \mathrm{FSR}$. Using input-output formalism, we calculate the resulting mode occupancies only due to laser noise as shown in Fig. 12. All occupancies, including the optical ones, stay below 1 for the input power range up to which we report bidirectional conversion with mode occupancies less than 1 (dashed vertical line). We find that the impact of laser noise on the microwave population and the microwave conversion noise is negligible due to the relatively low cooperativities achieved in this work. In the future, the laser noise can be filtered for example with a narrow band Fabry-Pérot cavity to enable noise-free high cooperativity conversion at higher pump powers.

[1] F. Arute *et al.*, Quantum supremacy using a programmable superconducting processor, Nature **574**, 505 (2019).
[2] P. Magnard, S. Storz, P. Kurpiers, J. Schär, F. Marxer, J. Lütolf, J.-C. Besse, M. Gabureac, K. Reuer, A. Akin, B. Royer, A. Blais, and A. Wallraff, Microwave quantum link between superconducting circuits housed in spatially separated cryogenic systems, arXiv:2008.01642 [quant-ph] (2020).
[3] A. A. Clerk, K. W. Lehnert, P. Bertet, J. R. Petta, and Y. Nakamura, Hybrid quantum systems with circuit quantum electrodynamics, Nat. Phys. **16**, 257 (2020).
[4] G. Burkard, M. J. Gullans, X. Mi, and J. R. Petta, Superconductor-semiconductor hybrid-circuit quantum electrodynamics, Nat. Rev. Phys. **2**, 129 (2020).
[5] D. D. Awschalom, R. Hanson, J. Wrachtrup, and B. B. Zhou, Quantum technologies with optically interfaced solid-state spins, Nat. Photon. **12**, 516 (2018).
[6] A. W. Elshaari, W. Pernice, K. Srinivasan, O. Benson, and V. Zwiller, Hybrid integrated quantum photonic circuits, Nat. Photon. **14**, 285 (2020).

[7] H. J. Kimble, The quantum internet, Nature **453**, 1023 (2008).

[8] S. Wehner, D. Elkouss, and R. Hanson, Quantum internet: A vision for the road ahead, Science **362**, eaam9288 (2018).

[9] J. Capmany and D. Novak, Microwave photonics combines two worlds, Nat. Photon. **1**, 319 (2007).

[10] F. Lecocq, J. B. Clark, R. W. Simmonds, J. Aumentado, and J. D. Teufel, Mechanically Mediated Microwave Frequency Conversion in the Quantum Regime, Phys. Rev. Lett. **116**, 043601 (2016).

[11] N. J. Lambert, A. Rueda, F. Sedlmeir, and H. G. L. Schwefel, Quantum information technologies: Coherent conversion between microwave and optical photons – an overview of physical implementations, Adv. Quantum Technol. **3**, 2070011 (2020).

[12] N. Lauk, N. Sinclair, S. Barzanjeh, J. P. Covey, M. Saffman, M. Spiropulu, and C. Simon, Perspectives on quantum transduction, Quantum Sci. Technol. **5**, 020501 (2020).

[13] A. P. Higginbotham, P. S. Burns, M. D. Urmey, R. W. Peterson, N. S. Kampel, B. M. Brubaker, G. Smith, K. W. Lehnert, and C. A. Regal, Harnessing electro-optic correlations in an efficient mechanical converter, Nat. Phys. **14**, 1038 (2018).

[14] G. Arnold, M. Wulf, S. Barzanjeh, E. S. Redchenko, A. Rueda, W. J. Hease, F. Hassani, and J. M. Fink, Converting microwave and telecom photons with a silicon photonic nanomechanical interface, Nat. Commun. **11**, 4460 (2020).

[15] A. Rueda, F. Sedlmeir, M. C. Collodo, U. Vogl, B. Stiller, G. Schunk, D. V. Strekalov, C. Marquardt, J. M. Fink, O. Painter, G. Leuchs, and H. G. L. Schwefel, Efficient microwave to optical photon conversion: an electro-optical realization, Optica **3**, 597 (2016).

[16] L. Fan, C.-L. Zou, R. Cheng, X. Guo, X. Han, Z. Gong, S. Wang, and H. X. Tang, Superconducting cavity electro-optics: A platform for coherent photon conversion between superconducting and photonic circuits, Sci. Adv. **4**, eaar4994 (2018).

[17] J. D. Witmer, T. P. McKenna, P. Arrangoiz-Arriola, R. Van Laer, E. Alex Wollack, F. Lin, A. K.-Y. Jen, J. Luo, and A. H. Safavi-Naeini, A silicon-organic hybrid platform for quantum microwave-to-optical transduction, Quantum Sci. Technol. **5**, 034004 (2020).

[18] T. P. McKenna, J. D. Witmer, R. N. Patel, W. Jiang, R. V. Laer, P. Arrangoiz-Arriola, E. A. Wollack, J. F. Herrmann, and A. H. Safavi-Naeini, Cryogenic microwave-to-optical conversion using a triply-resonant lithium niobate on sapphire transducer, arXiv:2005.00897 [quant-ph] (2020).

[19] J. Holzgrafe, N. Sinclair, D. Zhu, A. Shams-Ansari, M. Colangelo, Y. Hu, M. Zhang, K. K. Berggren, and M. Lončar, Cavity electro-optics in thin-film lithium niobate for efficient microwave-to-optical transduction, arXiv:2005.00939 [quant-ph] (2020).

[20] A. Vainsencher, K. J. Satzinger, G. A. Peairs, and A. N. Cleland, Bi-directional conversion between microwave and optical frequencies in a piezoelectric optomechanical device, Appl. Phys. Lett. **109**, 033107 (2016).

[21] W. Jiang, C. J. Sarabalis, Y. D. Dahmani, R. N. Patel, F. M. Mayor, T. P. McKenna, R. Van Laer, and A. H. Safavi-Naeini, Efficient bidirectional piezo-optomechanical transduction between microwave and optical frequency, Nat. Commun. **11**, 1166 (2020).

[22] X. Han, W. Fu, C. Zhong, C.-L. Zou, Y. Xu, A. A. Sayem, M. Xu, S. Wang, R. Cheng, L. Jiang, and H. X. Tang, Cavity piezo-mechanics for superconducting-nanophotonic quantum interface, Nat. Commun. **11**, 3237 (2020).

[23] M. Forsch, R. Stockill, A. Wallucks, I. Marinković, C. Gärtner, R. A. Norte, F. van Otten, A. Fiore, K. Srinivasan, and S. Gröblacher, Microwave-to-optics conversion using a mechanical oscillator in its quantum ground state, Nat. Phys. **16**, 69 (2020).

[24] M. Mirhosseini, A. Sipahigil, M. Kalaee, and O. Painter, Quantum transduction of optical photons from a superconducting qubit, arXiv:2004.04838 [quant-ph] (2020).

[25] A. P. Reed, K. H. Mayer, J. D. Teufel, L. D. Burkhart, W. Pfaff, M. Reagor, L. Sletten, X. Ma, R. J. Schoelkopf, E. Knill, and K. W. Lehnert, Faithful conversion of propagating quantum information to mechanical motion, Nat. Phys. **13**, 1163 (2017).

[26] A. B. Matsko, A. A. Savchenkov, V. S. Ilchenko, D. Seidel, and L. Maleki, On fundamental quantum noises of whispering gallery mode electro-optic modulators, Opt. Express **15**, 17401 (2007).

[27] M. Tsang, Cavity quantum electro-optics, Phys. Rev. A **81**, 063837 (2010).

[28] M. Tsang, Cavity quantum electro-optics. II, Phys. Rev. A **84**, 043845 (2011).

[29] C. Javerzac-Galy, K. Plekhanov, N. R. Bernier, L. D. Toth, A. K. Feofanov, and T. J. Kippenberg, On-chip microwave-to-optical quantum coherent converter based on a superconducting resonator coupled to an electro-optic microresonator, Phys. Rev. A **94**, 053815 (2016).

[30] M. Soltani, M. Zhang, C. Ryan, G. J. Ribeill, C. Wang, and M. Loncar, Efficient quantum microwave-to-optical conversion using electro-optic nanophotonic coupled resonators, Phys. Rev. A **96**, 043808 (2017).

[31] D. A. Cohen, M. Hossein-Zadeh, and A. F. J. Levi, High-q microphotonic electro-optic modulator, Solid-State Electron. **45**, 1577 (2001).

[32] V. S. Ilchenko, A. A. Savchenkov, A. B. Matsko, and L. Maleki, Whispering-gallery-mode electro-optic modulator and photonic microwave receiver, J. Opt. Soc. Am. B **20**, 333 (2003).

[33] D. V. Strekalov, C. Marquardt, A. B. Matsko, H. G. L. Schwefel, and G. Leuchs, Nonlinear and quantum optics with whispering gallery resonators, J. Opt. **18**, 123002 (2016).

[34] A. Rueda, W. Hease, S. Barzanjeh, and J. M. Fink, Electro-optic entanglement source for microwave to telecom quantum state transfer, Npj Quantum Inf. **5**, 108 (2019).

[35] I. S. Grudinin, V. S. Ilchenko, and L. Maleki, Ultrahigh optical quality factors of crystalline resonators in the linear regime, Phys. Rev. A **74**, 063806 (2006).

[36] R. W. Andrews, R. W. Peterson, T. P. Purdy, K. Cicak, R. W. Simmonds, C. A. Regal, and K. W. Lehnert, Bidirectional and efficient conversion between microwave and optical light, Nat. Phys. **10**, 321 (2014).

[37] G. Santamaria Botello, F. Sedlmeir, A. Rueda, K. A. Abdalmalak, E. R. Brown, G. Leuchs, S. Preu, D.

Segovia-Vargas, D. V. Strekalov, L. E. García Muñoz, and H. G. L. Schwefel, Sensitivity limits of millimeter-wave photonic radiometers based on efficient electro-optic upconverters, Optica **5**, 1210 (2018).

[38] M. Xu, X. Han, C.-L. Zou, W. Fu, Y. Xu, C. Zhong, L. Jiang, and H. X. Tang, Radiative Cooling of a Superconducting Resonator, Phys. Rev. Lett. **124**, 033602 (2020).

[39] A. L. Woodcraft, Recommended values for the thermal conductivity of aluminium of different purities in the cryogenic to room temperature range, and a comparison with copper, Cryogenics **45**, 626 (2005).

[40] J. M. Fink, L. Steffen, P. Studer, L. S. Bishop, M. Baur, R. Bianchetti, D. Bozyigit, C. Lang, S. Filipp, P. J. Leek, and A. Wallraff, Quantum-to-Classical Transition in Cavity Quantum Electrodynamics, Phys. Rev. Lett. **105**, 163601 (2010).

[41] Z. Wang, M. Xu, X. Han, W. Fu, S. Puri, S. M. Girvin, H. X. Tang, S. Shankar, and M. H. Devoret, Quantum microwave radiometry with a superconducting qubit, arXiv:1909.12295 [quant-ph] (2019).

[42] M. Scigliuzzo, A. Bengtsson, J.-C. Besse, A. Wallraff, P. Delsing, and S. Gasparinetti, Primary thermometry of propagating microwaves in the quantum regime, arXiv:2003.13522 [quant-ph] (2020).

[43] C. Zhong, Z. Wang, C. Zou, M. Zhang, X. Han, W. Fu, M. Xu, S. Shankar, M. H. Devoret, H. X. Tang, and L. Jiang, Proposal for Heralded Generation and Detection of Entangled Microwave–Optical-Photon Pairs, Phys. Rev. Lett. **124**, 010511 (2020).

[44] P. Kurpiers, P. Magnard, T. Walter, B. Royer, M. Pechal, J. Heinsoo, Y. Salathé, A. Akin, S. Storz, J.-C. Besse, S. Gasparinetti, A. Blais, and A. Wallraff, Deterministic quantum state transfer and remote entanglement using microwave photons, Nature **558**, 264 (2018).

[45] H.-J. Briegel, W. Dür, J. I. Cirac, and P. Zoller, Quantum Repeaters: The Role of Imperfect Local Operations in Quantum Communication, Phys. Rev. Lett. **81**, 5932 (1998).

[46] A. Rueda, F. Sedlmeir, M. Kumari, G. Leuchs, and H. G. L. Schwefel, Resonant electro-optic frequency comb, Nature **568**, 378 (2019).

[47] A. Youssefi, I. Shomroni, Y. J. Joshi, N. Bernier, A. Lukashchuk, P. Uhrich, L. Qiu, and T. J. Kippenberg, Cryogenic electro-optic interconnect for superconducting devices, arXiv:2004.04705 [quant-ph] (2020).

[48] F. Lecocq, F. Quinlan, K. Cicak, J. Aumentado, S. A. Diddams, and J. D. Teufel, Control and readout of a superconducting qubit using a photonic link, arXiv:2009.01167 [quant-ph] (2020).

[49] https://doi.org/10.5281/zenodo.4266026.

[50] Y. Minet, L. Reis, J. Szabados, C. S. Werner, H. Zappe, K. Buse, and I. Breunig, Pockels-effect-based adiabatic frequency conversion in ultrahigh-Q, Opt. Express **28**, 2939 (2020).

[51] A. R. Rueda Sanchez, Doctoral thesis, Friedrich-Alexander-Universität Erlangen-Nürnberg (FAU) (2018).

[52] K. Wong, Properties of Lithium Niobate, EMIS Datareviews Series (INSPEC, The Institution of Electrical Engineers, London, UK, 2002).

npj | Quantum Information

www.nature.com/npjqi

ARTICLE OPEN

Electro-optic entanglement source for microwave to telecom quantum state transfer

Alfredo Rueda[1]*, William Hease[1], Shabir Barzanjeh[1] and Johannes M. Fink[1]*

We propose an efficient microwave-photonic modulator as a resource for stationary entangled microwave-optical fields and develop the theory for deterministic entanglement generation and quantum state transfer in multi-resonant electro-optic systems. The device is based on a single crystal whispering gallery mode resonator integrated into a 3D-microwave cavity. The specific design relies on a new combination of thin-film technology and conventional machining that is optimized for the lowest dissipation rates in the microwave, optical, and mechanical domains. We extract important device properties from finite-element simulations and predict continuous variable entanglement generation rates on the order of a Mebit/s for optical pump powers of only a few tens of microwatts. We compare the quantum state transfer fidelities of coherent, squeezed, and non-Gaussian cat states for both teleportation and direct conversion protocols under realistic conditions. Combining the unique capabilities of circuit quantum electrodynamics with the resilience of fiber optic communication could facilitate long-distance solid-state qubit networks, new methods for quantum signal synthesis, quantum key distribution, and quantum enhanced detection, as well as more power-efficient classical sensing and modulation.

npj Quantum Information (2019)5:108 ; https://doi.org/10.1038/s41534-019-0220-5

INTRODUCTION

The development of superconducting quantum processors has seen remarkable progress in the last decade,[1,2] but long-distance connectivity remains an unsolved problem. Coherent interconnects between superconducting qubits are currently restricted to an ultra-cold environment, which offers sufficient protection from thermal noise.[3,4] A hybrid quantum network[5] that combines the advanced control capabilities and the high-speed offered by superconducting quantum circuits, with the robustness, range,[6] and versatility[7] of more-established quantum telecommunication systems appears as the natural solution.[8] Entanglement between optical and microwave photons is the key ingredient for distributed quantum computing with such a hybrid quantum network and would pave the way to integrate advanced microwave quantum state synthesis capabilities[9–11] with existing optical quantum information protocols[12,13] such as quantum state teleportation[14,15] and secure remote quantum state preparation.[16,17]

Electro-optomechanical systems stand out as the most successful platforms to connect optical and microwave fields near losslessly and with minimal added noise.[18,19] Very recently, it has been shown that mechanical oscillators can also be used to deterministically generate entangled electromagnetic fields.[20] Mechanical generation of microwave-optical entanglement has been proposed[21–27] but an experimental realization remains challenging. Low-frequency mechanical transducers typically suffer from added noise and low bandwidth, whereas high-frequency piezoelectric devices require sophisticated wave matching and new materials, which so far results in low total interaction efficiencies,[28–30] comparable to magnon-based interfaces.[31]

Cavity electro-optic (EO) modulators are another proposed candidate[32–36] to coherently convert photons, or to effectively generate entanglement between microwave and optical fields, employing the Pockels effect and without the need for an intermediary oscillator. Here, a material with a large and broadband nonlinear polarizability $\chi^{(2)}$ is shared between an optical resonator and the capacitor of a microwave cavity,[37–41] a platform that has recently been used for efficient photon conversion with bulk[42] and thin-film crystals.[43]

In this paper, we propose a multi-resonant whispering gallery mode (WGM) cavity electro-optic modulator whose free spectral range (FSR) matches the microwave resonance frequency. It is tailored for optimal performance at ultra-low temperatures, in particular, with respect to unwanted optical heating and thermal occupation of the microwave mode. We minimize the necessary optical pump power by maximizing the optical quality factor using a millimeter sized and mechanically polished bulk single crystal disk resonator.[44] Compared with nano- and micron-scale modulators, its large size and surface area should facilitate a more-efficient coupling to the cold bath and its large heat capacity is expected to result in slow heating rates in pulsed operation schemes. Compared with previous work[42] the disk is clamped in the center to avoid disk damage, air gaps, and to minimize potential piezoelectric clamping losses. Importantly, finite-element modeling shows that a sufficient mode overlap and bandwidth at moderate pump powers can still be achieved using a combination of lithographically defined thin-film superconducting electrodes together with carefully shaped WGM disc cross-sections.

In the main part of the paper, we develop the theory to analytically predict the entanglement properties under realistic conditions such as finite temperature and asymmetric waveguide couplings. We show that it is feasible to deterministically generate MHz bandwidth continuous variable (CV) entanglement between the outputs of a pumped optical and a cold microwave resonator via spontaneous parametric downconversion. We also present its performance for direct conversion-based and teleportation-based communication, as quantified by the quantum state transfer fidelities for a set of typical quantum states. Our results indicate that the proposed entangler could serve as a repeater node to

[1]Institute of Science and Technology Austria, am Campus 1, 3400 Klosterneuburg, Austria. *email: aruedasa@ist.ac.at; jfink@ist.ac.at

enable long-distance hybrid quantum networks.[45] The developed theory results are applicable to any triply resonant electro-optic transducer implementation.

RESULTS

Hamiltonian of the system

As shown schematically in Fig. 1, we consider a WGM cavity electro-optic modulator containing a $\chi^{(2)}$ nonlinear medium that generates a nonlinear interaction between a single microwave cavity mode with frequency Ω and two modes of the WGM optical resonator corresponding to the central and the Stokes-sideband mode with resonance frequencies ω_c and ω_s, respectively. Such a single sideband situation can be achieved by making use of mode couplings of different polarization that lead to an asymmetry of the WGM resonator's FSR.[42] The total Hamiltonian describing the system is $\hat{H} = \hat{H}_0 + \hat{H}_{\rm int}$ in which the free energy Hamiltonian is[32–34,38,42]

$$\hat{H}_0 = \hbar\omega_c a_c^\dagger a_c + \hbar\omega_s a_s^\dagger a_s + \hbar\Omega a_\Omega^\dagger a_\Omega, \tag{1}$$

and the interaction Hamiltonian is

$$\hat{H}_{\rm int} = g(a_\Omega + a_\Omega^\dagger)(a_c^\dagger + a_s^\dagger)(a_c + a_s), \tag{2}$$

where $\hat{a}_c$, $\hat{a}_s$ are the annihilation operators of the central and Stokes-sideband modes of the optical resonator, respectively, whereas $\hat{a}_\Omega$ is the annihilation operator of the microwave cavity and g describes the coupling strength between the microwave and the two optical modes. Moving to the interaction picture with respect to $\hat{H}_0$ and setting $\Omega = \omega_c - \omega_s$, the system Hamiltonian reduces to

$$\hat{H} = g(\hat{a}_c^\dagger \hat{a}_s \hat{a}_\Omega + \hat{a}_\Omega^\dagger \hat{a}_s^\dagger \hat{a}_c). \tag{3}$$

The second part of this Hamiltonian describes a three-wave mixing process during which an optical photon with frequency ω_s and a microwave photon with frequency Ω are generated by annihilating an optical photon with frequency ω_c.

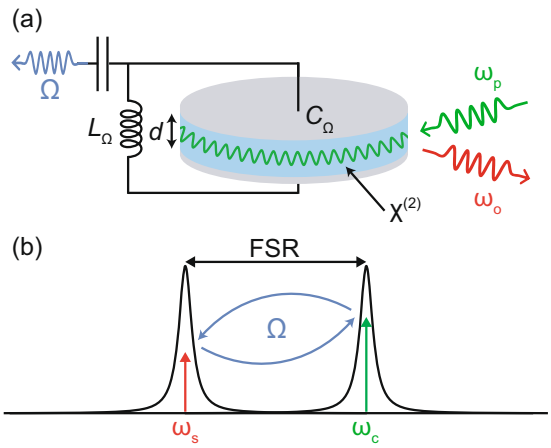

Fig. 1 Schematic representation of the cavity electro-optic modulator. **a** An optical WGM resonator with $\chi^{(2)}$ nonlinearity is confined between two metallic electrodes forming the capacitance C_Ω of a LC microwave resonator with resonance frequency $\Omega = 1/\sqrt{L_\Omega C_\Omega}$. An incident optical pump field at ω_p is down-converted into two outgoing correlated microwave-optical fields Ω and ω_o. **b** Power spectral density of the optical resonator. The two shown modes of the WGM resonator correspond to the central and Stokes-sideband modes with resonance frequencies ω_c and ω_s. Efficient microwave-optical interaction requires matching Ω with the free spectral range (FSR) of the optical mode. Here, the optical resonator is coherently pumped at resonance frequency $\omega_p = \omega_c$ and the output of the optical resonator is measured at the Stokes-Sideband frequency $\omega_o = \omega_s$.

The coupling strength g is determined by the spatial mode overlap of the electric fields $E_k = \sqrt{\hbar\omega_k/(2\epsilon_k V_k)}\psi_k(r,\theta,\phi)$ and the $\chi^{(2)}$ nonlinearity of the material:[38,42]

$$g = 2\epsilon_0\chi^{(2)}\sqrt{\frac{\hbar\omega_s\omega_c\Omega}{8\epsilon_s\epsilon_c\epsilon_\Omega V_c V_s V_\Omega}}\int dV\psi_s^*\psi_c\psi_\Omega. \tag{4}$$

where ϵ_0 is the vacuum permittivity, $\psi_k(r,\theta,\phi)$ the field distribution functions, ϵ_k and V_k are the relative permittivity and mode volume corresponding to mode k with $k = s, c, \Omega$, respectively. The field distributions can be written in terms of the cross-section $\Psi_k(r,\theta)$ and azimuthal distribution $e^{-im_k\phi}$ as $\psi_k(r,\theta,\phi) = \Psi_k(r,\theta)e^{-im_k\phi}$. The integral over the azimuthal variable ϕ is nonzero only if the relation $m_c = m_s + m_\Omega$ is fulfilled. This condition, known as phase matching or angular momentum conservation, returns a real value of the coupling constant g presented in Eq. (4).

We can linearize the Hamiltonian in Eq. (3) by limiting our analysis to the case where the center mode of the optical cavity is pumped resonantly by a strong coherent field at frequency $\omega_p = \omega_c$. In this condition the optical mode $\hat{a}_c$ can be treated as classical complex number $a_p = \langle\hat{a}_c\rangle$ and the linearized Hamiltonian becomes

$$\hat{H} = \hbar a_p g(\hat{a}_o\hat{a}_\Omega + \hat{a}_\Omega^\dagger\hat{a}_o^\dagger). \tag{5}$$

Here for simplicity we renamed the optical mode $\hat{a}_s \to \hat{a}_o$. The above Hamiltonian describes a parametric downconversion process that is responsible for entangling the microwave mode Ω with the optical mode ω_o. In a lossless system, this interaction could lead to an exponential growth of the energy stored in both modes and consequently lead to photon amplification of each mode.

Device implementation

The proposed system is based on a 3D-microwave cavity enclosing a mm-sized $LiNbO_3$ WGM resonator with major radius R operating at millikelvin temperature. At optical wavelengths, these mechanically polished resonators offer material-limited internal quality factors $Q_{i,o} \gtrsim 3.3\times10^8$[46] and strong lateral confinement, reflected in the small optical mode cross-section $\Psi_k(r,\theta)$, on the order of tens of μm^2.[47] In the microwave regime, $LiNbO_3$ exhibits an internal quality factor $Q_{i,\Omega} \gtrsim 10^4$ in the X-band at millikelvin temperatures[48] and a high electro-optic coefficiet $r_{33} = 31$ pm/V at 9 GHz.[49,50]

The large wavelength $\lambda_\Omega \gtrsim R$ of the microwave field causes considerable reduction of the spatial optical-microwave mode overlap, leading to a small microwave-optical mode coupling g. The proposed system tackles this problem by coupling the optical resonator to a metallic cavity. This hybrid device involves a monolithic $LiNbO_3$ resonator clamped at the center of a microwave cavity by two thin rods machined for example from aluminum or copper as depicted in Fig. 2a. The $LiNbO_3$ resonator is coated with a thin-film of superconductor such as Al or NbTiN forming the upper and lower electrodes of a capacitor for the microwave cavity. The thin-film electrodes can be realized by evaporating metal on the full resonator's surface followed by optical lithography on the resonator's rim. The photoresist is developed and the unprotected thin metal band is etched. An interesting feature of this resonator fabrication process is the possibility to vary the gap size d between the upper and lower electrodes independent of the disk thickness. Gaps from 1 mm down to 10 µm are feasible by adjusting the focus of the lithography laser. This results in a strong confinement of the microwave electric field at the resonator's wedge-shaped rim, enhancing the mode overlap between the optical and microwave

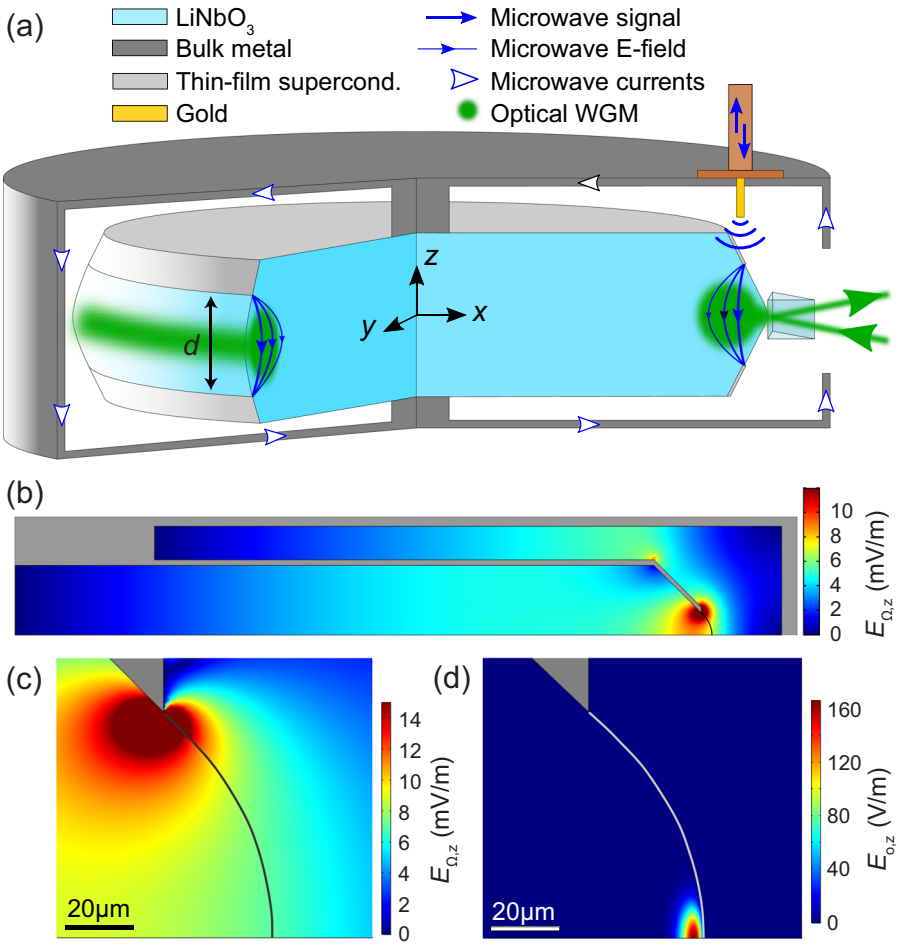

Fig. 2 Device implementation of the proposed cavity electro-optic modulator. **a** A monolithic $LiNbO_3$ optical resonator is incorporated inside a metal microwave cavity. The optical resonator is coated with a thin-film superconductor that defines the capacitor gap d and confines the microwave electric field at the resonator's rim. **b** To scale: microwave single photon electric field distribution $E_{\Omega,z}$ along the z axis. Only a quarter of the resonator is shown for symmetry reasons. **c** Enlarged view of the electric field distribution $E_{\Omega,z}$ at the resonator's rim. **d** Enlarged view of the electric field distribution of the optical mode $E_{o,z}$ along the z direction.

mode as shown in Fig. 2b–d, and increasing the coupling constant g (see Eq. (4). In addition, the enclosing cavity offers a degree of freedom to control the microwave mode's spatial distribution $\psi_\Omega(\vec{r})$, the microwave resonance frequency Ω and its coupling to a microwave coaxial waveguide $\kappa_{e,\Omega}$.

To achieve optical-microwave mode interaction the energy and azimuthal momentum conservations must be fulfilled. For this system, we use and isolate two neighboring optical modes with angular number $m_s = m$ and $m_c = m + 1$, spectrally separated by a FSR as experimentally shown in ref. [42] The energy conservation is fulfilled by matching the microwave mode frequency Ω to the optical FSR. In addition, the microwave mode field distribution must have one oscillation around the resonator's rim ($m = 1$) to fulfill the angular momentum conservation. We assume the center frequency of the WGM resonator with mode number $m_c = m + 1$ is coherently pumped via the evanescant coupling with a dielectric prism, which also serves as the out-coupling port for the created Stokes-sideband with mode number $m_s = m$. On the microwave side, a pin coupler can be used to couple the microwave photons into a coaxial waveguide as depicted in Fig. 2a. Here, the WGM resonator has an optical FSR of 9 GHz, corresponding to the typical frequency range of superconducting qubits and read-out resonators.

Numerical analysis of the system

Figure 2c, d show the numerical simulation of the electric field distribution of the microwave and optical modes, respectively. The microwave electric field is constant in the region enclosing the optical field. We simulate a z-cut $LiNbO_3$ WGM resonator with major radius $R = 2.5$ mm, height $H = 0.5$ mm, and side curvature $R_c = 0.1$ mm, enclosed by a cylindrical microwave cavity with diameter 5.5 and 1.3 mm hight. The optical WGM cross-section (FWHM) is analytically calculated to be $7.6 \times 17.8\,\mu m^2$.[47] For the electric fields along the $\hat{z}$ direction, the integral term in Eq. (4) results in:[42]

$$g = \frac{1}{4\sqrt{2}} \cdot n_e^2 \cdot \omega_p \cdot r_{33} \cdot E_{\Omega,z}(\vec{r_o}), \tag{6}$$

where n_e is the extraordinary optical refractive index of $LiNbO_3$ and $E_{\Omega,z}(\vec{r_o})$ is the z-component of the single photon microwave electric field at the position $\vec{r_o}$ of the optical mode. The $1/\sqrt{2}$ correction term is owing to the nature of the microwave stationary wave, which can be seen as two contra-propagating waves, one of which propagates opposite to the optical mode and therefore does not interact with it.

Figure 3a shows the simulated microwave-optical coupling rate g as a function of the electrodes gap size d. From a parametric fit to the simulated values, we find the dependency of coupling rate

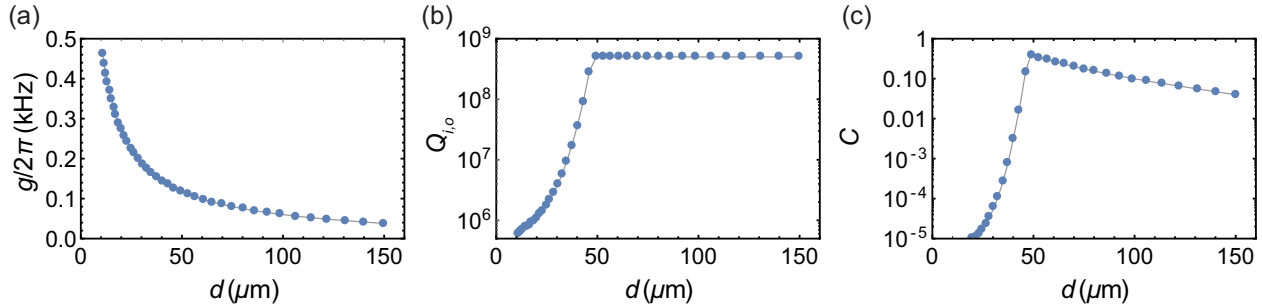

Fig. 3 Simulated device parameters as a function of the gap size d between the two thin-film metal electrodes. **a** The microwave-optical coupling rate g, **b** the intrinsic optical quality factor $Q_{i,o}$, and **c** the multi-photon cooperativity C for $P_p = 10\ \mu W$ as function of the electrodes gap size d at 10 mK.

Table 1. Electro-optic device parameter.

$\Omega/2\pi$	$\omega_o/2\pi$	$g/2\pi$	$Q_{i,\Omega}$	$Q_{i,o}$	η_Ω	η_o
9 GHz	193.5 THz	119 Hz	3×10^3	5×10^3	0.8	0.5

For generality, we chose an asymmetric coupling situation $\kappa_\Omega > \kappa_o$ and $\eta_\Omega > \eta_o$. The necessary pump power to achieve $C = 1$ in this asymmetrically and over-coupled configuration is $P_{p,C=1} = 63.9\ \mu W$
Reference values for the proposed system based on simulation (Ω, ω_o, and g) and characterization measurements of the system ($Q_{i,\Omega}$ and $Q_{i,o}$)

g to the gap size d scales with $g \sim d^{-0.8}$. Figure 3b shows the internal quality factor of the optical resonator $Q_{i,o}$ versus the gap size d. By decreasing the gap size, $Q_{i,o}$ decreases exponentially because the optical mode has a Gaussian envelope $\Psi_k \sim \exp(-0.5 \cdot z^2/\sigma_z^2)$ with $\sigma_z = 7.6\ \mu m$ along the $\hat{z}$ axis. For this simulation we consider aluminum electrodes, which exhibit a large imaginary index at optical frequencies[51,52] and therefore impose an optical loss for small electrode distances. In addition, optical photons can break the cooper pairs in the superconducting electrodes, degrading the quality factor of the microwave cavity. Therefore, it is desirable to reduce the spatial overlap between the optical mode and the superconducting electrodes and reduce the optical surface scattering. For moderately sized gaps the optical quality factor reaches the limit of $Q_{i,o} \sim 5\times10^8$, which is backed by our experimental results at room temperature without the metal electrodes and expected to be the material-limited absorption of $LiNbO_3$.

We have also carried out characterization measurements of the microwave properties of the proposed system shown in Fig. 2 using an aluminum cavity and thin-film aluminum metallization, which yielded values $Q_{i,\Omega} \sim 3\times10^3$ for a clamping rod diameter of 0.5 mm. This value, which we use for our further modeling, is at least a factor 4 below the reported material limit of $LiNbO_3$ and we attribute this to other loss sources such as frequency-dependent defect states,[48] piezoelectric mechanical,[53] cavity seam,[54] and surface losses.[55]

The multi-photon cooperativity $C = \frac{4n_p g^2}{\kappa_o \kappa_\Omega} = \frac{4\eta_o}{\kappa_o}\frac{P_p}{\hbar\omega_p}$ is the figure of merit in electro-optic systems. Here, $n_p = |\alpha_p|^2$ is the intra-cavity photon number owing to the resonant optical pump power P_p, $\kappa_{\Omega(o)} = \kappa_{e,\Omega(o)} + \kappa_{i,\Omega(o)}$ is total loss of the microwave (optical) cavity, whereas $\kappa_{e,\Omega(o)}$ and $\kappa_{i,\Omega(o)}$ are the extrinsic and the intrinsic damping rates of the microwave (optical) cavity, respectively. Here, we defined the normalized cavity to waveguide coupling strength as $\eta_{\Omega(o)} = \kappa_{e,\Omega(o)}/\kappa_{\Omega(o)}$ of the microwave (optical) resonator. Under the critically coupled condition $\eta_\Omega = \eta_o = 1/2$, the cooperativity for a given pump power is given as

$$C = \frac{P_p g^2 Q_{i,o}^2 Q_{i,\Omega}}{\hbar\omega_p^3 \Omega}, \tag{7}$$

with the intrinsic quality factor $Q_{i,\Omega(o)} = \Omega(\omega_o)/\kappa_{i,\Omega(\omega_o)}$ of the microwave (optical) mode. In Fig. 3c, we plot the microwave-optical cooperativity C as a function of the electrode gap size d and for a fixed optical pump power of 10 μW. This plot shows that the cooperativity increases by decreasing the gap size and it reaches its maximum value at $d \sim 50\ \mu m$ where $Q_{i,o}$ starts to saturate due to material absorption. To reach strong multi-photon microwave-optical interaction requires a cooperativity close to 1, which can be achieved by increasing the optical pump power to $P_p = 25.4\ \mu W$.

It is important to note that this is lower than the cooling power of commercial cryostats at ~30 mK and that in practice only a small fraction of it would be dissipated into the cold stage of the dilution refrigerator, whereas the majority of the pump field is out-coupled together with the generated signal via an optical fiber, e.g., by using a diamond prism with a basis angle of 63.5°. Nevertheless, in the following we will also consider the situation where the EO modulator is operated at the still plate at 800 mK and connected to a cold superconducting circuit at a few mK via a low-loss superconducting waveguide. The still stage of a modern dilution refrigerator offers cooling powers of at least 20 mW and the higher temperature offers higher thermal conductivities to connect the modulator more efficiently to the cold bath. Table 1 summarizes the full set of system parameters that will be used in the following unless otherwise stated.

System dynamics

In this subsection, we study the quantum dynamics of the proposed electro-optic modulator system presented in the previous section. We specifically focus on the conditions under which one can efficiently correlate and entangle optical and microwave fields using electro-optic interaction. The dynamics of the system can be fully described using the quantum Langevin treatment in which we add the damping and noise terms to the Heisenberg equations for the system operators associated with Eq. (5). The resulting quantum Langevin equations for the intra-cavity optical and microwave modes are

$$\dot{\hat{a}}_\Omega = -iG\hat{a}_o^\dagger - \frac{\kappa_\Omega}{2}\hat{a}_\Omega + \sqrt{\kappa_{e,\Omega}}\hat{a}_{e,\Omega} + \sqrt{\kappa_{i,\Omega}}\hat{a}_{i,\Omega} \tag{8a}$$

$$\dot{\hat{a}}_o = -iG\hat{a}_\Omega^\dagger - \frac{\kappa_o}{2}\hat{a}_o + \sqrt{\kappa_{e,o}}\hat{a}_{e,o} + \sqrt{\kappa_{i,o}}\hat{a}_{i,o}, \tag{8b}$$

where $G = \sqrt{n_p}ge^{i\phi_p}$ is the multi-photon interaction rate and ϕ_p the phase of the pump. We also introduce the zero-mean microwave (optical) input noises given by $\hat{a}_{e,\Omega(o)}$ and $\hat{a}_{i,\Omega(o)}$, obeying the following correlation functions

$$\langle \hat{a}_{k,\Omega(o)}^\dagger(t)\hat{a}_{k,\Omega(o)}(t')\rangle = \bar{n}_{\Omega(o)}^k \delta(t-t') \tag{9a}$$

$$\langle \hat{a}_{k,\Omega(o)}(t)\hat{a}_{k,\Omega(o)}^\dagger(t')\rangle = (\bar{n}_{\Omega(o)}^k + 1)\delta(t-t'), \tag{9b}$$

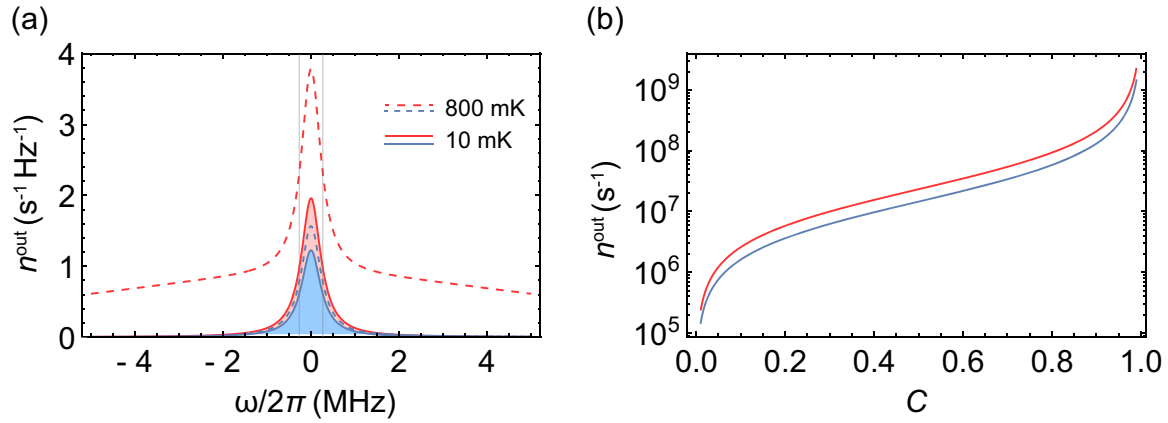

Fig. 4 Output photon numbers of the microwave and optical resonator. **a** Output photon number spectral density at two bath temperatures $T_b = 10$ mK (solid lines) and $T_b = 800$ mK (dashed lines) of the microwave (blue) and optical resonator (red) for the values given in Table 1 and $C = 0.3$. **b** Total integrated output photon flux of the optical resonator (blue) and microwave cavity (red) with respect to the pump power-dependent cooperativity C at $T_b = 10$ mK.

with $k = e, i$ where $\overline{n}^{e}_{\Omega(o)}$ and $\overline{n}^{i}_{\Omega(o)}$ are the equilibrium mean thermal photon numbers of the microwave (optical) fields.

The Eqs. (8a) and (8b) describe the dynamics of the system and reveal the origin of the optical-microwave intra-cavity correlation, which arises from the cross dependency of microwave operator $\hat{a}_\Omega$ on the optical mode operator $\hat{a}_o$, and vice versa. However, in this paper we are interested in generating nonclassical correlation and entanglement between itinerant electromagnetic modes, which can be calculated using the standard input–output theory.[56] We first solve the Eqs. (8a) and (8b) by moving to the Fourier domain to obtain the microwave and optical resonator variables. Then, substituting the solutions of Eqs. (8a) and (8b) into the corresponding input–output formula for the cavities' variables, i.e., $\hat{a}^{out}_{\Omega(o)} = \sqrt{\kappa_{e,\Omega(o)}}\hat{a}_{\Omega(o)} - \hat{a}_{e,\Omega(o)}$, we obtain

$$\hat{S}^{out}(\omega) = D(\omega)\cdot\hat{S}^{in}(\omega) \tag{10}$$

where $\hat{S}^{out}(\omega) = [a^{out}_o(\omega), a^{out\dagger}_\Omega(-\omega)]^T$ is the output field matrix. The transformation matrix $D(\omega)$ is given by:[34]

$$D(\omega) = M(\omega)^{-1}\begin{bmatrix} (i\omega+\frac{\Delta\kappa_o}{2})(-i\omega+\frac{\kappa_\Omega}{2})+|G|^2 & \sqrt{\kappa_{e,o}\kappa_{i,o}}(-i\omega+\frac{\kappa_\Omega}{2}) & -iG\sqrt{\kappa_{e,o}\kappa_{e,\Omega}} & -iG\sqrt{\kappa_{e,o}\kappa_{i,\Omega}} \\ iG^*\sqrt{\kappa_{e,\Omega}\kappa_{e,o}} & iG^*\sqrt{\kappa_{e,\Omega}\kappa_{i,o}} & (i\omega+\frac{\Delta\kappa_\Omega}{2})(-i\omega+\frac{\kappa_o}{2})+|G|^2 & \sqrt{\kappa_{e,\Omega}\kappa_{i,\Omega}}(-i\omega+\frac{\kappa_o}{2}) \end{bmatrix}, \tag{11}$$

with $M(\omega) = (-i\omega+\kappa_o/2)(-i\omega+\kappa_\Omega/2) - |G|^2$, $\Delta\kappa_{\{o,\Omega\}} = \kappa_{e,\{o,\Omega\}} - \kappa_{i,\{o,\Omega\}}$ and $\hat{S}^{in}(\omega)$ is the input noise matrix $[\hat{a}_{e,o}, \hat{a}_{i,o}, \hat{a}^\dagger_{e,\Omega}, \hat{a}^\dagger_{i,\Omega}]^T$. The photon generation rate of the traveling output fields of the electro-optic modulator owing to parametric downconversion $n^{out} = \langle a^{out\dagger}_j(\omega)a^{out}_j(\omega)\rangle$ can be calculated using Eq. (10)

$$n^{out} = \frac{4C\eta_j}{(1-C-\frac{4\omega^2}{\kappa_o\kappa_\Omega})^2 + \frac{4\omega^2}{\kappa_o^2\kappa_\Omega^2}(\kappa_o+\kappa_\Omega)^2}. \tag{12}$$

The bandwidth of the emitted radiation is

$$\mathrm{BW} = \sqrt{-C - \frac{\kappa_o^2+\kappa_\Omega^2}{2\kappa_o\kappa_\Omega} + \sqrt{(1-C)^2 + \left(C + \frac{\kappa_o^2+\kappa_\Omega^2}{2\kappa_o\kappa_\Omega}\right)^2}} \times \sqrt{\kappa_o\kappa_\Omega}, \tag{13}$$

which decreases as a function of C and approaches zero for $C = 1$.

In Fig. 4a, we show the output spectra of the microwave and optical cavities with respect to the response frequency ω for the experimentally accessible parameters shown in Table 1 at a cooperativity $C = 0.3$ corresponding to a pump power of $P_p = 19.2\,\mu W$. Even for such low pump powers we obtain readily detectable signal output powers on the order of 1 photon per second per Hertz. Owing to the asymmetric waveguide-cavity/resonator coupling $\eta_o \neq \eta_\Omega$, the output photon numbers are not balanced but it is worth noting that the bandwidth is identical even though the dissipation rates κ_Ω and κ_o are very different. The output spectra at an elevated temperature of the cavity baths $T_b = 800$ mK is related to the thermal photon numbers $\overline{n}^{i}_{\Omega(o)} = (\exp(\hbar\Omega(o)/k_BT_b) - 1)^{-1}$. Here, we assume a cold waveguide $\overline{n}^{e}_{\Omega(o)} \sim 0$, which can be realized with superconducting cables connected to the base temperature of the cryostat. As expected, the output of the microwave cavity increases considerably owing to an increase of the modulator thermal noise $\overline{n}^{i}_{\Omega}$. Although the photon occupation of the optical mode $\overline{n}^{i}_{o}$ is negligible one can see that the thermal microwave noise leads to parametrically amplified optical noise at the resonator output at elevated temperatures.

Figure 4b shows the integrated optical and microwave output photon flux versus multi-photon cooperativity C. The photon numbers are increasing with C and diverge abruptly as the cooperativity approaches unity $C \to 1$. In this limit the system reaches its instability and the linearization approximation used in the Hamiltonian Eq. (5) is not valid anymore. Therefore, for the remainder of the paper we study the generation of microwave-optics entanglement, conversion and quantum state transfer in the parameter range $C < 1$.

Two-mode squeezing

First, we verify the generation of the two-mode squeezing at the outputs of the microwave cavity and optical resonator. For this reason, it is convenient to define the field quadratures in terms of the annihilation and creation operators

$$\hat{q}_k = \hat{X}_k(0) \quad \text{and} \quad \hat{p}_k = \hat{X}_k(\pi/2), \qquad k = o, \Omega \tag{14}$$

where

$$\hat{X}_k(\theta) = \frac{1}{\sqrt{2}}(\hat{A}^{out}_k e^{-i\theta} + \hat{A}^{out\dagger}_k e^{i\theta}). \tag{15}$$

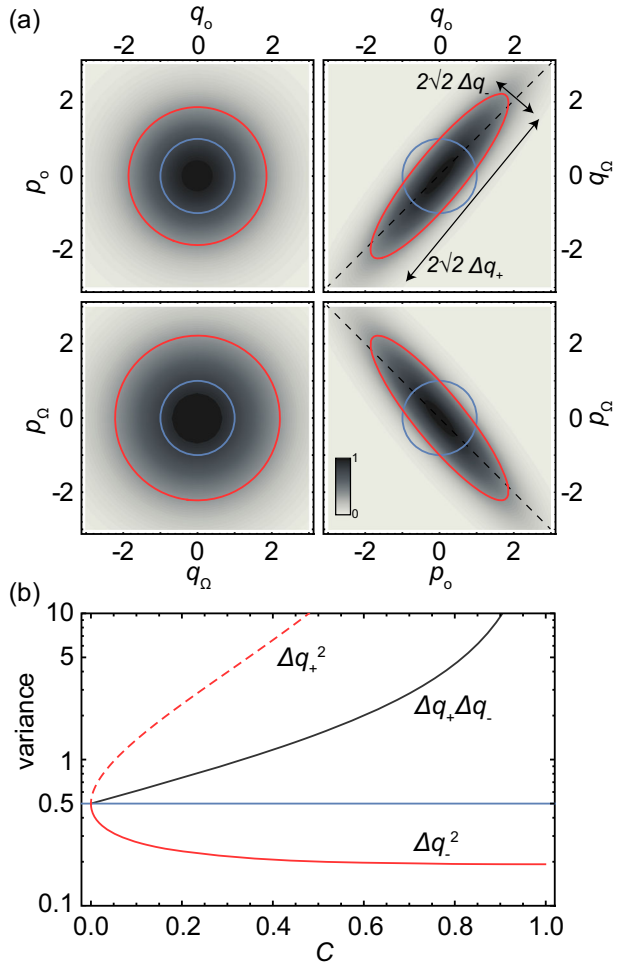

Fig. 5 Two-mode squeezing of the electro-optic output fields. **a** Normalized projections of the Wigner function of four output quadrature pairs for the same parameters as in Fig. 4a. The solid red line (blue line) indicates a drop by e^{-1} of its (the vacuum state's) maximum. The black dashed line marks the squeezing angle of 45° for an ideal squeezer. The squeezing angles for the asymmetric system in this representation are given by $\pm(90^\circ - \Theta)$. **b** The squeezed and anti-squeezed quadrature varince Δq_-^2 (solid red line), Δq_+^2 (dashed red line), their product $\Delta q_-\Delta q_+$ (black line) and the variance of the vacuum (blue line) as a function of the cooperativity C for the same parameters.

These quadratures satisfy the bosonic commutator $[\hat{q}_k, \hat{p}_k] = i$ and we define the filtered output operators

$$\hat{A}_k^{\text{out}}(\sigma) = \int_{-\infty}^{\infty} d\omega\, \mathrm{f}_k(\omega, \sigma_k)\hat{a}_k^{\text{out}}(\omega), \tag{16}$$

where we assume the filter function $\mathrm{f}_k(\omega, \sigma)$ with bandwidth σ_k ($k = o, \Omega$) is acting on the output of each cavity. Note that the vacuum noise is 1/2 for the quadratures defined in Eq. (14).

In order to quantify entanglement, we first determine the covariance matrix (CM) of our system, which can be expressed as[13]

$$V_{jk} = \frac{1}{2}\langle \Delta\hat{\mathrm{x}}_j \Delta\hat{\mathrm{x}}_k + \Delta\hat{\mathrm{x}}_k \Delta\hat{\mathrm{x}}_j \rangle, \tag{17}$$

where $\Delta\hat{\mathrm{x}}_k = \hat{\mathrm{x}}_k - \langle\hat{\mathrm{x}}_k\rangle$ and $\hat{\mathbf{x}} = [\hat{q}_o, \hat{p}_o, \hat{q}_\Omega, \hat{p}_\Omega]^{\mathrm{T}}$. Using the scattering matrix defined in Eq. (10) to calculate the second order moments of the output quadratures Eq. (15) at zero bandwidth $\sigma = 0$, we can compute the CM of the system in the steady state

$$V = \begin{bmatrix} \left(0.5 + \frac{4C(1+\bar{n}_\Omega)\eta_o}{(1-C)^2}\right) I & \left(\sqrt{4\eta_o\eta_\Omega C}\frac{(1+C+2\bar{n}_\Omega)}{(1-C)^2}\right) Z \\ \left(\sqrt{4\eta_o\eta_\Omega C}\frac{(1+C+2\bar{n}_\Omega)}{(1-C)^2}\right) Z & \left(0.5 + \frac{4(C+\bar{n}_\Omega)\eta_\Omega}{(1-C)^2}\right) I \end{bmatrix}, \tag{18}$$

where $\boldsymbol{I}_{2\times 2}$ is the identity matrix, $Z = \mathrm{diag}(1, -1)$ and $\bar{n}_\Omega = \kappa_{i,\Omega}\bar{n}_\Omega^i(T_b)/\kappa_\Omega$ is the microwave thermal mode occupancy. Here we assume a cold waveguide $\bar{n}_{\Omega(o)}^e = 0$ as well as $\bar{n}_o^i = 0$. For $C = 0$ the CM Eq. (18) takes on the values of the vacuum noise $V = I_{4\times 4}/2$ and the CM diverges at $C = 1$.

The existence of microwave-optical entanglement can be demonstrated using the quasi-probability Wigner function, which can be written in terms of the CM Eq. (18) and the optical and mic rowave quadratures $\hat{q}_k$ and $\hat{p}_k$

$$W(x) = \frac{\exp(-\frac{1}{2}[x \cdot V^{-1} \cdot x)]}{\pi^2\sqrt{\det[V]}}. \tag{19}$$

Figure 5a shows the Wigner function projected into the 4 different quadratures subspaces $\{p_o, q_o\}$, $\{p_\Omega, q_\Omega\}$, $\{q_\Omega, q_o\}$, and $\{p_\Omega, p_o\}$ where the complementary variables are integrated. For reference, we also plot the Wigner function of the vacuum state $V = I_{4\times 4}/2$ (blue circle) corresponding to zero cooperativity $C = 0$. The single-mode projections $\{p_o, q_o\}$ and $\{p_\Omega, q_\Omega\}$ show an increase of the noise fluctuations, indicating the phase-independent amplification of the vacuum noise at the output of each cavity. The $\{q_\Omega, q_o\}$ and $\{p_\Omega, p_o\}$ projections on the other hand, demonstrate the microwave-optical cross-correlation, originating from the electro-optic interaction, whose fluctuations in specific direction are squeezed below the quantum limit (blue line) and anti-squeezed in the perpendicular direction. In this plot, the red (blue) line indicates a drop by e^{-1} of its maximum for the parameters $C = 0.3$ ($C = 0$) at $T_b = 0$. Unlike the ideal symmetric two-mode squeezer ($V_{11} = V_{22} = V_{33} = V_{44}$) whose quadrature squeezing appears along diagonal axes with squeezing angle ±45° (black dashed lines), in general the electro-optic system is an asymmetric squeezer ($V_{11} = V_{22} \neq V_{33} = V_{44}$) if $\eta_o \neq \eta_\Omega$. The squeezing angle is then given by $\tan(2\Theta) = \pm 2V_{13}/|V_{33} - V_{11}|$ and its value is 39.34° for the system's parameters in Fig. 5a.

In Fig. 5b, we show the squeezed Δq_-^2 and anti-squeezing Δq_+^2 quadrature variances as well as their product $\Delta q_-\Delta q_+$, which is related to the purity $\mathcal{P} = 1/(2\Delta q_-\Delta q_+)$ of Gaussian states,[57] as a function of the cooperativity C. The variances are given as

$$\Delta q_\mp = \sqrt{\frac{(8C\eta_o + \varepsilon)(8C\eta_\Omega + \varepsilon)/\varepsilon - \Upsilon^2/\varepsilon}{2[\varepsilon + 8C\left(\eta_{o,(\Omega)}\sin^2(\Theta) + \eta_{\Omega,(o)}\cos^2(\Theta)\right) \pm \Upsilon\sin(2\Theta)]}}, \tag{20}$$

with $\Upsilon = 4\sqrt{\eta_o\eta_\Omega C}(1 + C)$ and $\varepsilon = (1 - C)^2$. Larger C gives smaller Δq_- (more squeezing) and larger Δq_+ (more amplification) at the outputs of the cavities. In the ideal case $\eta_o = \eta_\Omega = 1$ and for $0 < C < 1$ the above equation reduces to

$$\Delta q_-^2 = \frac{1}{2}\left(\frac{1 - \sqrt{C}}{1 + \sqrt{C}}\right)^2 < \frac{1}{2}, \tag{21a}$$

$$\Delta q_+^2 = \frac{1}{2}\left(\frac{1 + \sqrt{C}}{1 - \sqrt{C}}\right)^2 > \frac{1}{2}, \tag{21b}$$

which satisfies the minimum quadrature uncertainty $\Delta q_-\Delta q_+ = 1/2$. Moreover, we can define the electro-optic squeezing parameter as $r_{\text{EO}} = \ln\left(\frac{1+\sqrt{C}}{1-\sqrt{C}}\right)$ for this configuration. Owing to the optical and microwave internal losses $\eta_k < 1$ ($k = o, \Omega$) the quadrature variances deviate from the uncertainty principle $\Delta q_-\Delta q_+ > 1/2$ in the proposed device as shown in Fig. 5b.

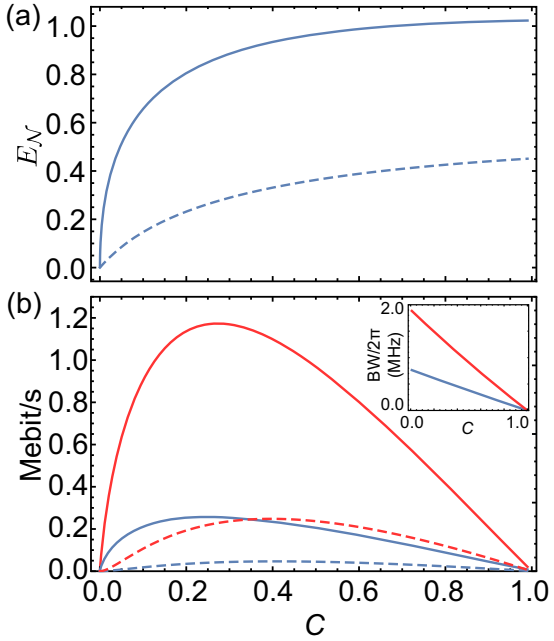

Fig. 6 Entanglement and bandwidth of the electro-optic output fields. **a** Microwave-optical entanglement given by the logarithmic negativity $\bar{E}_{\mathcal{N}}$ versus cooperativity C at $T_b = 10$ mK (solid line) and $T_b = 800$ mK (dashed line) calculated over a bandiwdth (BW). **b** The average distribution of emitted entangled bits per second at $T_b = 10$ mK (solid lines) and $T_b = 800$ mK (dashed lines) as a function of cooperativity C for the parameters in Table 1 (blue lines) and stronger optical waveguide coupling, i.e. $\eta_\Omega = \eta_o = 0.8$ (red lines). The inset shows the corresponding photon generation bandwidth BW for $\eta_o = 0.5$ (blue line) and $\eta_o = 0.8$ (red line).

Microwave-optical entanglement

We are interested in the entanglement properties of the radiation leaving the system and we therefore study the bipartite microwave-optical entanglement, which can be quantified using the logarithmic negativity[58,59]

$$E_{\mathcal{N}} = \max[0, -\log_2(2\tilde{d}_-)]. \tag{22}$$

where

$$\tilde{d}_- = 2^{-1/2}\sqrt{\tilde{\Delta} - \sqrt{\tilde{\Delta}^2 - 4\det(V)}}, \tag{23}$$

is the smallest symplectic eigenvalue of the partial transpose of the CM Eq. (18) with $\tilde{\Delta} = V_{11}^2 + V_{33}^2 + 2V_{13}^2$. In Fig. 6a we plot $E_{\mathcal{N}}$ as a function of the cooperativity for two different temperatures 10 mK (solid line) and 800 mK (dashed line). One can see that a significant amount of microwave-optical entanglement is generated $E_{\mathcal{N}} \sim 1$, even for moderate values of C, increasing with higher cooperativity and decreasing significantly at elevated bath temperatures T_b. In the low temperature limit $\bar{n}_\Omega \simeq 0$ and for the waveguide coupling matching $\eta = \eta_o = \eta_\Omega$, the logarithmic negativity (17) reduces to

$$E_{\mathcal{N}} = -\log_2\left(1 - \frac{4\eta\sqrt{C}}{(1+\sqrt{C})^2}\right). \tag{24}$$

We also calculate the distribution rate of the entangled fields emitted from the electro-optic system, which is given by

$$\#(\text{ebit/s}) = \bar{E}_F \cdot \text{BW}/2\pi. \tag{25}$$

where we introduce the entanglement of formation

$$E_F(\rho) = (x_m + 0.5)\log_2(x_m + 0.5) - (x_m - 0.5)\log_2(x_m - 0.5) \tag{26}$$

with $x_m = (\tilde{d}_-^2 + 1/4)/(2\tilde{d}_-)$. From the obtained output operators in Eq. (16) with the rectangular filter $\mathrm{f}_k(\omega,\sigma) = H(\text{BW}/2 - |\omega|)/\sqrt{\text{BW}}$, we compute the average CM over the emission bandwidth, which is then used inside Eq. (26) returning the average entanglement of formation $\bar{E}_F$.

Figure 6b shows the total emission rate of entangled radiation as well as the bandwidth of the photon emission as a function of cooperativity C. For the considered system parameters given in Table 1 (blue solid line) a maximum value of 0.26 Mebit/s is reached at $C = 0.25$ with a photon emission bandwidth of 0.6 MHz at $\mathrm{P}_p = 16\,\mu$W. The most-effective method to increase the BW and entanglement rate is to increase the optical waveguide coupling $\kappa_{e,o}$. The red lines in Fig. 6b show the situation for $\eta_o = 0.8$, yielding rates of 1.17 Mebit/s at ~1.34 MHz bandwidth at $C = 0.27$, which would now require a pump power of ($\mathrm{P}_p = 68\,\mu$W, a value that is still feasible at the mixing chamber temperature stage of a dilution refrigerator. Coherent quantum information I quantifies the lower bound of the distillable entanglement. $I_\Omega = I_o = 0.24$ Mebit/s is maximal at $C = 0.27$ and calculated according to refs [13,60] at low temperature in the symmetric case.

At the significantly elevated bath temperatures of $T_b = 800$ mK (dashed lines) the maximum entanglement rates drop by about a factor 5 in both coupling situations. It should be noted that further increasing the coupling to a cold waveguide on the microwave side $\eta_\Omega \simeq 1$ or alternatively finding a way to lower the internal losses of the microwave mode, would result in a significantly smaller effective system temperature. Larger waveguide coupling strengths and higher available pump powers at the still stage of a dilution refrigerator together with higher thermal conductivities could result in significantly higher entanglement rates than discussed in this paper which focusses on currently accessible device parameters. In all cases the entanglement rate approaches zero at $C = 1$, following the decrease in photon emission bandwidth, see also Eq. (13).

Teleportation-based quantum state transfer

An important feature of a hybrid quantum network is the ability to transfer quantum states between different nodes. The quality of the state transfer is characterized by the fidelity[61]

$$F = \pi \int W_{\text{in}}(\beta) W_{\text{out}}(\beta) \mathrm{d}^2\beta, \tag{27}$$

where W_{in} and W_{out} are the initial and final Wigner functions of an unknown arbitrary quantum state before and after the transduction, respectively. For Gaussian states the fidelity simplifies to[62]

$$F = \frac{\exp[-(\mathbf{x}^{\text{out}} - \mathbf{x}^{\text{in}})^{\mathrm{T}} \cdot \mathbf{V}_{\mathrm{F}}^{-1} \cdot (\mathbf{x}^{\text{out}} - \mathbf{x}^{\text{in}})]}{\sqrt{\det(\mathbf{V}_{\mathrm{F}}/2)}} \tag{28}$$

with $\mathbf{x}^{\text{in}} = (q_{o(\Omega)}^{\text{in}}, p_{o(\Omega)}^{\text{in}})^{\mathrm{T}}$, $\mathbf{x}^{\text{out}} = (q_{o(\Omega)}^{\text{out}}, p_{o(\Omega)}^{\text{out}})^{\mathrm{T}}$ and $\mathbf{V}_{\mathrm{F}} = 2\mathbf{V}_{\text{in}} + 2\mathbf{V}_{\text{out}}$, where $\mathbf{V}_{\text{in,(out)}}$ are the input and output covariance matrices following the definition given in Eq. (17).

We propose the bidirectional microwave-to-optical quantum state transfer using the presented EO device as an EPR source in an unconditional CV teleportation scheme. Assuming the standard Braunstein–Kimble set-up[61,64] with ideal Bell measurements and classical information transfer as depicted in Fig. 7a, the state transfer fidelity for an unknown coherent squeezed state $|\psi_{\text{in}}\rangle = |\alpha, r\rangle$ is given by

$$F_{\text{TE}}^{\text{G}}(\alpha, r, C, \eta_o, \eta_\Omega) = \left(4\Delta q_-^4 + 2\Delta q_-^2 \cosh(2r) + 1\right)^{-1/2} \tag{29}$$

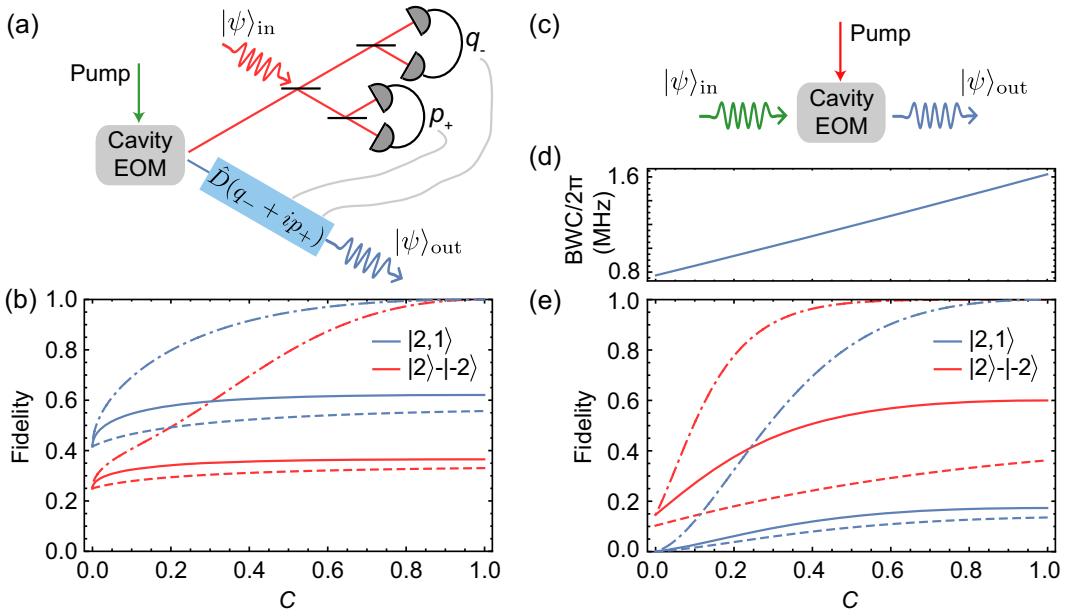

Fig. 7 Quantum state transfer. **a** EO teleportation scheme. The sender mixes the unknown optical input state $|\psi\rangle_{in}$ with one arm of the EO entanglement source using a 50:50 beam splitter and performs the corresponding Bell measurements of q_- and p_+. This information is sent classically to the microwave receiver, where an appropriate phase space displacement in the second arm of the EO entanglement source is performed to complete the state transfer. **b** Calculated fidelity of the teleportation protocol for the coherent squeezed input state $|\psi\rangle_{in} = |\alpha = 2, r = 1\rangle$ (blue lines) and for the cat state $|\psi\rangle_{in} = |2\rangle - |-2\rangle$ (red lines) for the experimental parameters outlined in Table 1 (solid lines), at an elevated temperature $T_b = 800$ mK (dashed lines) and for the case of a lossless system $\eta_\Omega = \eta_o = 1$ (dash-dotted lines). Note that the classical threshold for teleportation fidelity of a pure coherent state is 0.5, as shown in ref. [63]. **c** Scheme for EO transduction. The EO modulator is coherently pumped on resonance with the lower frequency optical mode,[42] allowing for coherent bidirectional conversion between the optical and the microwave modes. **d** Conversion bandwidth as a function of the multi-photon cooperativity C for the experimental parameters outlined in Table 1. **e** Calculated fidelity of the direct transducer protocol for the coherent squeezed input state $|\psi\rangle_{in} = |\alpha = 2, r = 1\rangle$ (blue lines) and for the cat state $|\psi\rangle_{in} = |2\rangle - |-2\rangle$ (red lines) for the experimental parameters outlined in Table 1 (solid lines), at an elevated temperature $T_b = 800$ mK (dashed lines) and for the case of a lossless system $\eta_\Omega = \eta_o = 1$ (dash-dotted lines).

with Δq_- explicitly given in Eq. (20). In the limit of $\eta_o = \eta_\Omega$ the fidelity for pure Gaussian states is reduced to:[65]

$$F_{TE}^{G}(\alpha, r, C, \eta) = \mathrm{Det}[2V_{in} + ZAZ + B - ZC - C^T Z^T]^{-1/2}, \tag{30}$$

where $A = V_{11} I$, $B = V_{33} I$, and $C = V_{13} Z$. The fidelity Eq. (30) can be written in terms of the logarithmic negativity $E_{\mathcal{N}}$ generated using the EO device

$$F_{TE}^{G}(\alpha, r, C) = \left(1 + 2^{1-E_{\mathcal{N}}(C)} \cosh(2r) + 2^{-2E_{\mathcal{N}}(C)}\right)^{-1/2}. \tag{31}$$

The fidelity in Eq. (31) is independent of the coherent state amplitude α due to the assumed ideal measurement of the quadratures q_- and p_+, and a lossless classical information transfer in this protocol. The bandwidth of the teleportation is given by the photon emission bandwidth shown in the inset of Fig. 6b.

In Fig. 7b, we show the fidelity for the coherent squeezed input state $|\psi_{in}\rangle = |\alpha, r\rangle = |2, 1\rangle$ as a function of the multi-photon cooperativity C for the system parameters in Table 1 at zero temperature (blue solid line), at 800 mK (blue dashed line) as well as for a lossless system $\eta_o = \eta_\Omega = 1$ (blue dash-dotted line). The lower bound of the fidelity is set by the classical limit $F_{TE}^{cl} = e^{-r}/(1 + e^{-2r})$[66] valid for non-entangled microwave and optical radiation. The fidelity increases monotonically achieving its maximum value set by the minimum quadrature squeezing of the entanglement source $\Delta q_-^2 = 0.5 - \frac{\eta_o \eta_\Omega}{\eta_o + \eta_\Omega}$ as shown in Fig. 7b. An increased temperature leads to a significant reduction of the achievable state transfer fidelity. A fidelity of ~1 is achieved for a cooperativity close to 1 in the near lossless and perfectly over-coupled case. In this case the system thermalizes with the cold waveguide independent of its internal bath temperature.

Quantum state teleportation based on EO entanglement can be used also with non-Gaussian states such as cat states that are readily available in superconducting circuits. Cat states are represented as a quantum superposition of two coherent states in the form $N(|\alpha\rangle + e^{i\phi}|-\alpha\rangle)$ with $N = \sqrt{2 + 2\exp(-2\alpha)\cos(\phi)}$. The state transfer fidelity using the proposed EO entanglement source is given by[61]

$$F_{TE}^{cat} = \frac{1}{1 + 2\Delta q_-^2} - \frac{1 + e^{-4|\alpha|^2} - e^{-4\frac{|\alpha|^2}{1+2\Delta q_-^2}} - e^{-8\frac{\Delta q_-^2 |\alpha|^2}{1+2\Delta q_-^2}}}{(2 + 4\Delta q_-^2)(1 + e^{-2|\alpha|^2}\cos(\phi))^2}. \tag{32}$$

In Fig. 7b, we show the teleportation fidelity of the cat state $|\psi_{in}\rangle = |\alpha\rangle - |-\alpha\rangle = |2\rangle - |-2\rangle$ as a function of C for the system parameters in Table 1 at zero temperature (red solid line), at 800 mK (red dashed line) as well as for a lossless system $\eta_o = \eta_\Omega = 1$ (red dash-dotted line) where we consider $\phi = \pi$. We find that the cat state transfer fidelities are lower compared with the coherent squeezed input state over the full range of parameters.

Conversion-based quantum state transfer

The EO system can also be used to directly convert the information between microwave and optical photons, schematically shown in Fig. 7c. This is achieved by driving the lower frequency optical mode in the same scheme as given in ref. [42,43] changing the nonlinear interaction Hamiltonian into the so called beam splitter Hamiltonian, allowing coherent frequency conversion between the microwave and optical modes following the

equations of motion:

$$\dot{\hat{a}}_\Omega = -iG\hat{a}_o - \frac{\kappa_\Omega}{2}\hat{a}_\Omega + \sqrt{\kappa_{e,\Omega}}\hat{a}_{e,\Omega} + \sqrt{\kappa_{i,\Omega}}\hat{a}_{i,\Omega}, \tag{33a}$$

$$\dot{\hat{a}}_o = -iG\hat{a}_\Omega - \frac{\kappa_o}{2}\hat{a}_o + \sqrt{\kappa_{e,o}}\hat{a}_{e,o} + \sqrt{\kappa_{i,o}}\hat{a}_{i,o}, \tag{33b}$$

Using the input–output theory to calculate the outputs of the optical and microwave modes, we can infer the photon conversion efficiency between the traveling microwave and optical fields[34]

$$\frac{\left\langle a^{\mathrm{out}\dagger}_{o(\Omega)}(\omega)a^{\mathrm{out}}_{o(\Omega)}(\omega)\right\rangle}{\left\langle a^{\dagger}_{e,\Omega(o)}(\omega)a_{e,\Omega(o)}(\omega)\right\rangle} = \frac{4C\eta_\Omega\eta_o}{\left(1+C-\frac{4\omega^2}{\kappa_o\kappa_\Omega}\right)^2+\frac{4\omega^2}{\kappa_o^2\kappa_\Omega^2}\left(\kappa_o+\kappa_\Omega\right)^2}, \tag{34}$$

over the bandwidth:[47]

$$\mathrm{BWC} = \sqrt{C-\frac{\kappa_o^2+\kappa_\Omega^2}{2\kappa_o\kappa_\Omega}+\sqrt{(1+C)^2+\left(C-\frac{\kappa_o^2+\kappa_\Omega^2}{2\kappa_o\kappa_\Omega}\right)^2}} \times \sqrt{\kappa_o\kappa_\Omega}. \tag{35}$$

The conversion bandwidth BWC increases with the cooperativity as shown in Fig. 7d and for the case of rate matching $\kappa_o = \kappa_\Omega = \kappa$ achieves the maximum value of $\sqrt{2}\kappa$ for $C = 1$. For the coherent squeezed state $|a, r\rangle$ the fidelity of the direct state transduction is given by

$$F^{\mathrm{G}}_{\mathrm{tr}}(a,r,C) = \frac{\exp\left(-2|a|^2(\epsilon_3-1)^2\left(\frac{\cos(\phi_a)}{V_-}+\frac{\sin(\phi_a)}{V_+}\right)\right)}{\sqrt{\frac{\epsilon_2}{2}(1-\epsilon_3^4)+\epsilon_3^4\left(1+\frac{\bar{n}_\Omega\left(\epsilon_2+\epsilon_2\epsilon_3^{-2}-2+\frac{\bar{n}_\Omega}{C\eta_o}\right)}{C\eta_o}\right)}}, \tag{36}$$

where

$$V_\pm = \left(1+\epsilon_3^2(e^{\pm 2r}-1+2\bar{n}_\Omega/(\eta_o C)\right), \tag{37}$$

$\epsilon_2 = 1+\cosh(2r)$, and $\epsilon_3 = \frac{\sqrt{4\eta_o\eta_\Omega C}}{(1+C)}$.

Figure 7e shows the fidelity of state transfer for the squeezed coherent input state $|\psi_{\mathrm{in}}\rangle = |2,1\rangle$ as a function of C for the system parameters in Table 1 at zero temperature (blue solid line), at 800 mK (blue dashed line) as well as for a lossless system $\eta_o = \eta_\Omega = 1$ (blue dash-dotted line). The lower bound of the fidelity ($C = 0$) is given by the overlap of the initial state and the vacuum state set by $\frac{2e^{-r-2|a|^2}}{1+e^{-2r}}$. In comparison with the teleportation scheme shown in Fig. 7b, the fidelity in direct transduction shown in Fig. 7e is significantly lower for this state. In general for direct conversion the fidelity is strongly dependent on the field amplitude $|a|$, which can be seen from the numerator of Eq. (36) in the case $\eta_{o(\Omega)}<1$. However, it is important to note that many quantum communication protocols work with $|a| \leq 1$,[14,67,68] a regime where both schemes offer more comparable fidelities.

The direct EO transducer can also be used to convert non-Gaussian cat states between microwave and optical fields. For a real a the fidelity of the conversion is

$$F^{\mathrm{cat}}_{\mathrm{tr}}(a,C) = \frac{1}{\epsilon_4(1+\epsilon_5)}\left[e^{\frac{-2a^2(1+\epsilon_3^2)^2}{1+\epsilon_5}}\left(e^{\frac{8a^2\epsilon_3}{1+\epsilon_5}}+1\right) + 2\cos(\phi)\left(e^{-\frac{2a^2(\epsilon_3^2+\epsilon_5)}{1+\epsilon_5}}+e^{-\frac{2a^2(1+\epsilon_3^2\epsilon_5)}{1+\epsilon_5}}\right) + \cos(2\phi)e^{\frac{-2a^2(\epsilon_5+\epsilon_3)^2}{\epsilon_5(1+\epsilon_5)}}+e^{\frac{-2a^2(\epsilon_3-\epsilon_5)^2}{\epsilon_5(1+\epsilon_5)}}\right] \tag{38}$$

with $\epsilon_4 = (1+\cos(\phi)e^{-2a^2})(1+\cos(\phi)e^{-2a^2\epsilon_3^2})$ and $\epsilon_5 = 1+\frac{8\eta_\Omega\bar{n}_\Omega}{(1+C)^2}$, and the lower bound of this fidelity given by $(1+\cos(\phi))/(e^{a^2}+e^{-a^2}\cos(\phi))$. In Fig. 7e we plot the conversion fidelity for the cat state $|\psi_{\mathrm{in}}\rangle = |2\rangle - |-2\rangle$ as a function of C for the system parameters in Table 1 at zero temperature (red solid line), at 800 mK (red dashed line) as well as for a lossless system $\eta_o = \eta_\Omega = 1$ (red dash-dotted line). We can compare the performance of the two working transduction schemes for the quantum state transfer in electro-optic devices in Fig. 7b, e. Although teleportation performs better for the coherent squeezed state both with and without waveguide coupling losses, for the cat state direct transduction performs better in a broad range $C > 0.2$ except for elevated temperatures. It should also be pointed out that the bandwidth of the state transfer is generally higher for direct conversion schemes BWC > BW as seen in Figs. 6b and 7d.

The most efficient electro-optic system yet reported achieved $C = 0.075$ with waveguide coupling rates $\eta_o = 0.31$ and $\eta_\Omega = 0.26$ at an effective temperature of 2.1 K.[43] Assuming that the waveguides can be thermalized to low mK temperatures, the fidelities for a state $|a = 2, r = 1\rangle$ are 10^{-3} and 0.41 for direct transduction and teleportation, respectively. On the other hand, the fidelity for an odd cat state with $a = 2$ are 0.09 and 0.25 for direct transduction and teleportation schemes, respectively. Our analysis showed that the proposed device should be able to outperform the state of the art with pump powers that are about 10^3 times lower—a crucial aspect to be able to thermalize the system noise temperature to the cold environmental bath.

DISCUSSION

We have presented an efficient and bright microwave-optical entanglement source based on a triply resonant electro-optic interaction. We proposed a specific device geometry and material system, tested and simulated the most important system parameters and derived the theory describing the physics, entanglement generation and device performance for both teleportation and conversion type quantum state transfer.

The figures of merit for a quantum interface are efficiency and added noise, which both affect the achievable state transfer fidelity. But for any realistic application with finite lifetime qubits, the transducer bandwidth determines whether it is of practical use for quantum interconnects. On-chip integrated devices with small mode volume offer higher nonlinear coupling constants g[43] compared with mm-sized systems, but chip-level integration so far comes at the expense of a lower internal optical $Q_{i,o}$,[69] because surface qualities routinely achieved with mechanical polishing are difficult to realize in micro-fabrication processes. We have presented a new device geometry that offers the lowest losses without sacrificing coupling and as a result yields high predicted state transfer fidelities at practical bandwidth and realistic optical pump powers.

Our analysis shows that ultra-low losses, a prerequisite to achieve very strong waveguide over-coupling, turns out to be the most important aspect for any resonant quantum interface to approach the high efficiency and fidelity needed in realistic applications. In comparison, increasing waveguide coupling rates requires higher pump powers to achieve the same cooperativity and dissipates more optical energy in the over-coupled regime, which leads to higher thermal bath occupations. Our analysis also pointed out the importance of low system temperatures, and mm-sized devices not only offer lower optical absorption and scattering losses, which can easily break Cooper pairs in the superconducting microwave cavity, they also offer much larger volume, mass, heat capacity, and surface area for effective thermalization to the cold bath in continuous and pulsed driving schemes.

The presented triply resonant modulator offers a very promising way forward in the field of hybrid quantum systems, both when used for entanglement swapping or for direct conversion of quantum states. Experimental tests will show if the proposed scheme can be implemented as expected and tell us more about the important $LiNbO_3$ material parameters and heating rates at millikelvin temperatures. In the context of classical and quantum

communication applications, with the above given parameters, our system could also work as an ultra efficient electro-optic modulator with a V_π as low as 12.4 mV that can be used for frequency comb generation.[70] Beyond that, we also expect applications of microwave-optical entangled fields in the area of radio frequency sensing, low noise detection, and microwave quantum illumination.[71,72]

DATA AVAILABILITY

The numerical data generated in this work is available from the authors upon resonable request.

Received: 29 August 2019; Accepted: 29 October 2019;
Published online: 28 November 2019

REFERENCES

1. Schoelkopf, R. J. & Girvin, S. M. Wiring up quantum systems. *Nature* **451**, 664–669 (2008).
2. Wendin, G. Quantum information processing with superconducting circuits: a review. *Rep. Prog. Phys.* **80**, 106001 (2017).
3. Kurpiers, P. et al. Deterministic quantum state transfer and remote entanglement using microwave photons. *Nature* **558**, 264–267 (2018).
4. Chou, K. S. et al. Deterministic teleportation of a quantum gate between two logical qubits. *Nature* **561**, 368–373 (2018).
5. Pirandola, S. & Braunstein, S. L. Physics: Unite to build a quantum internet. *Nature* **532**, 169–171 (2016).
6. Liao, S.-K. et al. Satellite-relayed intercontinental quantum network. *Phys. Rev. Lett.* **120**, 030501– (2018).
7. Maring, N. et al. Photonic quantum state transfer between a cold atomic gas and a crystal. *Nature* **551**, 485 EP (2017).
8. Lambert, N. J., Rueda, A., Sedlmeir, F. & Schwefel, H. G. L. Coherent conversion between microwave and optical photons – an overview of physical implementations (2019). arXiv: 1906.10255.
9. Hofheinz, M. et al. Synthesizing arbitrary quantum states in a superconducting resonator. *Nature* **459**, 546–549 (2009).
10. Eichler, C. et al. Observation of two-mode squeezing in the microwave frequency domain. *Phys. Rev. Lett.* **107**, 113601 (2011).
11. Vlastakis, B. et al. Deterministically encoding quantum information using 100-photon schrödinger cat states. *Science* **342**, 607–610 (2013).
12. Braunstein, S. L. & van Loock, P. Quantum information with continuous variables. *Rev. Mod. Phys.* **77**, 513–577 (2005).
13. Weedbrook, C. et al. Gaussian quantum information. *Rev. Mod. Phys.* **84**, 621–669 (2012).
14. Furusawa, A. et al. Unconditional quantum teleportation. *Science* **282**, 706–709 (1998).
15. Lee, N. et al. Teleportation of nonclassical wave packets of light. *Science* **332**, 330–333 (2011).
16. Laurat, J., Coudreau, T., Treps, N., Maître, A. & Fabre, C. Conditional preparation of a quantum state in the continuous variable regime: generation of a sub-poissonian state from twin beams. *Phys. Rev. Lett.* **91**, 213601 (2003).
17. Pogorzalek, S. et al. Secure quantum remote state preparation of squeezed microwave states, Nature Communications, vol. 10, no. 1, p. 2604 (2019).
18. Andrews, R. W. et al. Bidirectional and efficient conversion between microwave and optical light. *Nat. Phys.* **10**, 321–326 (2014).
19. Forsch, M. et al. Microwave-to-optics conversion using a mechanical oscillator in its quantum ground state, Nature Physics, https://doi.org/10.1038/s41567-019-0673-7 (2019).
20. Barzanjeh, S. et al. Stationary entangled radiation from micromechanical motion. *Nature* **570**, 480–483 (2019).
21. Genes, C., Mari, A., Tombesi, P. & Vitali, D. Robust entanglement of a micromechanical resonator with output optical fields. *Phys. Rev. A.* **78**, 032316 (2008).
22. Stannigel, K., Rabl, P., Sørensen, A. S., Zoller, P. & Lukin, M. D. Optomechanical transducers for long-distance quantum communication. *Phys. Rev. Lett.* **105**, 220501 (2010).
23. Barzanjeh, S., Vitali, D., Tombesi, P. & Milburn, G. J. Entangling optical and microwave cavity modes by means of a nanomechanical resonator. *Phys. Rev. A.* **84**, 042342 (2011).
24. Barzanjeh, S., Abdi, M., Milburn, G. J., Tombesi, P. & Vitali, D. Reversible optical-to-microwave quantum interface. *Phys. Rev. Lett.* **109**, 130503 (2012).
25. Wang, Y.-D. & Clerk, A. A. Reservoir-engineered entanglement in optomechanical systems. *Phys. Rev. Lett.* **110**, 253601 (2013).
26. Tian, L. Robust photon entanglement via quantum interference in optomechanical interfaces. *Phys. Rev. Lett.* **110**, 233602 (2013).
27. Zhong, C. et al. Heralded generation and detection of entangled microwave–optical photon pairs. *arXiv e-prints* arXiv:1901.08228 (2019).
28. Bochmann, J., Vainsencher, A., Awschalom, D. D. & Cleland, A. N. Nanomechanical coupling between microwave and optical photons. *Nat. Phys.* **9**, 712–716 (2013).
29. Forsch, M. et al. Microwave-to-optics conversion using a mechanical oscillator in its quantum groundstate. *arXiv:1812.07588v1* (2018).
30. Shao, L. et al. Microwave-to-optical conversion using lithium niobate thin-film acoustic resonators. *arXiv:1907.08593* (2019).
31. Hisatomi, R. et al. Bidirectional conversion between microwave and light via ferromagnetic magnons. *Phys. Rev. B.* **93**, 174427 (2016).
32. Matsko, A. B., Savchenkov, A. A., Ilchenko, V. S., Seidel, D. & Maleki, L. On fundamental quantum noises of whispering gallery mode electro-optic modulators. *Opt. Express* **15**, 17401–17409 (2007).
33. Tsang, M. Cavity quantum electro-optics. *Phys. Rev. A.* **81**, 063837 (2010).
34. Tsang, M. Cavity quantum electro-optics. II. Input-output relations between traveling optical and microwave fields. *Phys. Rev. A.* **84**, 043845 (2011).
35. Javerzac-Galy, C. et al. On-chip microwave-to-optical quantum coherent converter based on a superconducting resonator coupled to an electro-optic microresonator. *Phys. Rev. A.* **94**, 053815 (2016).
36. Soltani, M. et al. Efficient quantum microwave-to-optical conversion using electro-optic nanophotonic coupled resonators. *Phys. Rev. A.* **96**, 043808 (2017).
37. Cohen, D., Hossein-Zadeh, M. & Levi, A. Microphotonic modulator for microwave receiver. *Electron. Lett.* **37**, 300–301 (2001).
38. Ilchenko, V. S., Savchenkov, A. A., Matsko, A. B. & Maleki, L. Whispering-gallery-mode electro-optic modulator and photonic microwave receiver. *J. Opt. Soc. Am. B.* **20**, 333–342 (2003).
39. Strekalov, D. V., Savchenkov, A. A., Matsko, A. B. & Yu, N. Efficient upconversion of subterahertz radiation in a high-Q whispering gallery resonator. *Opt. Lett.* **34**, 713–715 (2009).
40. Strekalov, D. V. et al. Microwave whispering-gallery resonator for efficient optical up-conversion. *Phys. Rev. A.* **80**, 033810–033815 (2009).
41. Botello, G. S.-a et al. Sensitivity limits of millimeter-wave photonic radiometers based on efficient electro-optic upconverters. *Optica* **5**, 1210–1219 (2018).
42. Rueda, A. et al. Efficient microwave to optical photon conversion: an electro-optical realization. *Optica* **3**, 597–604 (2016).
43. Fan, L. et al. Superconducting cavity electro-optics: a platform for coherent photon conversion between superconducting and photonic circuits. *Sci. Adv.* **4**, eaar4994 (2018).
44. Strekalov, D. V., Marquardt, C., Matsko, A. B., Schwefel, H. G. L. & Leuchs, G. Nonlinear and quantum optics with whispering gallery resonators. *J. Optics* **18**, 123002 (2016).
45. Muralidharan, S. et al. Optimal architectures for long distance quantum communication. *Sci. Rep.* **6**, 20463 (2016).
46. Leidinger, M. et al. Comparative study on three highly sensitive absorption measurement techniques characterizing lithium niobate over its entire transparent spectral range. *Opt. Express* **23**, 21690–21705 (2015).
47. Sanchez, A. R. R. *Resonant Electrooptics*. doctoralthesis, Friedrich-Alexander-Universität Erlangen-Nürnberg (FAU) (2018).
48. Goryachev, M., Kostylev, N. & Tobar, M. E. Single-photon level study of microwave properties of lithium niobate at millikelvin temperatures. *Phys. Rev. B.* **92**, 060406 (2015).
49. Weis, R. S. & Gaylord, T. K. Lithium niobate: Summary of physical properties and crystal structure. *Appl. Phys. A.* **37**, 191–203 (1985).
50. Wong, K., of Electrical Engineers, I. & service), I. I. *Properties of Lithium Niobate*. EMIS datareviews series (INSPEC/Institution of Electrical Engineers, 2002).
51. McPeak, K. M. et al. Plasmonic films can easily be better: rules and recipes. *ACS Photonics* **2**, 326–333 (2015).
52. Rakić, A. D. Algorithm for the determination of intrinsic optical constants of metal films: application to aluminum. *Appl. Opt.* **34**, 4755–4767 (1995).
53. Nguyen, D. T. et al. Ultrahigh q-frequency product for optomechanical disk resonators with a mechanical shield. *Appl. Phys. Lett.* **103**, 241112 (2013).
54. Brecht, T. et al. Multilayer microwave integrated quantum circuits for scalable quantum computing. *Npj Quant. Inform.* **2**, 16002 EP (2016).
55. Wenner, J. et al. Surface loss simulations of superconducting coplanar waveguide resonators. *Applied Physics Letters* **99**, 113513 (2011).
56. Gardiner, C. W. & Zoller, P. *Quantum Noise* (Springer Series in Synergetics, 2004).
57. Paris, M. G. A., Illuminati, F., Serafini, A. & De Siena, S. Purity of gaussian states: Measurement schemes and time evolution in noisy channels. *Phys. Rev. A.* **68**, 012314 (2003).
58. Vidal, G. & Werner, R. F. Computable measure of entanglement. *Phys. Rev. A.* **65**, 032314 (2002).

59. Plenio, M. B. Logarithmic negativity: a full entanglement monotone that is not convex. *Phys. Rev. Lett.* **95**, 090503 (2005).
60. Schumacher, B. & Nielsen, M. A. Quantum data processing and error correction. *Phys. Rev. A.* **54**, 2629–2635 (1996).
61. Braunstein, S. L. & Kimble, H. J. Teleportation of continuous quantum variables. *Phys. Rev. Lett.* **80**, 869–872 (1998).
62. Isar, A. Quantum fidelity for Gaussian states describing the evolution of open systems. *Eur. Phys. J. Spec. Top.* **160**, 225–234 (2008).
63. Braunstein, S. L., Fuchs, C. A., Kimble, H. J. & van Loock, P. Quantum versus classical domains for teleportation with continuous variables. *Phys. Rev. A.* **64**, 022321 (2001).
64. Pirandola, S., Eisert, J., Weedbrook, C., Furusawa, A. & Braunstein, S. L. Advances in quantum teleportation. *Nat. Photonics* **9**, 641 EP (2015).
65. Fiurášek, J. Improving the fidelity of continuous-variable teleportation via local operations. *Phys. Rev. A.* **66**, 012304 (2002).
66. Owari, M., Plenio, M. B., Polzik, E. S., Serafini, A. & Wolf, M. M. Squeezing the limit: quantum benchmarks for the teleportation and storage of squeezed states. *N. J. Phys.* **10**, 113014 (2008).
67. Wittmann, C. et al. Demonstration of near-optimal discrimination of optical coherent states. *Phys. Rev. Lett.* **101**, 210501 (2008).
68. Cook, R. L., Martin, P. J. & Geremia, J. M. Optical coherent state discrimination using a closed-loop quantum measurement. *Nature* **446**, 774 EP (2007).
69. Zhang, M., Wang, C., Cheng, R., Shams-Ansari, A. & Loncar, M. Monolithic ultra-high-q lithium niobate microring resonator. *Optica* **4**, 1536–1537 (2017).
70. Rueda, A., Sedlmeir, F., Kumari, M., Leuchs, G. & Schwefel, H. G. L. Resonant electro-optic frequency comb. *Nature* **568**, 378–381 (2019).
71. Barzanjeh, S. et al. Microwave quantum illumination. *Phys. Rev. Lett.* **114**, 080503 (2015).
72. Barzanjeh, S., Pirandola, S., Vitali, D. & Fink, J. M. Experimental microwave quantum illumination. arXiv: 1908.03058 (2019).

ACKNOWLEDGEMENTS

This work was supported by the Institute of Science and Technology Austria (IST Austria) and the European Research Council under grant agreement number 758053 (ERC StG QUNNECT). S.B. acknowledges support from the Marie Skłodowska Curie fellowship number 707438 (MSC-IF SUPEREOM) and J.M.F. from the Austrian Science Fund (FWF) through BeyondC (F71), a NOMIS foundation research grant, and the EU's Horizon 2020 research and innovation program under grant agreement number 732894 (FET Proactive HOT). We thank M. Wulf, H. Schwefel, and C. Marquardt for fruitful discussions.

AUTHOR CONTRIBUTIONS

A.R., W.H., and J.M.F. conceived the project. Analytical analysis was done by A.R. and S.B., and FEM simulations by W.H. All authors contributed to the manuscript. S.B. and J.M.F. supervised the project.

COMPETING INTERESTS

The authors declare no competing interests.

ADDITIONAL INFORMATION

Correspondence and requests for materials should be addressed to A.R. or J.M.F.

Reprints and permission information is available at http://www.nature.com/reprints

Publisher's note Springer Nature remains neutral with regard to jurisdictional claims in published maps and institutional affiliations.